Report No. FHWA-ICT-26-009

Evaluation of Steel Bridge Girders Damaged by Over-height Vehicle Strikes Using Terrestrial Laser Scanning and Machine Learning

Ahmed E. Ibrahim
Limo R. Schissler
Larry A. Fahnestock
James M. LaFave
Ahmed E. Elbanna

ICT Project R27-225

July 2026

ISSN: 0197-9191
ICT Series Report No. 26-011
https://doi.org/10.36501/0197-9191/26-011

TECHNICAL REPORT DOCUMENTATION PAGE

<table>
<tr><td>1. Report No.
FHWA-ICT-26-009</td><td colspan="2">2. Government Accession No.
N/A</td><td colspan="2">3. Recipient's Catalog No.
N/A</td></tr>
<tr><td colspan="3" rowspan="2">4. Title and Subtitle
Evaluation of Steel Bridge Girders Damaged by Over-height Vehicle Strikes Using Terrestrial Laser Scanning and Machine Learning</td><td colspan="2">5. Report Date
July 2026</td></tr>
<tr><td colspan="2">6. Performing Organization Code
N/A</td></tr>
<tr><td colspan="3">7. Authors
Ahmed E. Ibrahim (https://orcid.org/0000-0002-2275-6293), Limo R. Schissler (https://orcid.org/0009-0004-9653-5348), Larry A. Fahnestock (https://orcid.org/0000-0003-3172-2260), James M. LaFave (https://orcid.org/0000-0001-6514-2163), Ahmed E. Elbanna (https://orcid.org/0000-0003-4079-2607)</td><td colspan="2">8. Performing Organization Report No.
ICT-26-011
UILU-2026-2011</td></tr>
<tr><td colspan="3" rowspan="2">9. Performing Organization Name and Address
Illinois Center for Transportation
Department of Civil and Environmental Engineering
University of Illinois Urbana-Champaign
205 North Mathews Avenue, MC-250
Urbana, IL 61801</td><td colspan="2">10. Work Unit No.
N/A</td></tr>
<tr><td colspan="2">11. Contract or Grant No.
R27-225</td></tr>
<tr><td colspan="3" rowspan="2">12. Sponsoring Agency Name and Address
Illinois Department of Transportation (SPR)
Bureau of Research
126 East Ash Street
Springfield, IL 62704</td><td colspan="2">13. Type of Report and Period Covered
Final Report 10/1/20–7/31/26</td></tr>
<tr><td colspan="2">14. Sponsoring Agency Code</td></tr>
<tr><td colspan="5">15. Supplementary Notes
Conducted in cooperation with the U.S. Department of Transportation, Federal Highway Administration.
https://doi.org/10.36501/0197-9191/26-011</td></tr>
<tr><td colspan="5">16. Abstract
Bridge strikes caused by over-height vehicles frequently damage steel girders and can reduce their load-carrying capacity, requiring rapid and reliable evaluation to ensure structural safety. Current evaluation practices rely on manual measurements that often require traffic disruptions and simplified assessment approaches that do not fully capture the effects of damage. In addition, finite element simulations are time-consuming and computationally intensive to develop for practical rapid evaluation. This study developed an integrated, data-driven framework for the inspection and assessment of damaged steel bridge girders. A semiautomated procedure was developed to process laser-scan point cloud data and extract displacement profiles along the girder span. Machine learning models were trained and validated using a dataset generated from finite element simulations informed by field measurements of actual bridge strike incidents to predict the residual capacity of damaged girders. Explainable artificial intelligence techniques were incorporated to interpret model predictions and identify key parameters influencing structural performance. Results demonstrated the framework's capabilities in effectively capturing girder displacements, and for accurately and efficiently estimating the residual capacity, to support post-strike bridge evaluation. Measured girder deformations obtained from laser scanning can be used as inputs to the machine learning models for quantifying a girder's capacity. The predicted capacity can then be incorporated into bridge rating software to compute rating factors, enabling rapid decisions on traffic restrictions and load posting. Additionally, the interpretability results can guide engineers in identifying critical design parameters and prioritizing repair actions.</td></tr>
<tr><td colspan="2">17. Key Words
Steel Bridges, Girders, Girder Bridges, Impact Damage, Low-Clearance Bridges, Machine Learning, Terrestrial Laser Scanning, Point Clouds</td><td colspan="3">18. Distribution Statement
No restrictions. This document is available through the National Technical Information Service, Springfield, VA 22161.</td></tr>
<tr><td>19. Security Classif. (of this report)
Unclassified</td><td colspan="2">20. Security Classif. (of this page)
Unclassified</td><td>21. No. of Pages
79 + appendix</td><td>22. Price
N/A</td></tr>
</table>

Form DOT F 1700.7 (8-72) **Reproduction of completed page authorized**

ACKNOWLEDGMENT, DISCLAIMER, MANUFACTURERS' NAMES

This publication is based on the results of **ICT-R27-225: Strength and Serviceability of Damaged Steel Girders**. ICT-R27-225 was conducted in cooperation with the Illinois Center for Transportation; the Illinois Department of Transportation; and the U.S. Department of Transportation, Federal Highway Administration.

Members of the Technical Review Panel (TRP) were the following:

- Spencer Koehler, TRP Chair, Illinois Department of Transportation
- Ruben Boehler, Illinois Department of Transportation
- Jeff Burke, Illinois Department of Transportation
- Brandon Dudley, Illinois Department of Transportation
- Nick Lombardi, Federal Highway Administration
- Robert Perkins, Illinois Department of Transportation
- Sarah Wilson, Illinois Department of Transportation

EXECUTIVE SUMMARY

Bridge strikes caused by over-height vehicles often result in significant damage to steel girders and potential reductions in structural capacity. These incidents typically occur when vehicles exceed vertical clearance limits due to improper loading or hauling of equipment. Current inspection practices mainly rely on manual measurements, which can be time-consuming, require lane closures, and pose safety challenges for bridge inspectors. While emerging technologies such as terrestrial laser scanning (TLS) can provide more comprehensive and efficient means of capturing girder deformations, they require specialized processing procedures to extract meaningful measurements. Moreover, detailed finite element simulations can accurately characterize damage and predict structural behavior, but they are time-consuming and computationally intensive to develop, hindering rapid evaluation of post-strike bridge conditions. These challenges highlight the need for efficient and reliable approaches to support timely decision-making following bridge strike events.

This study introduced an integrated, data-driven framework for rapid inspection and assessment of damaged steel girders. First, current practices for evaluation and repair were reviewed to identify limitations and practical challenges of existing methods. Next, a semiautomated procedure was developed to process TLS point cloud data for extracting displacement measurements along the span length of damaged girders. Then, several machine learning models were trained and validated using a dataset generated from detailed finite element analyses of damaged steel girders to predict the residual load-carrying capacity and identify key design and damage parameters influencing structural response. The constructed dataset included a wide range of girder geometries and damage scenarios that were informed by field measurements and observations from actual bridge strike incidents.

Results demonstrated that the proposed framework provides an efficient and reliable approach for evaluating damaged steel girders. The developed point cloud processing procedure successfully captured both displacement and tilt of the girder bottom flange, promoting precise characterization of the damage while eliminating disruptive field operations. The machine learning methodology provided an efficient and accurate surrogate to time-consuming finite element simulations, enabling a practical alternative for rapid residual capacity assessment. Integration of explainable artificial intelligence techniques enhanced understanding of key factors influencing structural performance of damaged steel girders and provided a quantitative basis to support informed decision-making. To facilitate practical implementation of the proposed methods, web-based diagnostic tools were developed, incorporating advanced point cloud measurement extraction and data-driven predictions, to improve the speed, accuracy, and execution of post-strike bridge evaluations.

TABLE OF CONTENTS

LIST OF FIGURES

LIST OF TABLES

CHAPTER 1: INTRODUCTION

PROBLEM STATEMENT

Bridges are frequently subjected to vehicle impacts, which can significantly compromise their structural performance and, in severe cases, lead to partial or full collapse (Dunne and Thorkildsen 2020; Stark et al. 2016). Steel bridge girders are especially subjected to collisions from over-height vehicles exceeding the vertical clearance beneath bridges, as illustrated in Figure 1. These impacts can introduce substantial permanent deformation and reduction in load-carrying capacity, requiring rapid evaluation to determine whether the affected girders remain safe for service (Finley 2006; Ghosn et al. 2003).

Figure 1. Photo. Over-height vehicle lodged beneath a bridge following an impact incident.

Source: Courtesy of IDOT

The prevalence of bridge strikes has been well documented. A national survey conducted by Agrawal et al. (2011) indicated that most state departments of transportation (DOTs) consider bridge strikes to be a significant problem, with over-height vehicles identified as the primary cause. Similarly, Fu et al. (2004) reported a substantial increase in strike incidents in Maryland between 1995 and 2000. On a national scale, the number of bridge strikes in the United States exceeds 15,000 annually, most of which involve overhead impacts on girders or stringers (Dunne and Thorkildsen 2020).

According to AASHTO *LRFD Bridge Design Specifications* (2020), vehicle collisions with bridge superstructures are classified as extreme limit states with potentially severe safety and operational consequences. While design provisions aim to prevent collapse and ensure life safety, even in the presence of significant inelastic deformation, post-strike evaluation remains essential for determining the residual load-carrying capacity of damaged girders. In practice, this requires rapid and reliable assessment methods to support decisions regarding traffic restrictions, bridge posting, or immediate repair actions.

Existing methods for inspecting bridge girder impact damage rely on manual methods and conservative, subjective judgments. For example, the Illinois Department of Transportation (IDOT) *Structural Services Manual* (2024) details a procedure for hand measurements of displacements near the impact point of a girder. Performing hand measurements typically requires lane closures and working at height, and it may not be practical to measure displacements relative to the supports (at span ends) due to site constraints. Terrestrial laser scanning (TLS) is an emerging method for inspection of steel girders damaged in bridge strikes (Schissler et al. 2026a). A TLS-based approach can give more comprehensive data for characterizing both displacement and tilt of the girder bottom flange along an entire span length, and lane closures can often be avoided. However, a specialized point cloud processing approach is needed to efficiently extract damaged girder displacements.

Additionally, although detailed finite element (FE) modeling can provide valuable insight into damage progression and failure mechanisms of steel girders subjected to vehicle impacts, such analyses are typically developed for individual cases and require substantial time and computational effort to perform (Ibrahim et al. 2026). This limitation restricts their applicability for rapid field assessment following bridge strike incidents.

Recent advancements in artificial intelligence (AI) offer a promising alternative to traditional computational approaches (Wang et al. 2023). In particular, machine learning algorithms have demonstrated strong capability in civil engineering applications for predicting structural performance, assessing condition, and supporting engineering decision-making (Reich 1997; Deka 2019; Sun et al. 2021; Di Mucci et al. 2024). These developments motivate the use of machine learning–based frameworks to enable efficient and data-driven estimation of residual load-carrying capacity of damaged steel girders, providing a practical tool for rapid post-strike assessment.

BACKGROUND AND LITERATURE REVIEW

Terrestrial Laser Scanning for Damage Inspection

Laser scanning is a nondestructive inspection technique in which a light detection and ranging (lidar) system detects points on the surfaces of objects. The result is a point cloud, which contains the coordinates of all points detected. The laser scanner can only detect points that are within its line of sight, so scans are typically performed from several vantage points to capture necessary geometric features. Data from all vantage points are subsequently combined into a single point cloud.

In TLS, the laser scanner is placed in a stationary position on the ground during each scan. TLS typically has higher accuracy than other laser scanning methods (such as aerial laser scanning using drones or mobile laser scanning using vehicles), though accuracy of all methods is consistently improving thanks to advances in equipment technology. For TLS, accuracy and precision are typically at the millimeter level for recent equipment (Seo et al. 2021).

Point clouds are unstructured datasets with no inherent relationships between points, so processing is necessary to extract meaningful information (Xu et al. 2021). Processing challenges include variable accuracy and density throughout the point cloud (based on the distance from the scanner), along with redundant points in overlapping areas from multiple scan positions. A phenomenon termed "mixed pixels" occurs when a single laser-scan beam is reflected to the scanner by two surfaces, generating a "noise" point that lies on neither surface (Wang et al. 2016). Because laser scanning relies on the laser beam being reflected back to the sensor, sharp corners are often not shown accurately in the point cloud. Additionally, the point cloud may include outlier points when scanning reflective surfaces, such as polished metal or plastic (Wang and Feng 2014). An effective processing method must address these challenges.

Rashidi et al. (2020) reviewed TLS applications related to bridges, including generation of 3D models, quality inspection, structural assessment, and bridge information modeling. Truong-Hong and Laefer (2019) summarized advantages of laser scanning over manual bridge inspection and highlighted developments in data collection, geometric modeling, and structural inspection. TLS is particularly useful for measurements such as bridge deformation (e.g., Ziolkowski et al. 2018; Tysiac et al. 2022; Zhou et al. 2024) and vertical clearance (Riveiro et al. 2013; Xu et al. 2024) because it can capture measurements over a continuous region of a bridge, whereas manual measurements are only recorded at a few discrete locations.

Although current literature has documented TLS for bridge construction, operation, and maintenance under normal operating conditions, only one instance has been found where TLS was applied to a steel-girder roadway bridge subject to impact damage. Stull and Earls (2009) created a solid FE model of an impacted bridge based on TLS data. First, an undamaged model of the bridge was developed based on the as-built plans and inspection reports. Then, TLS data were used to model the geometry in damaged regions of the steel girders. The approach focused on localized damage features, and the implementation was not automatic.

Other studies (e.g., Cha et al. 2019; Lee et al. 2019; Erdélyi et al. 2020; Zhao et al. 2024) explored methods for structural steel displacement monitoring by comparing laser-scan point clouds taken at different times. However, prior laser scans are rarely available for structures that experience impact damage because laser scanning is a developing tool that is not yet part of regular documentation and inspection processes, making point cloud comparison approaches infeasible. These studies were also designed for typical undamaged steel members and include assumptions such as planar flange surfaces or nontilted flanges. A new method is needed to obtain a displacement curve for a member that has experienced impact damage.

Despite the growing body of research related to TLS for bridges, adoption of laser scanning in the construction industry has been limited because the equipment is expensive and requires specialized training. TLS yields point cloud data that are unstructured and have no inherent relationships between points, which means that processing is necessary to extract meaningful information (Xu et al. 2021). Further research on detailed methods to process bridge point cloud data in conjunction with other emerging techniques can be useful to hesitant industry professionals (Psomas et al. 2022).

Finite Element Analysis of Damaged Steel Girders

Finite element analysis has been widely adopted for investigating the structural behavior of steel bridge girders subjected to over-height vehicle strikes. Early and recent studies have utilized nonlinear FE simulations to capture the response of girders under various impact scenarios. For instance, Wang et al. (2022) conducted parametric investigations to quantify how variations in damage geometry and location influence load-deflection behavior of steel girders, demonstrating that both factors significantly affect stiffness and ultimate capacity of the girders. Similarly, Oppong et al. (2024) performed nonlinear analyses to evaluate induced deformation patterns and associated impact forces related to different types of impacting objects.

Other studies have focused on identifying and classifying damage mechanisms. Xu et al. (2013) developed numerical models to simulate impact events on prestressed concrete and composite steel-concrete bridge systems. The study proposed simplified formulations for estimating collision forces and identified two categories of damage: global damage modes, such as lateral and vertical deflections, and localized effects including yielding and buckling in girder components.

Research has also examined the implications of cross-sectional distortion on structural performance. Bedi (2000) modeled isolated steel girders with existing lateral deformation and demonstrated that distortion leads to a reduction in sectional stiffness, particularly the moment of inertia. The study further noted that relying solely on the deformed geometry to estimate load-carrying capacity may result in unconservative estimates, emphasizing the need for more comprehensive analytical or numerical evaluation methods.

Furthermore, analytical approaches have been proposed to complement FE modeling. For example, Shenton et al. (2006) estimated a reduced load rating factor based on the deformed cross-section of a damaged girder. Their approach assumed that composite action with the deck constrains the top flange to remain horizontal, thereby simplifying load application conditions. While efficient, such assumptions may limit applicability in cases involving significant damage, loss of composite behavior, or non-composite construction.

RESEARCH OBJECTIVES AND REPORT OUTLINE

The objective of this research is to develop an integrated, data-driven framework for rapid inspection, assessment, and evaluation of steel bridge girders damaged by over-height vehicle strikes. To achieve this goal, the study is organized into five tasks. These tasks include a summary of current practices for damage evaluation (Chapter 2), damage characterization using terrestrial laser scanning (Chapter 3), finite element numerical modeling (Chapter 4), machine learning prediction of residual capacity (Chapter 5), and development of diagnostic tools based on the technologies established in this research (Chapter 6). Finally, in Chapter 7, a summary of the findings, including advantages of the proposed framework, is presented along with overall conclusions from the research. The tasks are summarized as follows.

Summary of current practices for damage evaluation. Current IDOT practices for inspection, assessment, and repair are reviewed. The IDOT *Structural Services Manual* (2024) details official procedures, such as manual measurement of displacements during inspections and curvature calculations for selecting the repair method. Additional informal practices are also included based on discussions with IDOT inspectors and engineers. A modernized method for evaluation could improve efficacy.

Damage characterization using terrestrial laser scanning. TLS is positioned as an effective method for characterizing impact damage to steel I-girders. First, a description of common approaches for performing a TLS scan of a damaged girder are reported, based on interviews with IDOT surveyors. Then, the authors present a new semiautomated modular procedure for processing laser-scan point cloud data of steel I-sections to obtain bottom-flange displacement profiles along the length of a span. Several existing point cloud processing techniques are incorporated, including outlier removal, voxelization, cross-sectional slicing, and random sample consensus (RANSAC) regression. Four case studies are discussed.

Finite element numerical modeling. Detailed 3D nonlinear FE models are developed to simulate damage mechanisms and evaluate the structural response of steel I-girders subjected to over-height vehicle strikes. The modeling framework incorporates material behavior, boundary conditions, and loading sequences informed by field measurements and observations. The resulting simulations are used to generate a comprehensive dataset capturing a wide range of girder cross-sectional geometries, span lengths, damage magnitudes, and impact locations, forming the basis for data-driven modeling.

Machine learning prediction of residual capacity. The generated dataset is used to train and validate multiple machine learning models for estimating the post-strike load-carrying capacity of damaged I-girders. The approach includes data preprocessing, model development, and performance evaluation using statistical metrics and cross-validation techniques. In addition, explainable artificial intelligence methods are integrated to interpret model predictions, identify key influencing parameters, and provide insights that align with structural behavior.

Development of diagnostic tools. The methodologies established in this research are translated into interactive, user-oriented applications to support bridge evaluation in practice. Two complementary tools have been developed to enhance accessibility and implementation of rapid evaluation for damaged I-girders. The first tool follows the workflow of point cloud–based measurements to process TLS data and extract girder deformation profiles. The second tool integrates the trained machine learning model and user-defined inputs to predict residual load-carrying capacity and provide recommendations informed by model interpretability. These tools are deployed through a web-based interface to facilitate their use by state DOTs, enabling streamlined and data-driven decision-making for damaged steel girders.

CHAPTER 2: SUMMARY OF CURRENT PRACTICES FOR DAMAGE EVALUATION

The authors conducted a detailed survey that gathered information about current state highway agency practices related to bridge strikes. Twenty-three responses were received, with full results published in an interim project report (Schissler et al. 2024). This chapter presents a more detailed description of current impact damage evaluation practices in Illinois. The most relevant aspects are included, but this description is not exhaustive. First, an overview of inspection and repair procedures detailed in the IDOT (2024) *Structural Services Manual* is presented, followed by a description of a typical IDOT load rating procedure.

IDOT *STRUCTURAL SERVICES MANUAL*

Inspection (*Structural Services Manual* Section 2.3.3)

The IDOT (2024) *Structural Services Manual* prescribes a procedure for measuring girder displacements resulting from bridge strikes on steel I-girders. Engineers use these measurements as a factor when determining what, if any, repair is necessary. Measurements are performed by hand, which typically requires lane closures underneath the bridge. As illustrated in Figure 2, inspectors measure the vertical and horizontal flange deflections at longitudinal intervals of 7.6 cm (3 in.) along a 61 cm (2 ft) distance on each side of the point of maximum displacement, which is assumed to be the impact point. If the impact is at a splice, deflections over a 122 cm (4 ft) distance on each side of the impact point are measured. Horizontal web deflections are measured at 5.1 cm (2 in.) vertical intervals along the depth of the web at the point of impact and 7.6 cm (3 in.) to each side, as shown in Figure 3. The primary purpose of displacement measurements is to accurately determine whether a beam can be straightened or must be replaced. The inspector may decide that measurements need not be performed if a visual inspection indicates the damage is so severe that replacement is necessary. A girder may only be straightened once; a second impact on the same area prompts replacement.

Deflections are not necessarily measured from the true initial position of a girder. Instead, inspectors typically extend a string between two flange edge locations relatively far from the line of impact, as illustrated in Figure 4, and measurements are taken relative to the string. (Additional photographs of stringline placement are included in Figure 67 and Figure 68 in Appendix A.) Judgment about where the string reference should be placed is qualitative, so damage-related deflections may extend beyond the reference locations. Additionally, in some cases, measurements of flange deflections may continue beyond the specified 61 cm (2 ft) longitudinal distance on each side of the impact location if deemed necessary by the inspector.

The IDOT *Structural Services Manual* requires inspectors to further document the impact with photographs and sketches. Inspectors also note information on plans, such as the impact location, locations of damaged cross-frames or connecting elements, damage to the concrete slab at the top flange of the girder, and extent of impact deflection.

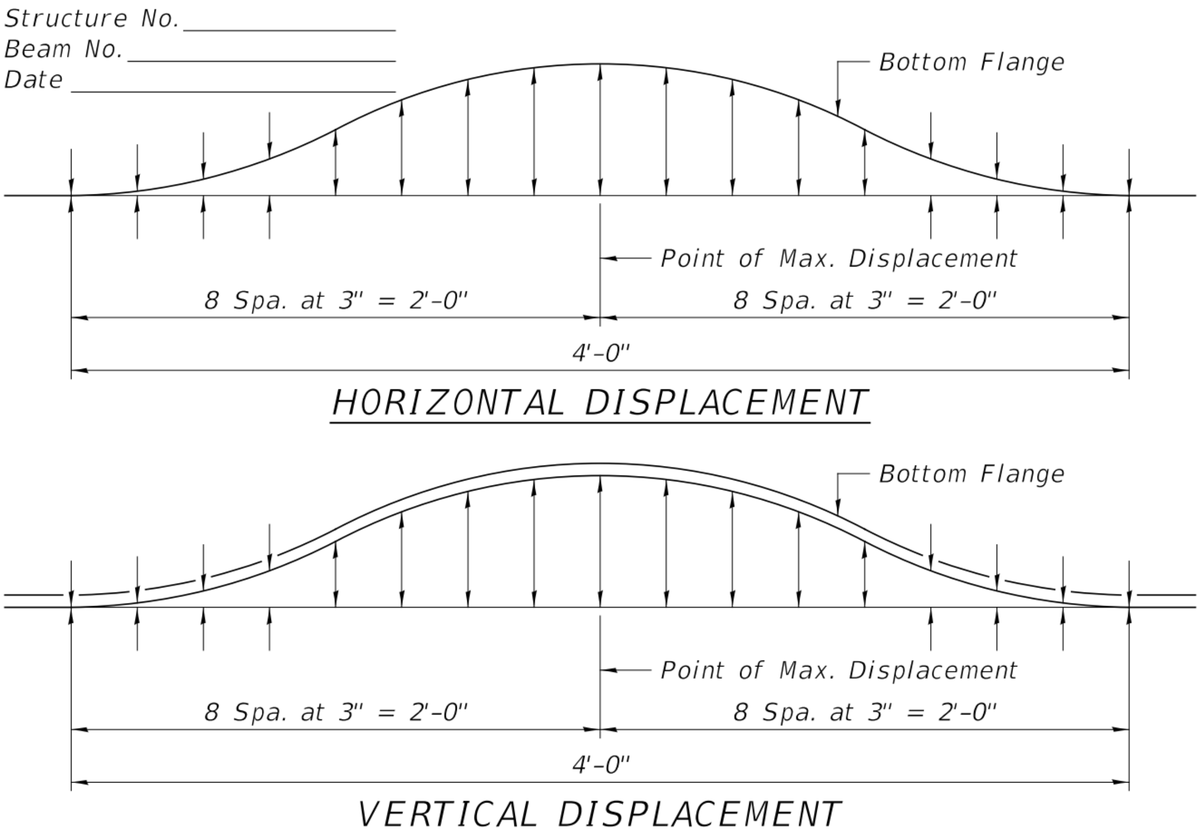

Figure 2. Diagram. Horizontal and vertical displacement measurements at 7.6 cm (3 in.) intervals over a 61 cm (2 ft) distance on each side of the impact point.

Source: IDOT (2024)

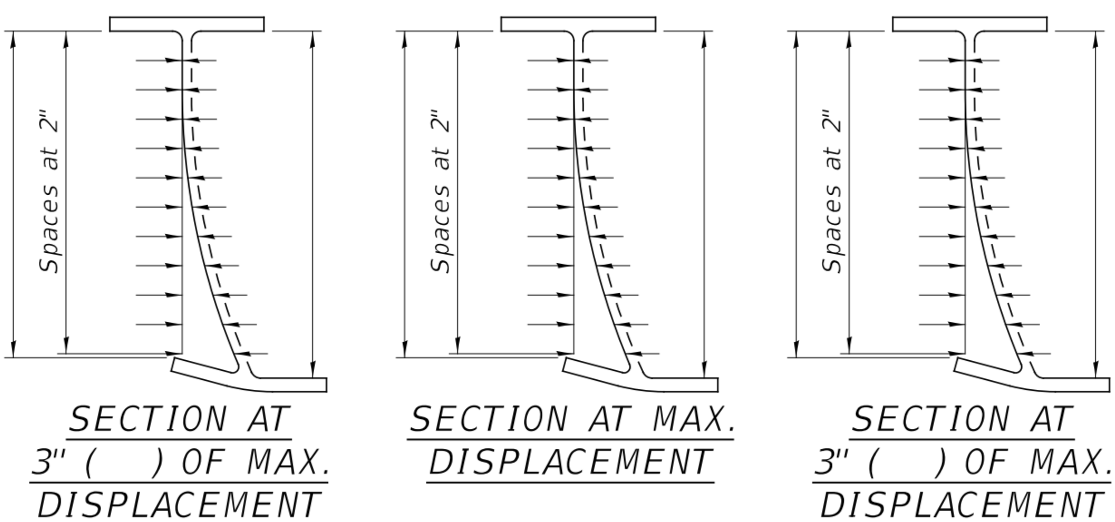

Figure 3. Diagram. Displacements measured along the web height at 5.1 cm (2 in.) intervals, including at 7.6 cm (3 in.) to the left and right of the impact.

Source: IDOT (2024)

Figure 4. Photo. Stringline placement for hand measurements of flange deflections on IDOT bridge SN 084-0077 Girder 19. (The stringline is colored pink.)

Source: Courtesy of IDOT

Repair (*Structural Services Manual* Section 2.13)

The IDOT (2024) *Structural Services Manual* discusses repairs to steel beams damaged in impact events. Guidelines from NCHRP Report 271 (Shanafelt and Horn 1984) are referenced for determining repair actions after a damaging event. IDOT uses three primary repair techniques for damaged girders: (1) straightening, (2) straightening and strengthening, and (3) replacing the damaged portion of the girder. Per Shanafelt and Horn (1984), repair method selection should be based on the amount of impact-induced strain. The approximate damage radius of curvature is calculated, using deflection measurements from the field inspection, and is then compared to the radii of curvature at yield strain, 15 times yield strain, and 5% nominal strain to identify the recommended repair. The radius of curvature of a damaged girder can be computed in both the horizontal and vertical directions. Figure 5 includes a diagram and corresponding approximate radius of curvature calculation equations for a damaged girder. The result is approximate because the calculation uses finite increments and assumes the incremental length is equal to the arc length; accuracy is reduced for large angles of rotation. (Please see Shanafelt and Horn [1984] for a more detailed discussion of this approach.)

IDOT straightening currently only includes mechanical methods (using timber bracing, jacks, cables, and winches to push or pull the damaged girder back to its original position); typical details are included in the *Structural Services Manual*. An example of mechanical straightening for a fascia I-girder (deflected away from the interior girders) is included in Figure 6. After straightening operations are complete, nondestructive testing is prescribed for welded connections near the damaged area to evaluate whether further retrofitting is necessary. Gouges caused by the impact are typically ground smooth. If strengthening is necessary, bolted plates are used. Strengthening plates are recommended to have the same capacity as the damaged flange for a simple and conservative approach, and plates can be installed on the top and bottom surfaces of the flange to minimize further reductions in vertical clearance.

When damage is severe or a girder has been impacted multiple times at the same location, replacement is necessary for both non-composite and composite girders. A girder replacement requires a temporary shoring plan to prevent excessive deflections during repair; often, a carrier beam is installed above the bridge deck to support the deck, and oak timbers are used for cribbing and bracing. Replacement may occur between existing field splices or at new splices, depending on the damage geometry.

The full section of a non-composite girder can be replaced without removing the existing concrete deck, whereas a full-section composite girder replacement requires also replacing a portion of the deck over the girder (and possibly the concrete parapet, if repairing a fascia girder). To facilitate repair installation for composite I-girders, IDOT commonly uses a “zipper detail” method in which only the bottom flange and lower portion of the web are replaced in the damaged area. The new portion of the girder is attached via bolted connections. Typical details and additional considerations are discussed in the *Structural Services Manual*. A photograph of an in-progress “zipper detail” repair is included in Figure 7.

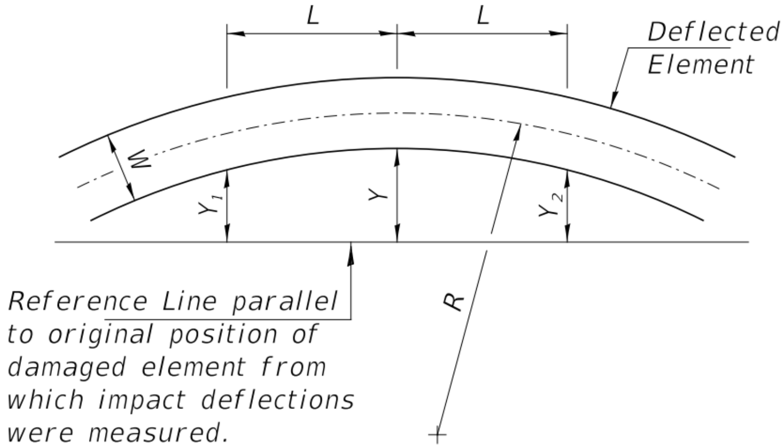

CALCULATION OF DAMAGE CURVATURE

$$R \cong \frac{L^2}{Y_1 + Y_2 - 2Y}$$

L = increment lengths at which deflection measurements were taken.
Y = offset of deflected element from reference line.
R = approximate radius of curvature at location of offset Y.

Figure 5. Diagram. Method for computing damage curvature.

Source: IDOT (2024)

Figure 6. Photo. Straightening IDOT bridge SN 084-0077 Girder 10 (fascia girder) using chains attached to Girder 11 (first interior girder).

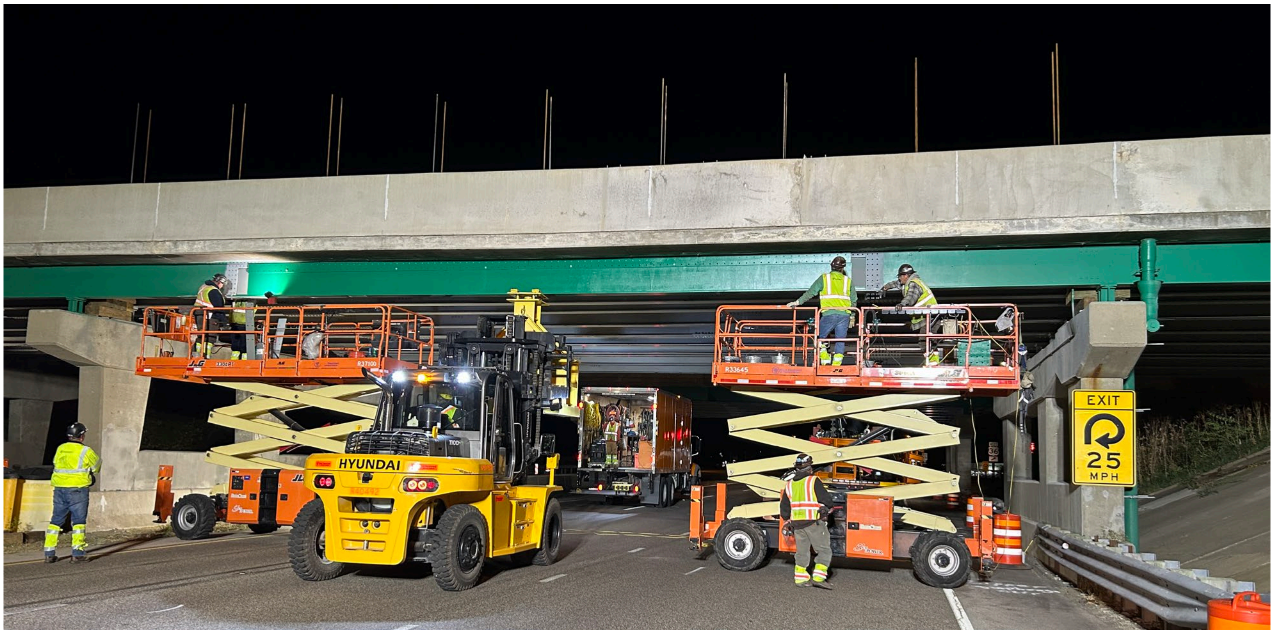

Figure 7. Photo. Installation of a "zipper detail" repair for IDOT bridge SN 084-0077 Girder 19 (fascia girder). The replacement section has been lifted into place, but bolts have not yet been installed.

Source: Courtesy of Kyle Hutson, IDOT

IDOT DAMAGE EVALUATION PROCEDURE

The IDOT (2024) *Structural Services Manual* does not include an approach for assessing the capacity of a damaged girder. Instead, the typical IDOT damage evaluation procedure was ascertained through discussions with IDOT engineers. This procedure can change based on the engineers' assessment of each damage case. Typically, the most severely damaged girder on a bridge is evaluated. While a complete finite element model would provide the most accurate indication of girder capacity, developing these models is too time-consuming when a rapid decision is needed after a bridge strike.

Example hand sketches and calculations for the damage evaluation process are included in Figure 8. Initially, an engineer estimates the maximum horizontal and vertical displacements, the portion of the I-girder web that is bent, the rotation angle of the web, the rotation angle of the flange, and the longitudinal extent of damage. These values are typically approximately determined from photographs, and the estimates are generally conservative. Using these values, a damaged cross-section moment of inertia is computed (shown as I_{dam} in Figure 8). In Figure 8, the bottom cover plate was conservatively assumed to be ineffective.

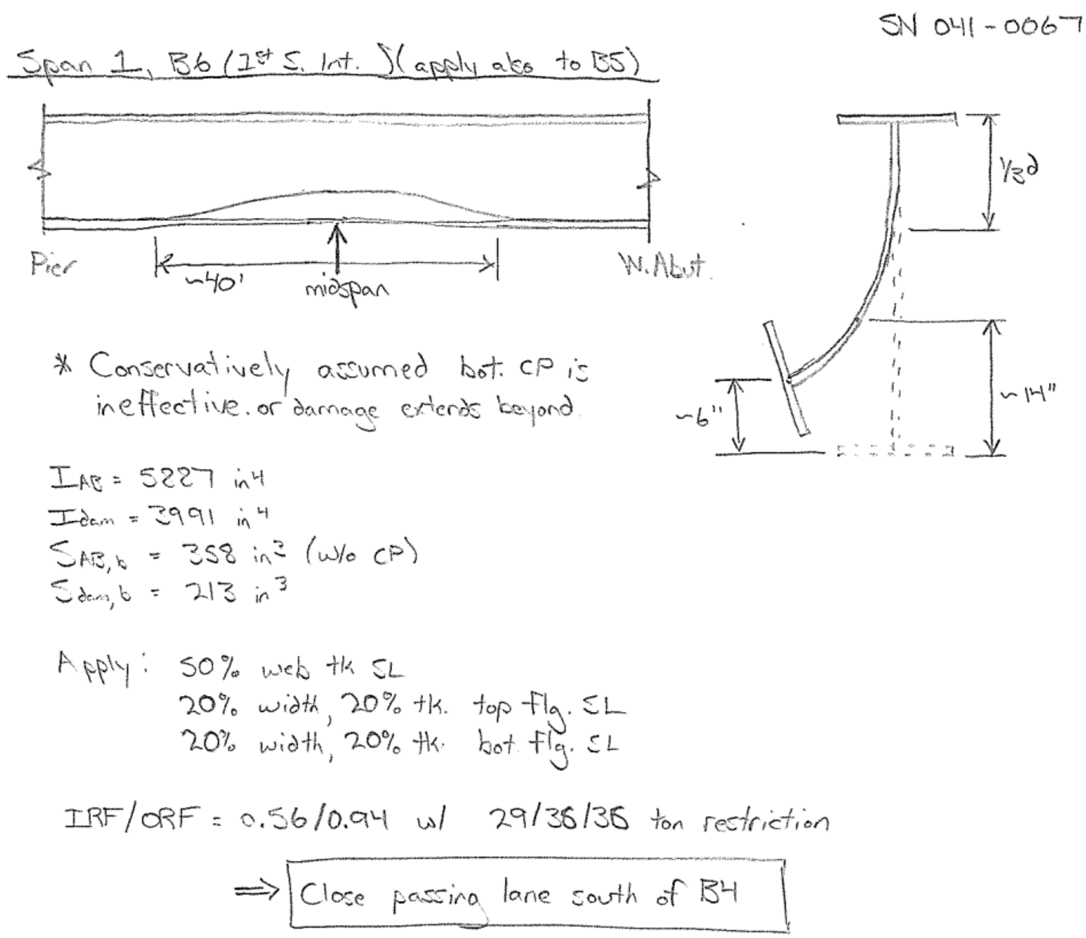

Figure 8. Illustration. Summary of damage assessment parameters for IDOT bridge SN 041-0076 Girder 6.

Source: Courtesy of IDOT

IDOT then uses the AASHTOWare software for bridge load rating. AASHTOWare is convenient for this application because it considers several limit states, and IDOT typically maintains an AASHTOWare model for each bridge in the state inventory. However, AASHTOWare does not have capability to explicitly consider impact damage. Instead, IDOT engineers adapt the section loss (corrosion) damage feature for this purpose. Reductions in flange and web thicknesses are applied until the resulting cross-section moment of interia, I_x, is equal to the estimated cross-section moment of inertia for the impacted girder, I_{dam}. AASHTOWare allows the user to define the longitudinal distance over which the reduced section is applied; engineers adjust this parameter as needed. An engineer evaluates the resulting inventory and operating load ratings and decides whether the bridge condition is satisfactory. Typically, the bridge remains open if the load rating(s) are greater than one. In Figure 8, the inventory and operating load ratings were both less than one for that bridge, so the lane above the damaged girder was closed.

CHAPTER 3: DAMAGE CHARACTERIZATION USING TERRESTRIAL LASER SCANNING

Laser scanning would be beneficial for inspecting damaged steel bridge girders because high-resolution data can be obtained without working at height and possibly without lane closures underneath the damaged bridge (unless lane closures are necessary for other reasons). While hand measurements only obtain displacement values at discrete points along a girder, a typical TLS scan includes millions of points and therefore captures a more complete and detailed geometry of the damage. Hand displacement measurements are relative to a string line reference that is placed subjectively, but displacements extracted from a laser scan can be measured with respect to the supports (as long as the entire span is captured within the scan, which is reasonable). Furthermore, hand measurements only document displacements of one point on the cross-section (e.g., the I-girder bottom-flange lower-left or lower-right corner), whereas a TLS scan can capture displacements of multiple reference points to document the cross-sectional tilt in addition to translation.

This background highlights that TLS offers several benefits over traditional hand measurement methods and is a promising approach for characterizing damage to steel I-sections. However, although TLS has been used for investigating various damage to steel I-sections, there is no standard method for obtaining a flange displacement curve along an entire member. Current TLS displacement measurement methods require manually aligning the point cloud and selecting specific points, which is impractical for obtaining a displacement curve to characterize damage over a complete span. The researchers aim to address these gaps by presenting a new semiautomated modular procedure for processing a laser-scan point cloud to obtain measurements of the horizontal and vertical deflections of a flange of a steel I-section along its length. After an impact event occurs, flange displacement measurements can provide insight into the geometry of the damage, which is useful for assessing severity and determining an appropriate course of action. The procedure can also be implemented to measure deflections in undamaged members.

For this project, TLS was selected as the scanning method (instead of drone- or vehicle-mounted lidar) because it is already within the scope of IDOT capabilities and can be readily implemented in the field. Point clouds of impacted steel bridges (all having hot-rolled W-shaped girders) in Illinois were used for development of the procedure. All point clouds were captured with a Trimble SX10 3D scanning total station and provided directly by IDOT. The Trimble SX10 was used for data capture because IDOT already owns the equipment and has trained staff to perform scans. Many state agencies have immediate access to similar equipment. Additionally, the Trimble SX10 can perform scans from some distance away from a bridge and therefore can be used to characterize girders over live traffic. However, the methods presented in this report are applicable to data from any modern TLS equipment. Drone-mounted lidar is consistently improving in accuracy and may soon be suitable for the proposed measurement procedure as well.

IDOT TLS FIELD SETUP

IDOT already has some experience with laser scanning for other inspection purposes. In September 2025, one of the researchers attended a site visit to observe an IDOT laser scan of bridge structure number (SN) 057-0025 in Normal, Illinois. Impact damage to bridge SN 057-0025 was discovered during a routine inspection in August 2025. Mike Young and the IDOT District 5 survey crew explained their laser scanning process and answered questions. Additionally, the research team later worked with Robert Stickelmaier, District 4 Chief of Surveys, to present about laser scan procedures to an audience of IDOT bridge maintenance engineers. Highlights are included below.

Most IDOT districts use a Trimble SX10 scanning total station for TLS scans, so the discussion below focuses on options available using this setup. An external controller is used to select scan settings, start the scan, monitor progress, and review initial results. Equipment from other manufacturers likely has similar overall functionality. The authors do not endorse any particular equipment or manufacturer. State highway agencies and others intending to perform TLS inspections should consider equipment costs, accuracy and precision requirements, speed of data collection, and compatibility with other equipment (among other factors) when deciding which scanner to procure.

Scanning Approaches

A laser scan can be performed using either a controlled or uncontrolled setup. Both IDOT District 4 and District 5 recommend and commonly use a controlled setup. In a controlled setup, laser scans are taken from points with known coordinates and elevations. Working points and backsights must therefore be set prior to the scan. Point cloud data are then automatically collected in a consistent global coordinate system, facilitating incorporation with design plans, Google Earth, or other applications. Adding more scan locations and registering them is a simple process, allowing flexibility when performing the scan.

An uncontrolled scan setup does not require any surveying before performing the scan. Each scan is recorded in its own local coordinate system (relative to the scanner position). A scan from a single location can be performed easily, providing quick results if one perspective is acceptable. However, extra steps are required to register multiple scans to a consistent global coordinate system, which can increase the likelihood of errors. Registration can be accomplished by identifying and aligning common features among various scans (such as bolts, markings, or special targets placed on the scene) and/or using various algorithms to refine the results, such as the iterative closest point algorithm. Some software may assist with these registration tasks.

Performing the Scan

The scan operator selects the number of scan locations based on the extent of features that need to be captured and level of detail required. For example, documenting one span of a damaged fascia girder could require four scan locations, while documenting an entire bridge could require 16 scan locations. Scan locations could include in front of or behind a bridge, on the slope wall underneath a bridge, on a median or shoulder underneath a bridge, or on an approach embankment. Three examples of scan positions are shown in Figure 9. Scans can often be performed entirely from the shoulder or median of a roadway, avoiding road closures. For assessing damaged girders, scans are not typically performed from the top of the bridge, so the top of the bridge deck is not typically included in the resulting point cloud.

A. Scanner positioned on the slope wall. Control points are marked with pink paint.

B. Scanner positioned on the approach embankment next to a bridge.

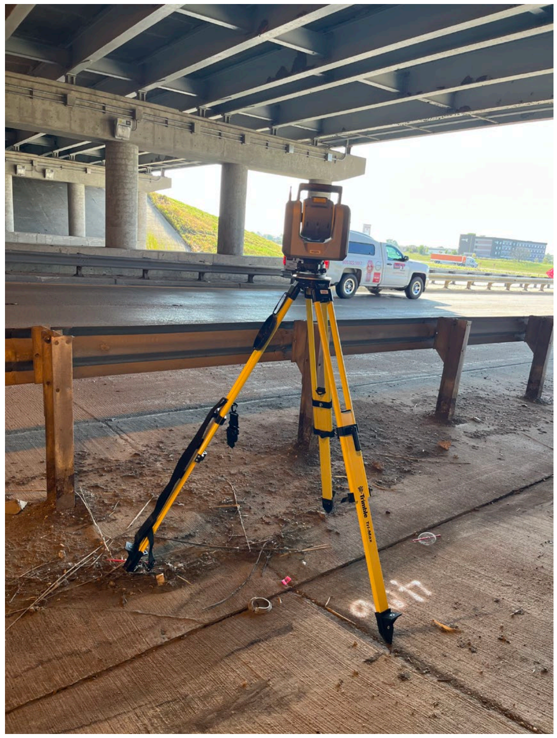

C. Scanner positioned on the shoulder underneath a bridge.

Figure 9. Photo. Example laser scanner positions for documenting impact damage to girders.

Source: Figure 9-A and Figure 9-B courtesy of Robert Stickelmaier, IDOT

Figure 10 shows an example controller input screen for a Trimble SX10 scan of a steel truss bridge. At each scan location, the operator selects whether to perform a “full dome” scan or a “polygon” field-of-view scan. For a full dome scan, the laser scanner captures points in all directions over an entire sphere (excluding points directly underneath the scanner). A full dome scan is the most time-intensive setting and, therefore, is used only when necessary, such as when scanning underneath a bridge to document the entire bridge width. For a polygon area scan, the operator selects the desired field of view using the scanner controller and camera. The camera rotates in real time when selecting the field of view on the controller. A polygon scan is typically used when scanning from the side of bridge or when only documenting select girders on a bridge.

For each scan, the operator also selects the level of detail. The Trimble SX10 has four levels of detail: coarse, standard, fine, and very fine. For an object 50 m (164 ft) from the scanner, the point spacings for the resulting point cloud are 50 mm, 25 mm, 12.5 mm, and 6.25 mm (2.0 in., 1.0 in., 0.5 in., and 0.25 in.) for the coarse, standard, fine, and very fine settings, respectively. Bridge scans are often performed from much closer distances, which considerably decreases the point spacing. For a full dome scan underneath a bridge, the coarse setting is typically used. A full dome scan on the Trimble SX10 typically takes about 12–15 minutes using the coarse setting, but the time increases to about an hour for the standard setting and 12 or more hours at the fine setting. For a polygon field-of-view scan, the standard or fine settings can often be used because the time required is not prohibitively long. The lowest detail setting needed to adequately capture the geometry is typically selected. After the field of view and level of detail have been selected, the scanner typically shows an estimate of the time required and number of points.

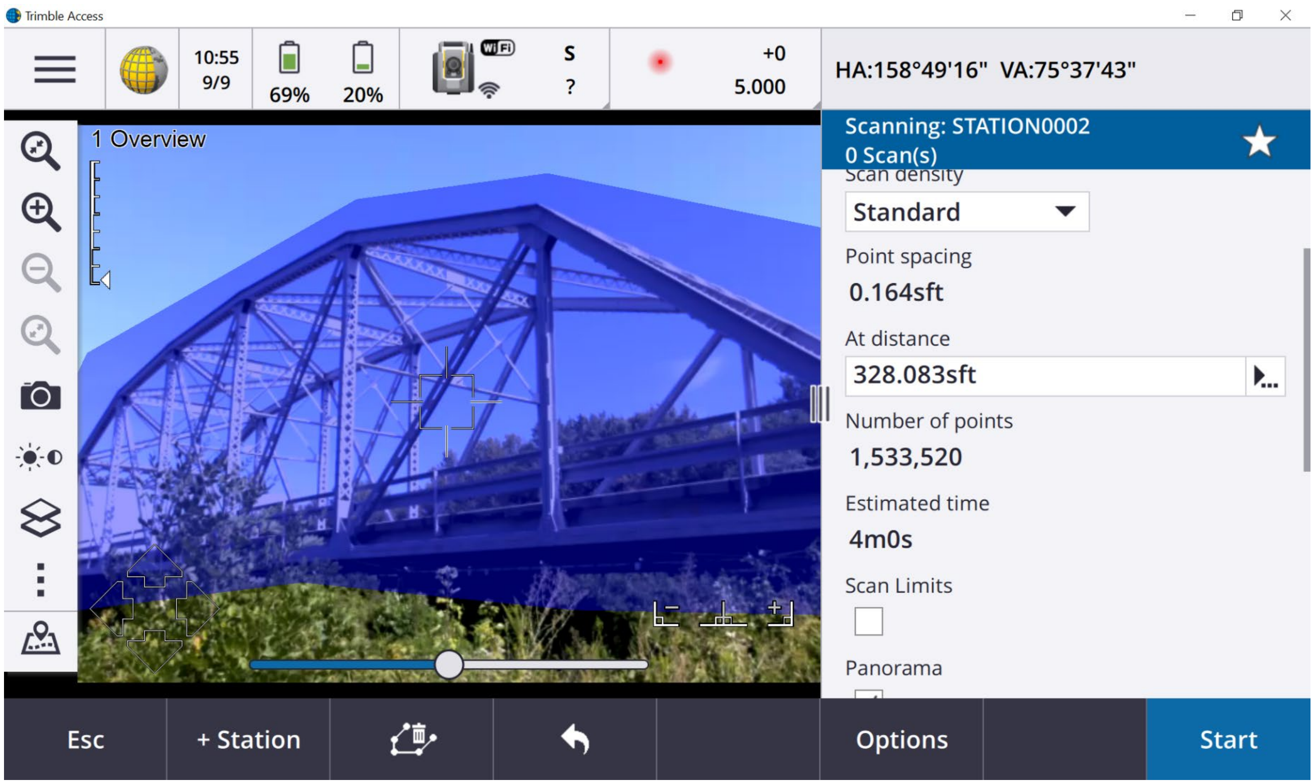

Figure 10. Illustration. Example controller screen for selecting scan options. A polygon scan is selected for a steel truss bridge.

Modern scanners such as the Trimble SX10 have a camera attachment and can automatically colorize the resulting point cloud (assigning a color to each point). Although colors are not used for the processing procedure below, a colorized point cloud can be visually appealing and help inspectors distinguish between elements. After the operator begins the scan, the scan runs automatically, and the scan progress can be monitored on the controller, as shown in Figure 11.

Overall, completing a full bridge scan (including setting control points and performing the scan) is approximately one full day of work. Setting control points typically takes three to four hours, and scanning the bridge takes three to four hours. If only one or two beams need to be documented, the duration could be reduced to about three hours total (one hour for setting control points and one to two hours for completing the scan). These durations are estimates and may vary based on site conditions, crew expertise, and equipment selected.

The initial scan result can be preprocessed in software such as Trimble Business Center (TBC). TBC automatically recognizes various features such as the road, vehicles, light posts, and vegetation; irrelevant features can be easily deleted. The point cloud file can be saved in various proprietary or open-source formats for further analysis using other software.

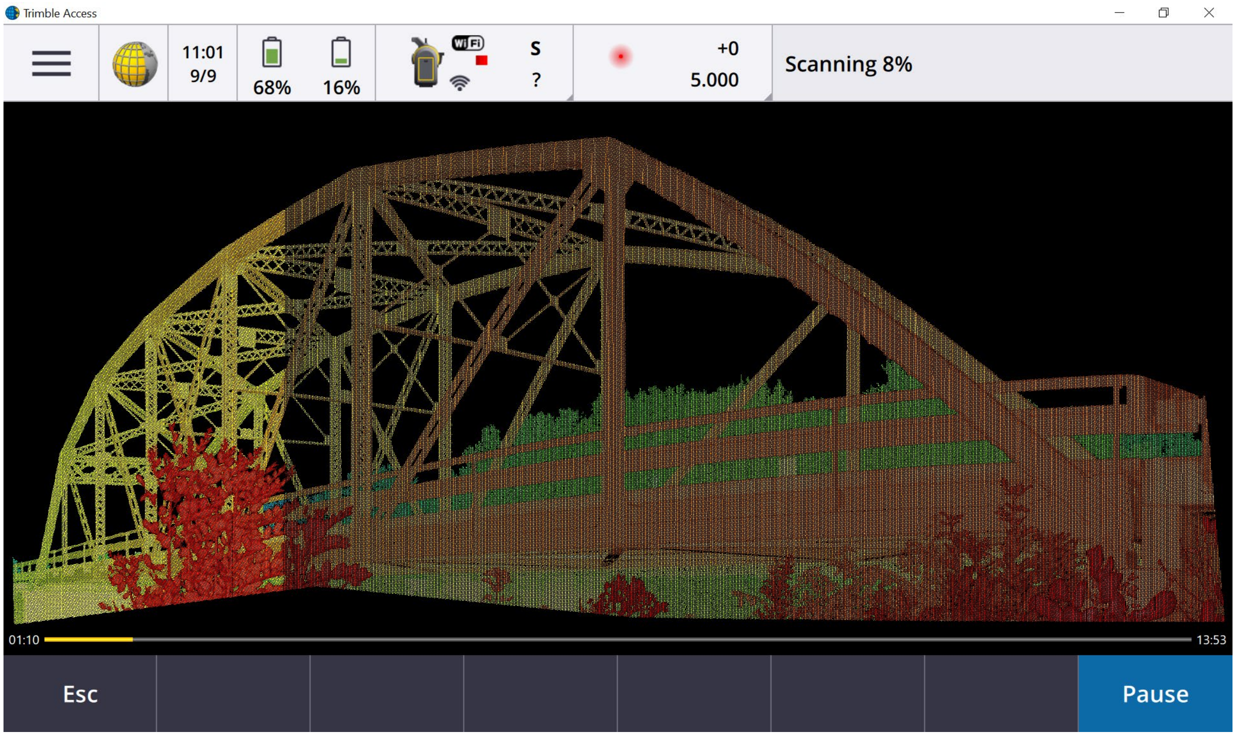

Figure 11. Illustration. Controller screen showing live progress during a laser scan of a steel truss bridge. Brighter colors indicate higher point density at this stage of the scan.

Source: Courtesy of Robert Stickelmaier, IDOT

POINT CLOUD PROCESSING FOR DISPLACEMENT MEASUREMENTS

The following sub-sections detail a procedure for measuring the horizontal and vertical displacements of a steel I-section flange from point cloud data. The proposed procedure follows a modular approach and includes several automated steps to improve practicality. The procedure description focuses on displacement measurements for the bottom flange of a highway bridge steel I-girder subject to impact damage. (The term “bottom flange” may also include cover and/or splice plates, if present.) Displacements of the bottom-flange lower-surface left corner, centerline, and right corner are measured, as illustrated in Figure 12. The procedure may also be used for displacement measurements of other damaged and undamaged I-sections, such as exposed I-columns in parking garages, as discussed in Schissler et al. (2026b). For damaged girders, the bottom-flange lower-right corner is defined as the corner that has been displaced away from the original (vertical) web location. For undamaged girders, either lower corner can be selected as the right corner. Within a given cross-section, measurements are first computed for the right corner, and measurements of other points on the bottom flange are then computed from there.

Figure 13 illustrates the coordinate system for displacement measurements. The procedure is designed to process a single point cloud in Cartesian coordinates. Scans performed from different vantage points must be preregistered to a consistent global coordinate system. To perform measurements for multiple members (or multiple spans of a single member), the procedure needs to be performed in its entirety for each member.

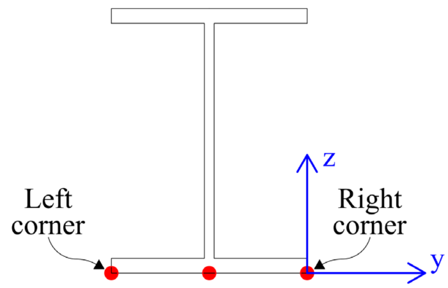

A. Key points for an undamaged cross-section

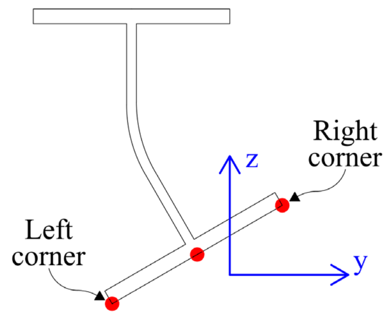

B. Key points for a damaged cross-section

Figure 12. Schematic. Undamaged and damaged girder displacements, with the coordinate system selected so displacement of the right corner is equal to zero in the undamaged condition. Displacements of the bottom-flange left corner, centerline, and right corner are measured.

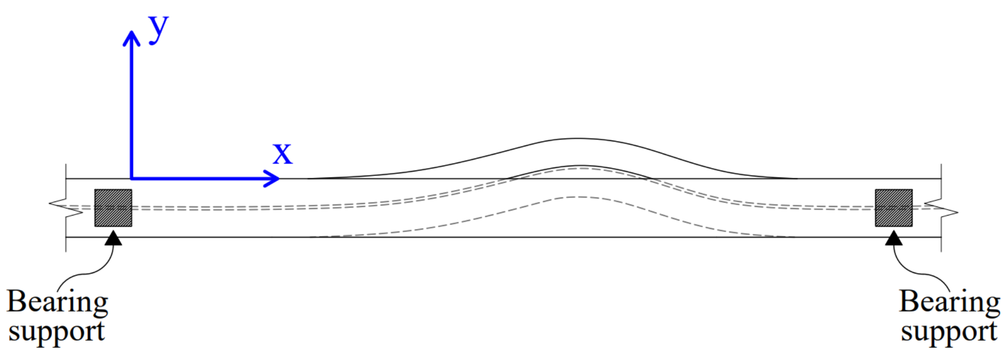

A. Top view

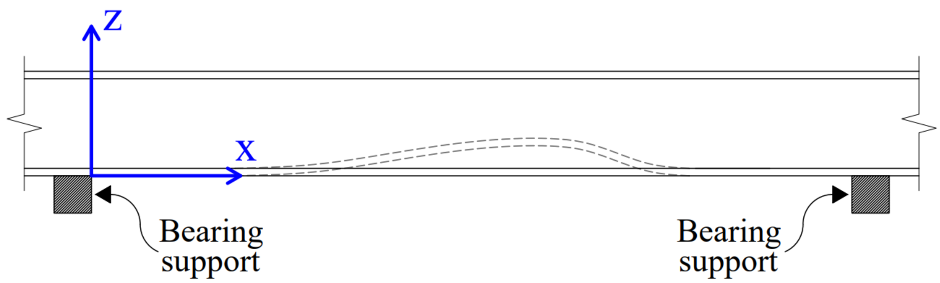

B. Side view

Figure 13. Schematic. Girder orientation for damage measurements.

There are a few important assumptions incorporated in this point cloud processing procedure, based on observations from bridge strike photographs, documentation, and laser scans provided by IDOT. Only one span is considered at a time, and all displacements are measured relative to a line connecting the respective flange cross-sectional reference points at the face of supports for the span. (Based on discussions with IDOT, impact damage extending into neighboring spans or causing displacement at the supports is not typically a concern.) Additionally, the procedure assumes that the surface of the bottom flange remains as an approximately straight line at any given girder cross-section location throughout the impact damage region, which is representative for most cases studied (Schissler 2024). A manual correction approach for bent or curved flanges is described in Schissler et al. (2026b).

For a complete description of the procedure, including a case study with example input values (for manually adjusted parameters) and a detailed discussion of the procedure strengths and limitations, one can see Schissler et al. (2026b). The procedure comprises six main steps, as discussed in the subsequent sub-sections. Automation throughout the procedure, especially in the longitudinal alignment and coordinate measurement steps, makes it feasible to measure displacements along an entire girder span in less than an hour. Each module after girder segmentation runs automatically once its manual parameters are adjusted, and results can be fine-tuned as needed by adjusting each module's manual parameters.

Girder Segmentation

The initial steps in the point cloud processing algorithm are segmenting the girder span of interest and approximately positioning the coordinate system. The researchers used CloudCompare version 2.12.4, an open-source software, to perform this step. Other software may also be suitable. The segmentation step does not need to be precise, and points corresponding to the deck, railings, cross-frames, or other components above the girder will not affect the final measurement result. Importantly, because the measurements are taken relative to the girder position at the face of supports, the supports at the ends of the girder span must be preserved, as illustrated in Figure 13. The coordinate system is positioned such that the girder longitudinal direction is approximately parallel to the global *x*-axis, the damage is toward the positive *y*-direction, and the origin is located near the girder. A qualitative approximation is sufficient because the orientation will be refined in a later step.

Outlier Removal

After segmentation, outlier removal is performed for the point cloud. Although recent scanning equipment often has accuracy and precision at the millimeter level (Seo et al. 2021), noise is still typically present in point cloud data, even under ideal conditions. Potential noise sources include the mixed pixel phenomenon, where a single laser beam is reflected to the scanner by two surfaces (Wang et al. 2016); errors caused by reflective surfaces (Wang and Feng 2014); and inaccurate capture of sharp corners. Removing outlier points improves the efficacy of subsequent steps in the overall procedure.

In general, automatic optimization of outlier removal is a challenging topic of current research. Han et al. (2017) and Chen and Shen (2018) reviewed outlier removal methods proposed before 2018, and

Zhou et al. (2022) reviewed more recent methods, including deep learning–based approaches. Although the best choice of outlier removal technique and associated parameters depends on the specific point cloud characteristics, an appropriate method for this procedure only needs to remove obvious outlier points. Region-averaging methods such as simple voxel downsampling are not recommended because they tend to reduce data precision, detracting from measurement accuracy. The radius outlier removal method included in the Python Open3D library (Zhou et al. 2018) was implemented for most girders studied. This simple, yet effective method removes points with less than n_{nb} points contained in a sphere of radius r around them. The statistical outlier removal method presented by Rusu et al. (2008) was also investigated but was often less effective due to sensitivity to variations in point cloud density.

Longitudinal Alignment

Girder flange displacements are measured with respect to flange positions at the faces of the supports, so the coordinate system must therefore be aligned with the girder longitudinal direction. Approximate alignment was performed in the girder segmentation step described previously, but a more precise and accurate alignment is necessary. For the longitudinal alignment step, the terms "north" and "south" refer to the ends of the girder with the minimum and maximum *x*-coordinates, respectively. For Girder 18, the north and south girder ends correspond to the center and south piers, respectively. The alignment process, illustrated in Figure 14, is automatic and comprises an iterative process of rotations in the *x*-*z* and *x*-*y* planes; a maximum number of iterations, i_{max}, can be specified. Additional details for vertical and horizontal operations are included in Schissler et al. (2026b).

Coordinate Measurements

After proper coordinate system alignment is established, the girder bottom-flange lower-right corner horizontal and vertical displacements can be obtained. The coordinate measurement step combines three key techniques: cross-sectional slicing, voxelization, and RANSAC regression. A manually specified number of cross-sectional slices are created at equal intervals along the girder length. Every point in the point cloud is included in exactly one slice, and each slice is labeled by its central coordinate in the longitudinal (*x*-) direction.

The coordinate measurement procedure begins at the slice with the minimum longitudinal coordinate and progresses automatically through Steps 1–6 (within the *y*-*z* plane) for all slices along the girder length. For each slice, the following steps are performed:

1. Identify points in the slice located within the 2D bottom-flange region from the previous slice.
2. Fit a RANSAC line to the points identified in Step 1.
3. Identify the horizontal coordinate of the bottom-flange lower-right corner as the maximum coordinate of the bottom-flange region points.
4. Compute the bottom-flange lower-right corner vertical coordinate using the horizontal coordinate and the RANSAC line equation.
5. Compute the location of the bottom-flange lower-left corner and centerline points using the RANSAC line equation and the flange width.

6. Use a 2D voxel scheme to identify the bottom-flange region (in the *y-z* plane) based on RANSAC inliers of the current slice.

This approach effectively traces the bottom-flange region along the length of the girder, even in the damaged region, because any change in bottom-flange location from one slice to the next is relatively small. RANSAC linear regression (Fischler and Bolles 1981), as implemented in `scikit-learn` (Pedregosa et al. 2011), was selected to generate the straight line representing the lower surface of the bottom flange. RANSAC regression is robust to outliers, so any points corresponding to other features (such as the web) will not affect the resulting line as long as most points in the bottom-flange region are on the lower surface of the bottom flange.

Figure 15 presents selected cross-sectional slices along the length of IDOT bridge SN 084-0014 Girder 18. Figure 15-B shows a cross-section at a cross-frame near the impact, illustrating that the bottom-flange voxelization excludes extraneous points corresponding to the cross-frame. Figure 15-D illustrates that the RANSAC fitting method is still effective for a slice containing a bolted splice plate.

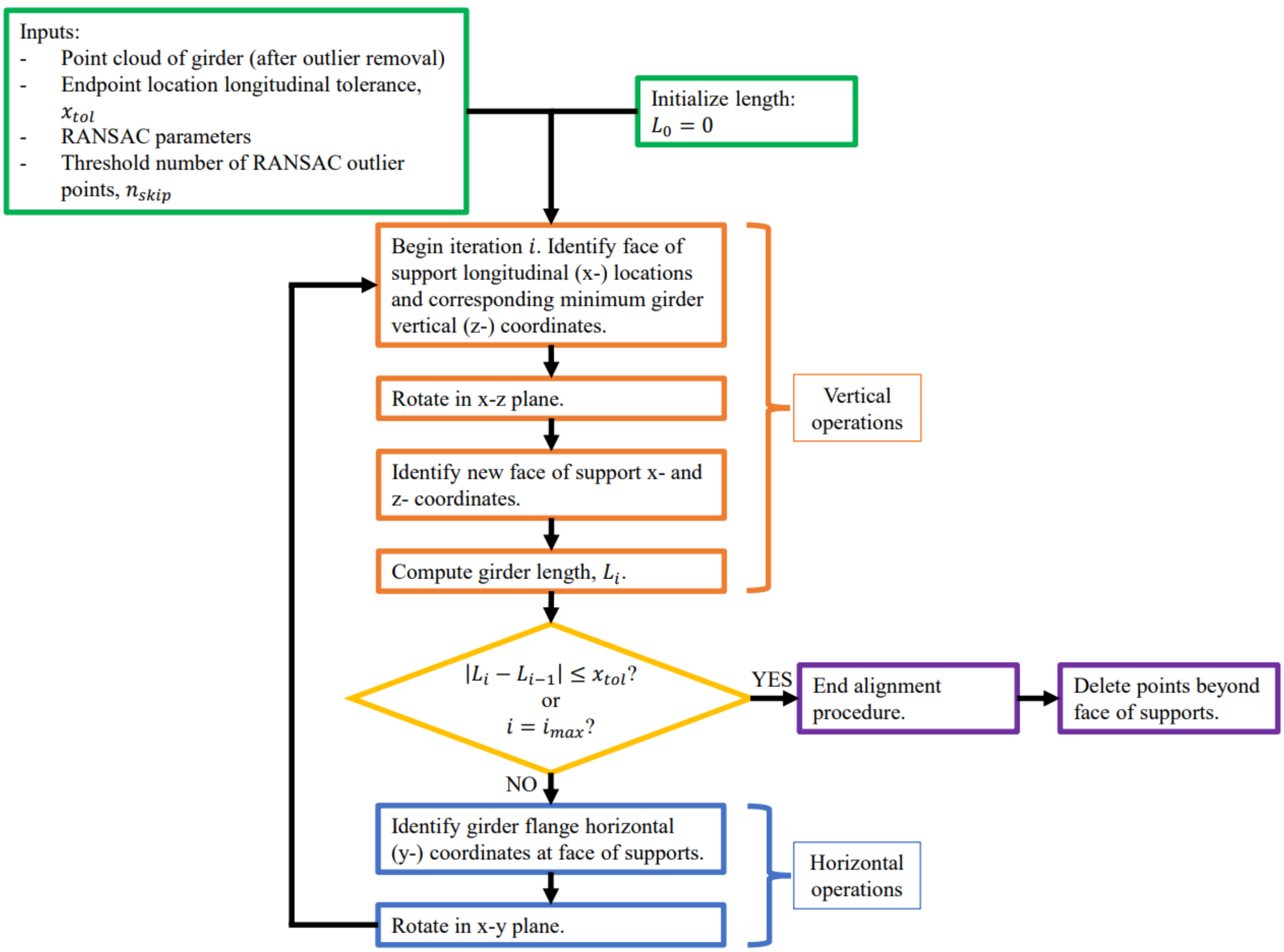

Figure 14. Diagram. Schematic flow chart of girder alignment process. The first iteration corresponds to $i = 1$.

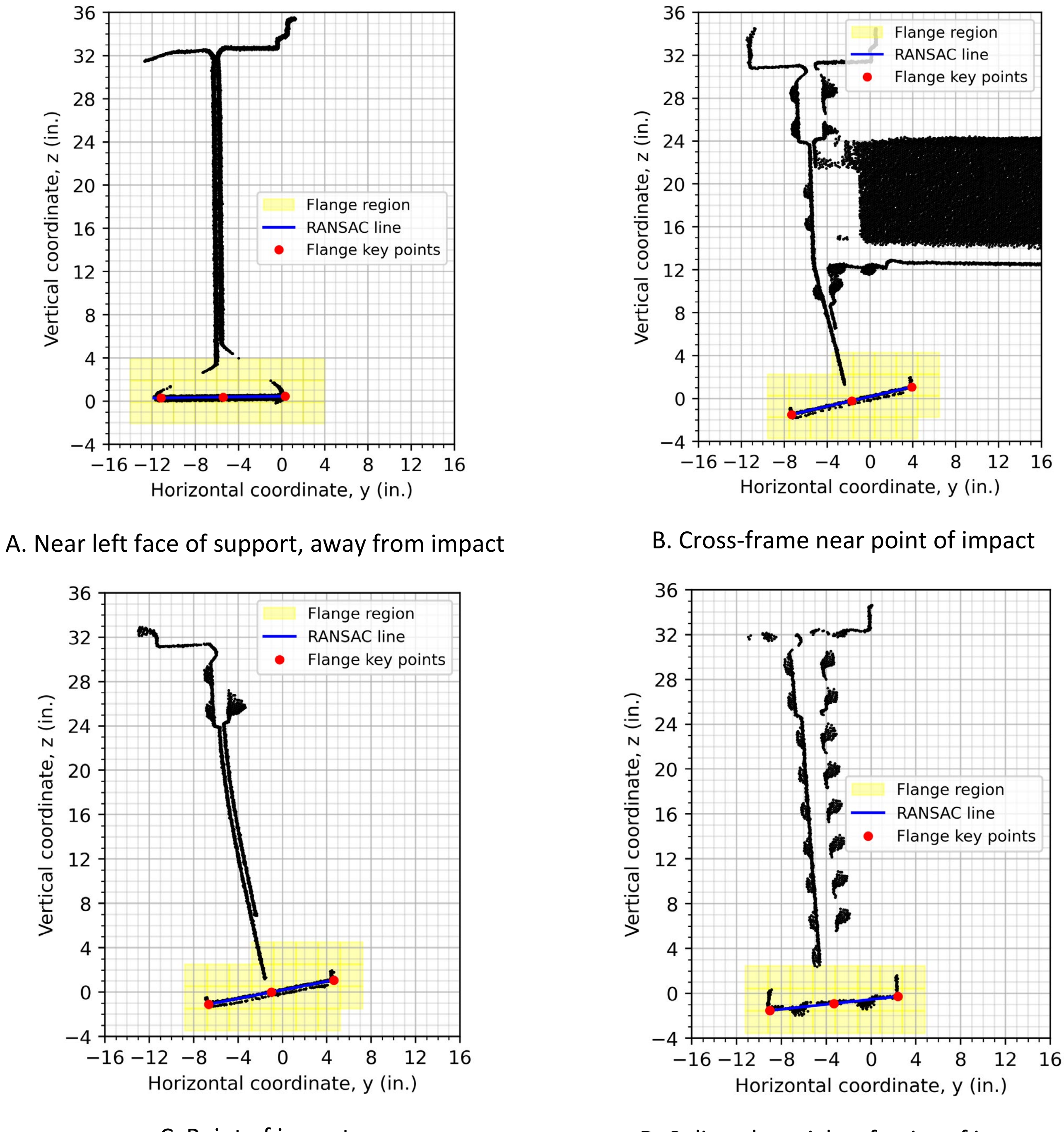

A. Near left face of support, away from impact

B. Cross-frame near point of impact

C. Point of impact

D. Splice plate right of point of impact

Figure 15. Graph. Selected cross-sectional slices from point cloud of SN 084-0014 Girder 18 (1 in. = 25.4 mm).

The horizontal and vertical coordinates detected over the entire length of the damaged span are shown in Figure 16 for the bottom-flange lower-right corner of IDOT bridge SN 084-0014 Girder 18. The horizontal measurement endpoints are very close to zero but may deviate slightly if the slice width for measurements is different from the slice width used for horizontal alignment. The vertical measurement endpoints may deviate further from zero due to differences between the approaches for the alignment and coordinate measurement steps. This deviation will be corrected in subsequent steps.

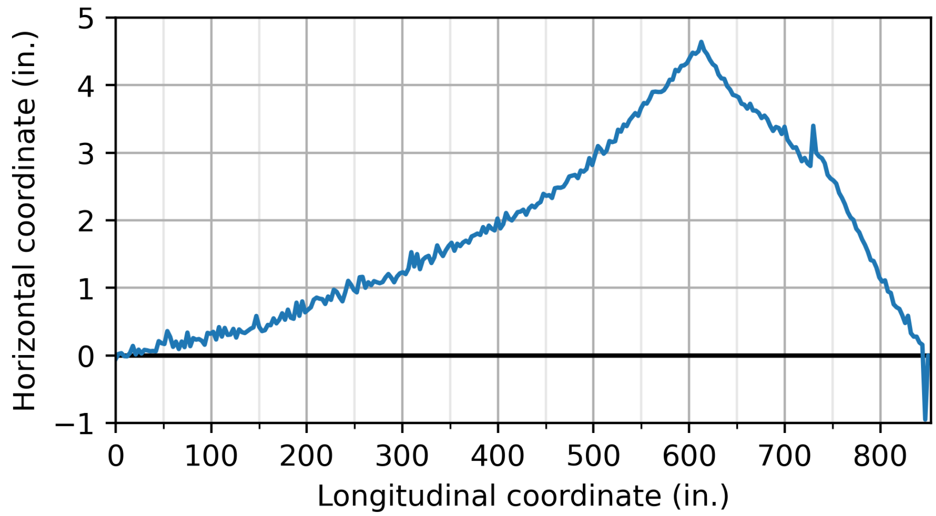

A. Horizontal coordinate

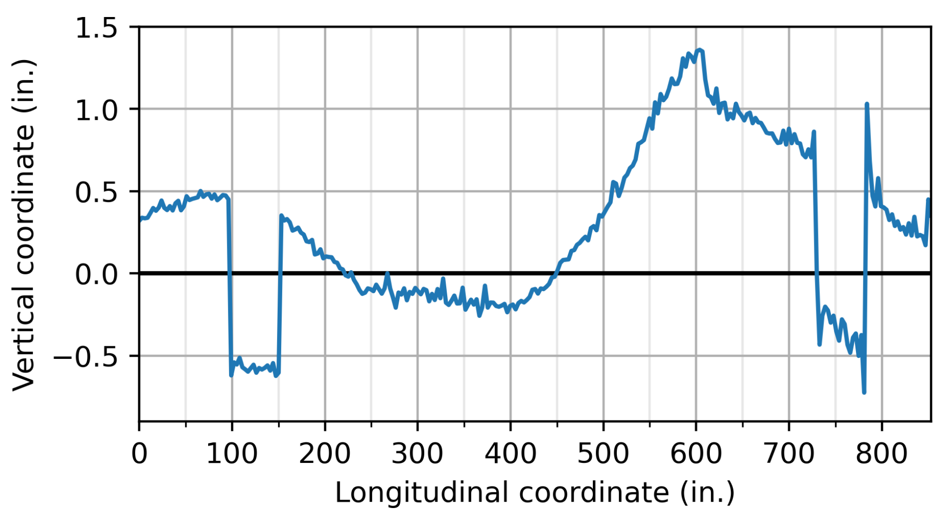

B. Vertical coordinate

Figure 16. Graph. Overall horizontal and vertical coordinates of the bottom-flange lower-right corner measured from the laser scan for bridge SN 084-0014 Girder 18. Vertical coordinate endpoints have not yet been adjusted (1 in. = 25.4 mm).

Adjust for Cover/Splice Plates

Based on previous steps, the resulting coordinates of the bottom-flange lower corners and centerline in each cross-section may include cover and/or splice plates, which do not extend over the entire length of the span. The thickness of cover/splice plates therefore affects vertical coordinate measurement. If there are no cover plates at the supports and the impact is not near a splice, then the maximum displacement can be obtained directly without adjusting for cover/splice plates. However, to obtain a smooth displacement curve over the length of the girder, measurements must be relative to the girder initial position, including any plates that are present. A cover plate at one support but not the other will also affect the measurement values along the span.

To correctly quantify how much the girder bottom flange has moved from its initial position, the vertical coordinate resulting from alignment and coordinate measurement steps performed on an undamaged girder must be subtracted from the measured vertical coordinate of the damaged girder. When a laser scan of the undamaged girder is not available, a theoretical undamaged vertical coordinate measurement can be computed by assuming a perfectly straight undamaged girder and estimating cover/splice plate locations and thicknesses from construction drawings or the point cloud of the damaged girder.

Figure 17 illustrates the adjustment step for a vertical displacement measurement, using the bottom-flange lower-right corner of SN 084-0014 Girder 18 as an example. For Girder 18, there are two splice plates in the damaged span, each with 25.4 mm (1 in.) thickness and 1.37 m (54 in.) longitudinal length. From the construction drawings, the splice plate longitudinal (x-) locations are from 2.51 m (99 in.) to 3.88 m (153 in.) and 18.52 m (729 in.) to 19.89 m (783 in.). The theoretical undamaged coordinate is plotted in Figure 17-A. Longitudinal locations of plate ends agree well with the locations of abrupt deviations in a measured vertical coordinate. In girders with a cover plate over the support at one end, but not at the other, a rotation of the theoretical undamaged coordinate would be necessary so both coordinate ends have values of $z = 0$ (for consistency with point cloud alignment).

Before adjusting for cover/splice plates, the measured vertical coordinate data are rotated so the endpoints have values of $z = 0$. Next, the relative vertical displacement of the girder section corner is computed by subtracting the theoretical undamaged position in Figure 17-A from the measured damaged position. The resulting curve, shown in Figure 17-B, appears to show increased noise around the locations of the plate ends. In slices at these locations, the bottom-flange region may include points on both the plate and bottom surface of the flange of the W-section, resulting in a RANSAC line that represents neither surface. For Girder 18, the additional large jump around $x =$ 19.94 m (785 in.) is attributed to a few sparse slices at that location. Overall, except for these features, the resulting curve reflects the expected geometry. The adjustment step is also performed for the bottom-flange lower-left corner and centerline.

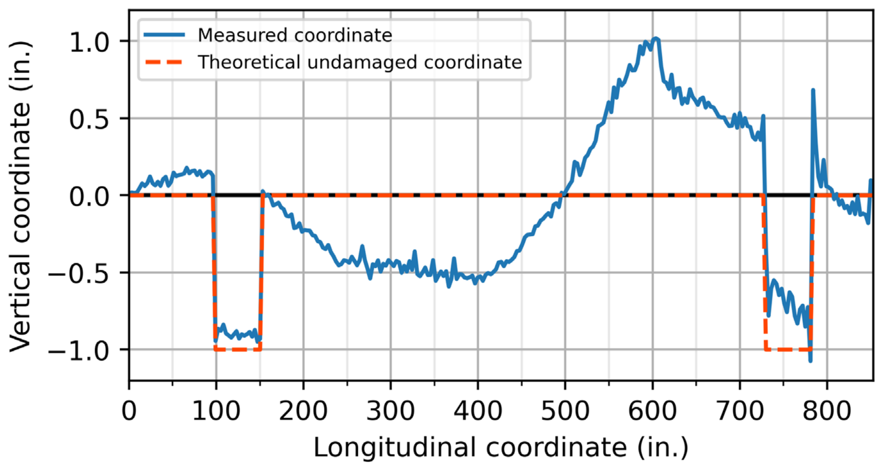

A. Measured coordinate, rotated such that endpoints have zero displacement, compared with initial undamaged vertical coordinate of bottom flange.

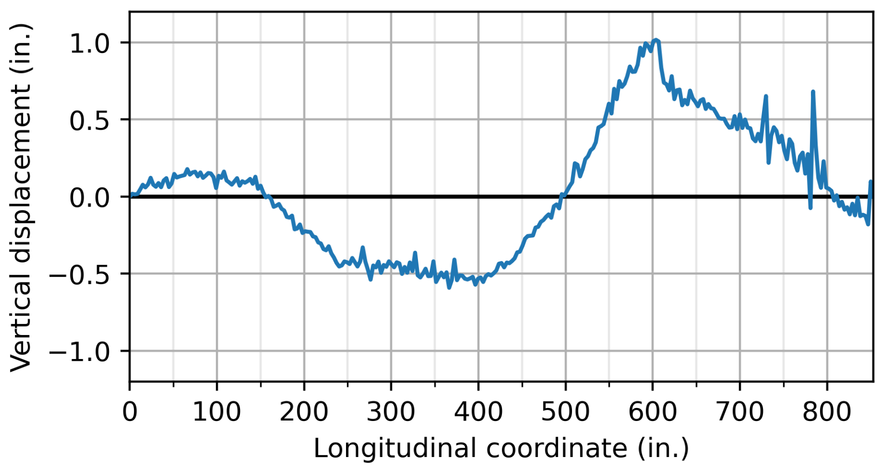

B. Vertical displacement relative to initial position.

Figure 17. Graph. Cover and splice plate adjustment process for bridge SN 084-0014 Girder 18 bottom-flange lower-right corner vertical displacement measurements (1 in. = 25.4 mm).

Noise Removal

As observed in Figure 16 and Figure 17, the resulting measurements include some high-frequency noise not representing any physical behavior, which may be attributed to errors from both the laser scan and measurement processes. Eliminating noise yields a more realistic representation of girder geometry. To obtain a smooth curve, a bidirectional low-pass Butterworth filter is applied to the measurement data for the bottom-flange lower corners and centerline. The longitudinal (*x*-) coordinate and measurement interval are analogous to time and sample interval, respectively, for a filter applied to time-series data. The filter order, threshold frequency, and extent of zero-padding can be adjusted to improve the result. Example parameter values are included in Schissler et al. (2026b).

The filtering step may underestimate the maximum displacement. This effect is usually more significant for girders with larger displacements. Judgment should therefore be exercised to assess whether the result is acceptable. To correct the underestimation, one effective approach is implementing a spline between the maximum (impact) displacement and the closest inflection point (in the filtered data) on each side of the maximum. Figure 18 illustrates the results for the SN 084-0014 Girder 18 right corner. The spline slope is specified as continuous with the rest of the filtered data at the inflection point and zero at the maximum displacement location. Finally, the curve is rotated such that the endpoints have a displacement value of zero. Figure 19 shows the final smooth data for the SN 084-0014 Girder 18 right corner, with the same rotation applied to the noisy data. The maximum right-corner horizontal and vertical displacements are 119 mm (4.7 in.) and 25.4 mm (1.0 in.), respectively.

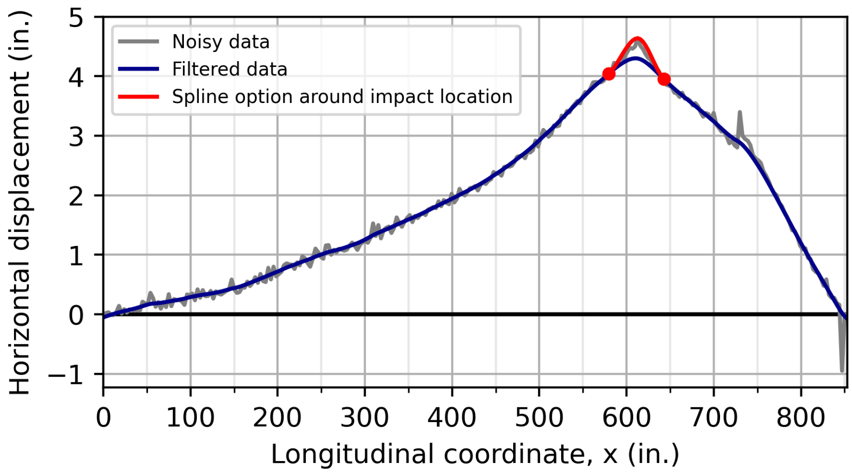

A. Horizontal displacement

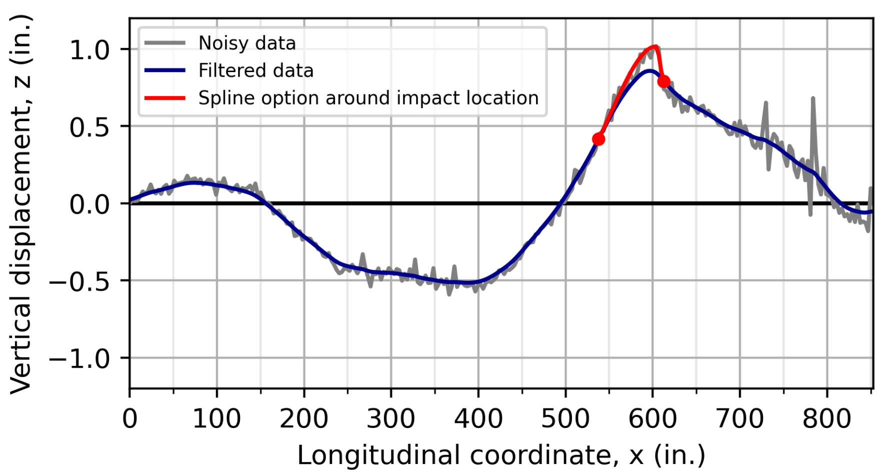

B. Vertical displacement

Figure 18. Graph. Original and filtered displacement measurements for bridge SN 084-0014 Girder 18 bottom-flange lower-right corner (1 in. = 25.4 mm).

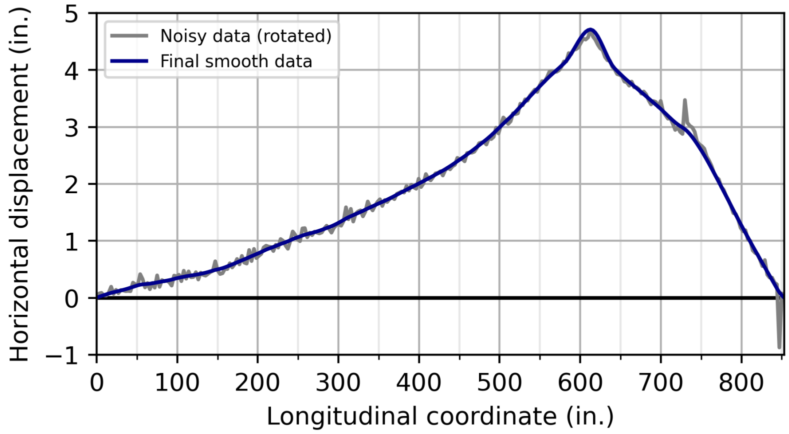

A. Horizontal displacement

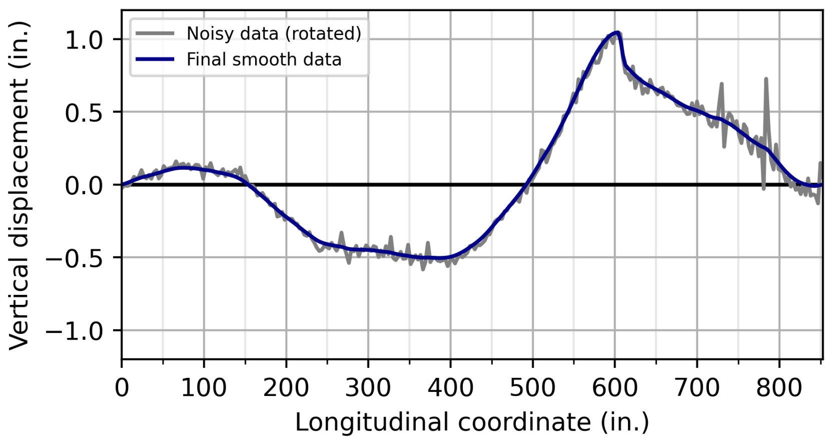

B. Vertical displacement

Figure 19. Graph. Original and smooth data for bridge SN 084-0014 Girder 18 bottom-flange lower-right corner displacement measurements, after adding a spline near the impact point and rotating data such that the endpoints are at zero displacement (1 in. = 25.4 mm).

EXAMPLES OF DISPLACEMENT MEASUREMENTS

Point cloud displacement measurements from four damaged IDOT bridges are included in this section. For each bridge, measurements for a damaged girder are presented alongside measurements for a girder having minimal to no damage. The undamaged girder location on each bridge is immediately adjacent to the damaged girder, except for in bridge SN 041-0067, where the immediately adjacent girders were damaged as well. Damage photographs for each case are included in Appendix A.

From studying 37 girders with minor to no damage, a typical undamaged girder may have horizontal and vertical displacements of up to approximately 25 mm (1 in.). Although vertical displacements of some undamaged girders resembled typical dead-load deflections, others had upward vertical displacements (despite no specified camber). Bridge retrofits are one possible explanation for this observation. For example, as shown in Figure 22, SN 016-0918 Girder 2 is undamaged but exhibits an upward deflection of about 13 mm (0.5 in.). The construction documents indicate that rehabilitation included a jacking sequence to raise all girders by 181 mm (7.13 in.).

Displacements of an undamaged girder on the same bridge can provide insight when the damaged girder initial position is unknown. For large impact damage displacements, the initial position is less significant, as illustrated for SN 041-0067 Girder 6 in Figure 23. However, for smaller impact damage displacements, such as the vertical displacement of SN 084-0014 Girder 18 in Figure 20, an initial displacement of 25 mm (1 in.) is of a similar magnitude to the damage displacement and may be significant.

Key bridge information is summarized in Table 1. When available, hand measurements performed by IDOT are also included for each damaged girder. Procedure results can be further validated by comparing the girder length (between supports) from the longitudinal alignment step to the expected length from the construction drawings. As reported in Table 1, the difference between measured and expected length ranges from 0.04% to 0.23%, representing an average difference of 28 mm (1.1 in.). Schissler et al. (2026b) includes a more detailed discussion of the implications of the point cloud measurement procedure.

Table 1. Summary of Bridges for Which Example Measurements Are Included

IDOT Bridge Number	Location	Size of Selected Girders	Span Lengths (Damaged Span indicated with an Asterisk)	Difference in Span Length (Point Cloud vs. Plans)
SN 084-0014	Springfield, IL	W33x130	15.4 m, 22.3 m, 22.3 m*, 12.2 m (607 in., 877 in., 877 in.*, 482 in.)	0.06% (Girder 18) 0.12% (Girder 17)
SN 084-0077	Springfield, IL	W27x114	11.9 m, 14.2 m, 19.3 m*, 12.3 m (469 in., 558 in., 758 in.*, 484 in.)	0.22% (Girder 19) 0.23% (Girder 18)
SN 016-0918	Glenwood, IL	W30x116	13.7 m, 17.1 m, 17.1 m*, 13.7 m (540 in., 675 in., 675 in.*, 540 in.)	0.12% (Girder 1) 0.21% (Girder 2)
SN 041-0067	Mt. Vernon, IL	33WF118	19.9 m, 19.9 m* (784 in., 784 in.*)	0.04% (Girder 6) 0.15% (Girder 2)

Bridge SN 084-0014

IDOT bridge SN 084-0014 carries I-55 southbound over Sangamon Ave (IL 54) in Springfield, Illinois. Bridge SN 084-0014 was damaged by a vehicle traveling eastbound on Sangamon Ave (IL 54) in a hit-and-run incident on November 17, 2020. An inspection indicated damage to the west fascia girder (Girder 18). The bridge remained open to traffic. The primary concern was reduction in capacity due to lack of composite action in the impacted area, but engineers determined that the girder had sufficient reserve capacity. Girder 18 has been struck previously and received zipper repairs in 2015 and 2017, and it was mechanically straightened earlier in 2020. For this damage incident, IDOT planned to straighten the girder because the deflection was spread over a significant longitudinal distance. If subject to further impact, a zipper replacement would likely be required.

Figure 20 presents the horizontal and vertical displacements for Girder 18 (damaged) and Girder 17 (minor to no damage). Inspectors only performed hand measurements for the horizontal direction, and a 122 cm (4 ft) longitudinal interval was used. Photographs show that the damage extends over most of the span length, with significant localized concrete deck spalling over the impact point.

The horizontal displacement profile in Figure 20-A is of a typical shape, with the left corner, flange centerline, and right corner measurements all similar to the hand measurements and consistent with a global deflection mode. The hand measurement documents a 16 mm (5/8 in.) horizontal displacement over the centerline of the south pier (slightly past the maximum longitudinal coordinate in Figure 20-A, which corresponds to the face of the south pier bearing), so the stringline reference extended past the pier centerline. Although the standard point cloud measurement procedure cannot measure displacement over a support, discussions with IDOT indicated that displacement over the bearing support is not usually a concern, so this inspection result is uncommon.

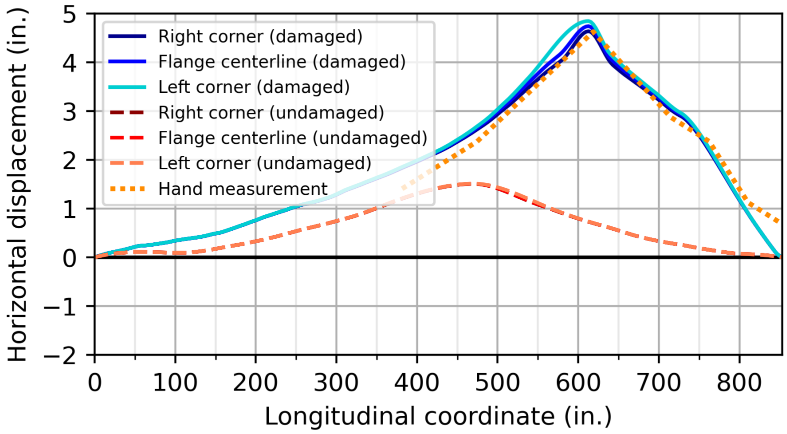

A. Horizontal displacement

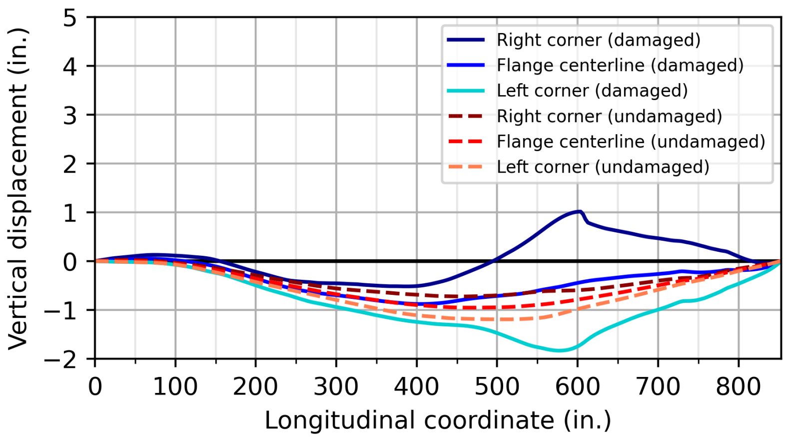

B. Vertical displacement

Figure 20. Graph. Horizontal and vertical displacement measurement results for IDOT bridge SN 084-0014 Girders 18 (damaged) and 17 (undamaged) (1 in. = 25.4 mm).

Bridge SN 084-0077

IDOT bridges SN 084-0076 and -0077 carry I-72 over 6th St/BUS 55 in Springfield, Illinois. Bridge SN 084-0076 (girders 1–9) carries I-72 westbound, and SN 084-0077 (girders 10–19) carries I-72 eastbound. Twelve girders on bridges SN 084-0076 and -0077 were impacted in a hit-and-run incident on September 9, 2024. A vehicle traveling northbound on 6th St/BUS 55 damaged the bridge in the second span from east. Girder 19 was impacted most severely and is highlighted below. The other impacted girders experienced less severe damage such as scrapes and minor deflections. When the impact was discovered, IDOT closed the I-72 eastbound shoulder over Girder 19. The shoulder was later reopened after engineers determined that Girder 19 had sufficient reserve capacity. In October 2025, a zipper repair was performed for Girder 19, and an adjacent diaphragm was replaced. The 11 other damaged girders were mechanically straightened and/or strengthened.

SN 084-0077 Girder 19 is the south fascia girder, and the second span from east was impacted. The first interior girder (Girder 18) was undamaged and is included for comparison. Both girders have a composite design in the middle 9.8 m (32 ft) of the relevant span. Figure 21 shows point cloud measurements and hand measurements for Girder 19. The minimum longitudinal coordinate corresponds to the west end of the span. Hand measurements were taken at 61 cm (2 ft) longitudinal intervals. Based on the inspection photos, the stringline references are positioned within the damaged span, away from the impact point, and hand measurements documented the displacement of the bottom flange lower-left corner.

For horizontal displacement, the hand measurement is less than the point cloud measurement. This is expected because the stringline reference is placed within the span, whereas the point cloud measurements are relative to the supports. The point cloud measurements indicate that there is still some displacement beyond the stringline reference points. For vertical displacement, the magnitude of the hand measurement is less than that of the point cloud measurement, which is also expected due to the stringline reference locations. However, the shape of the hand measurement curve is more abrupt and has more curvature compared to the point cloud measurement of the left flange corner, which is unexpected. The point cloud and hand measurements are expected to show a more similar curvature, especially when the hand measurement reference points are far from the impact point.

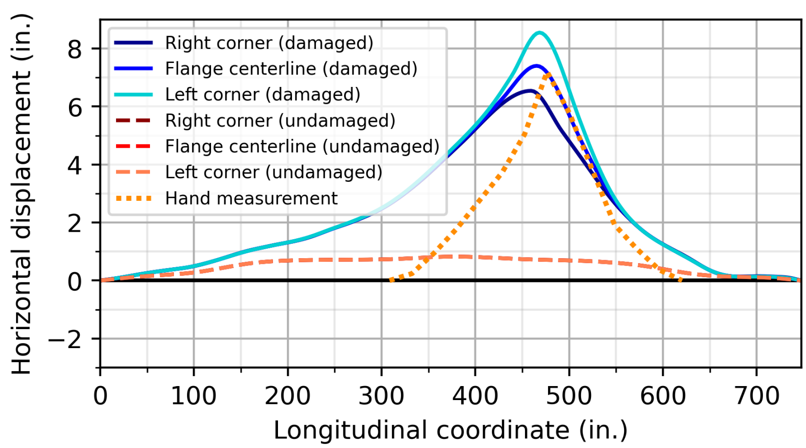

A. Horizontal displacement

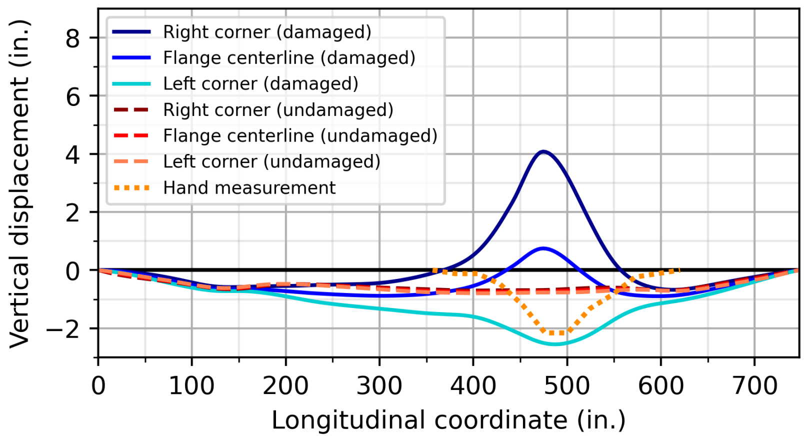

B. Vertical displacement

Figure 21. Graph. Horizontal and vertical displacement measurement results for IDOT bridge SN 084-0077 Girders 19 (damaged) and 18 (undamaged) (1 in. = 25.4 mm).

Bridge SN 016-0918

IDOT bridge SN 016-0918 carries Glenwood Lansing Road over IL 394 in Bloom Township, Illinois. Bridge SN 016-0918 was damaged in April 2021 when a truck hauling a container, traveling northbound in the right lane of IL 394, struck both the bridge and a bridge-mounted directional sign. An inspection indicated the south fascia girder (Girder 1) was damaged in the second span from east, and an adjacent diaphragm clip angle was bent. The directional sign was later removed.

Figure 22 presents the horizontal and vertical displacements for Girder 1 (damaged) and Girder 2 (undamaged). The displacement profile of Girder 1 is of a moderate magnitude and extends over the span. In the horizontal displacement point cloud measurement, there is a change in curvature around a longitudinal coordinate of 8.9 m (350 in.), where the displacement slope becomes steeper closer to the impact location. The hand measurement closely matches the shape of the point cloud measurements, suggesting the stringline references were placed far from the impact. The hand measurement of horizontal displacement is larger than the point cloud measurement, which is unexpected and could indicate that the stringline reference points were beyond the support or there was some other discrepancy in the hand measurement method.

The vertical displacement for Girder 1 does not show a pronounced peak at the impact location. Instead, the right corner curve plateaus between longitudinal coordinates of approximately 10.2 m to 12.7 m (400 in. to 500 in.), and the left corner and flange centerline displacements increase only slightly over this distance. This pattern has not been observed for other damage cases. The most probable explanation is that the directional sign, mounted to the girder in four locations near the impact, appeared to somewhat brace the girder in the vertical direction. One attachment point for this sign is to the right of the impact, and the other attachment points are to the left of the impact (at lower longitudinal coordinates), similar to the plateau extending to the left of the impact point in Figure 22-B. The hand measurement data show a slightly greater peak at a longitudinal location around 12.2 m (480 in.) but otherwise exhibit a shape similar to the point cloud data.

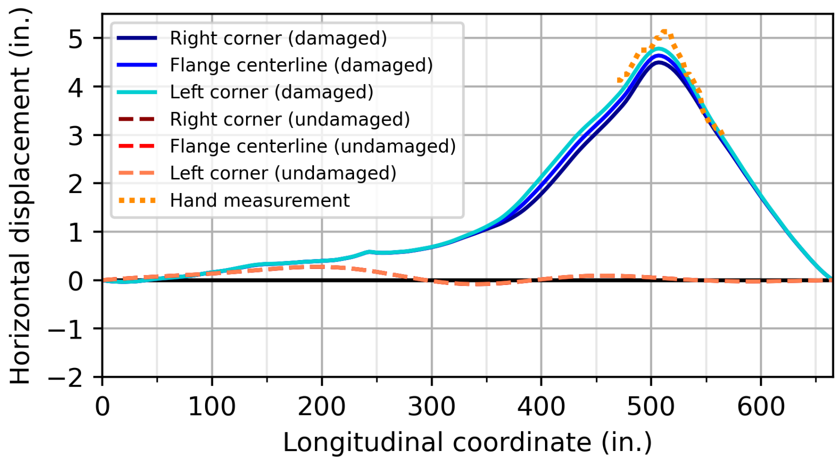

A. Horizontal displacement

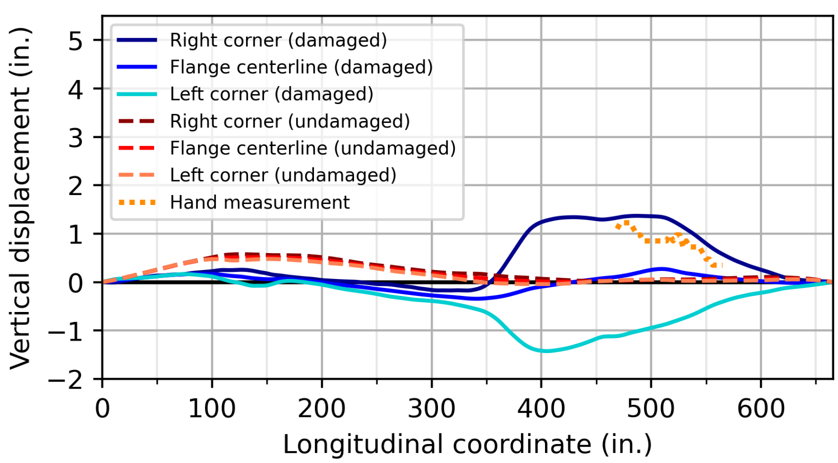

B. Vertical displacement

Figure 22. Graph. Horizontal and vertical displacement measurement results for IDOT bridge SN 016-0918 Girders 1 (damaged) and 2 (undamaged) (1 in. = 25.4 mm).

Bridge SN 041-0067

IDOT bridge SN 041-0067 carries I-64 westbound over IL 37 in Mount Vernon, Illinois. On July 18, 2023, the west span of bridge SN 041-0067 was impacted by a truck traveling southbound on IL 37 and carrying an oversized cylindrical pipe. An IDOT inspection found that Girders 1 (north fascia), 3, 4, 5, 6 and 7 (south fascia) were damaged. Damage to Girders 5 and 6 was so severe that IDOT deemed hand measurements unnecessary because the girders would need replacement. The passing lane on I-64 westbound above was closed due to the reduced capacity of Girders 5 and 6.

Figure 23 presents the horizontal and vertical displacements for Girder 6 (damaged) and Girder 2 (undamaged). Girder 6 has the largest displacements of all damaged girders studied by the researchers. The significant separation between the right corner, flange centerline, and left corner displacement curves indicates significant rotation and tilt of the girder flange. Such significant separation between the curves in the horizontal direction is especially notable.

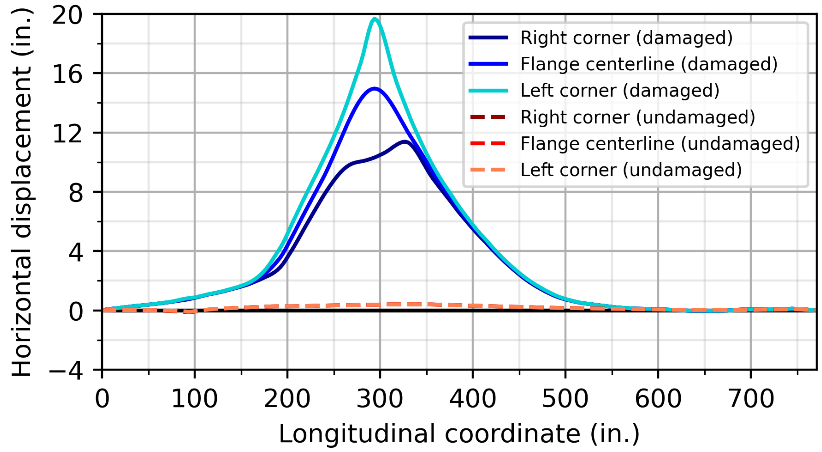

A. Horizontal displacement

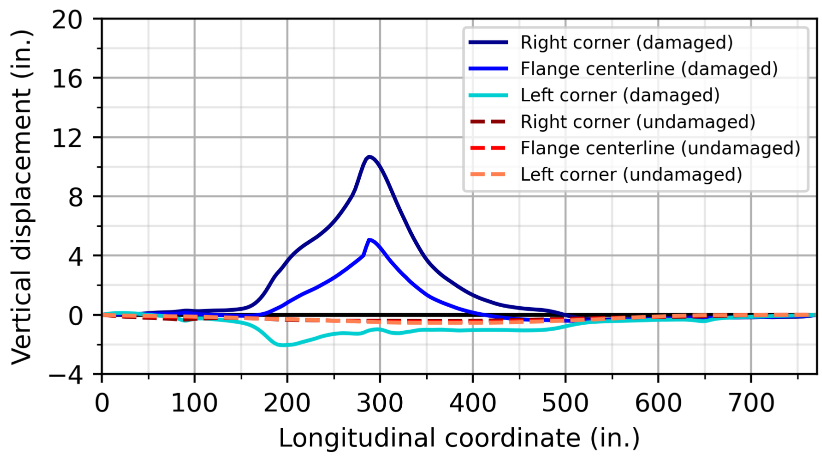

B. Vertical displacement

Figure 23. Graph. Horizontal and vertical displacement measurement results for IDOT bridge SN 041-0067 Girders 6 (damaged) and 2 (undamaged) (1 in. = 25.4 mm).

At longitudinal coordinates of about 5.1 m (200 in.) and 12.2 m (480 in.), there are diaphragms on each side of the girder. The diaphragms are offset by about 0.4 m (16 in.) from one side of the girder to the other. The horizontal and vertical displacement plots show that tilting of the Girder 6 flange was generally concentrated between these two sets of diaphragms. There is a noticeable change in curvature in the displacement plots around these locations, indicating the diaphragms had some effect on the deflected shape. In this instance, diaphragms experienced minor damage (e.g., bent clip angles) but did not punch through the girder.

CURVATURE CALCULATIONS

As discussed in Chapter 2, the IDOT *Structural Services Manual* (2024) refers to a curvature calculation procedure developed by Shanafelt and Horn (1984). The procedure in Figure 5 can be implemented for both horizontal and vertical displacements. To illustrate the feasibility of this approach for the point cloud measurements, radii of curvature were calculated for horizontal and vertical displacements at all three reference points: the bottom flange left corner, centerline, and right corner. When available, radii of curvature were also calculated from hand measurements for comparison.

For each displacement coordinate (e.g., horizontal displacement left-corner point cloud measurement), the minimum radius of curvature near the impact location is recorded. “Near the impact location” is arbitrarily defined as within a 2.54 m (100 in.) longitudinal distance from the maximum horizontal left-corner displacement measured in the point cloud. In some damage cases, the minimum radius of curvature could occur at a longitudinal location away from the impact. Future work should consider the implications of these cases for repairs. Additionally, measurements of some reference points on a damaged girder may not show local extrema at the impact location. For example, the vertical displacement of the SN 084-0014 Girder 18 centerline (see Figure 20) does not appear to have sharp curvature at a local maximum. Considering radii of curvature of all three reference points gives the most complete indication of the damage.

As shown in Figure 5, computing the radius of curvature requires selecting a longitudinal interval for measurements. Shanafelt and Horn (1984) recommend using a longitudinal interval of 30 cm (12 in.) for documenting the global behavior of a member and a reduced longitudinal interval of 5 to 10 cm (2 to 4 in.) for local distortions. In general, the selection of longitudinal interval affects curvature results, so engineers implementing this approach should exercise appropriate judgment. To facilitate comparison, the longitudinal interval of the hand measurements was also used for computing the curvature of the point cloud displacement measurements. When point cloud measurements were taken at a closer interval than hand measurements, the curvature was still computed at each point, but the increment length for curvature calculation (shown as L in Figure 5) in each direction is consistent with the hand measurements. For example, for SN 084-0077 Girder 19, point cloud measurements were taken at 7.6 cm (3 in.) intervals, but hand measurements are taken at 61 cm (24 in.) intervals. Therefore, the point cloud displacement radii of curvature were calculated every 7.6 cm (3 in.), using the measurements 61 cm (24 in.) to either side of the center point for the calculation in Figure 5. For SN 041-0067 Girder 6, hand measurements are not available, so an increment of 30 cm (12 in.) was used to reflect the global nature of the damage. In general, decreasing the increment length for curvature calculation to a value of approximately 7.6 cm (3 in.) results in a smaller minimum radius of curvature, capturing the typically sharp nature of the damage at the impact point. Excessively small values of increment length only cover a short longitudinal distance and may fail to capture a curvature that is on a larger scale. The increment length should be selected to reflect the scale of damage to be assessed.

Table 2 and Table 3 show minimum radii of curvature for the horizontal and vertical displacements, respectively. For the same girder, the minimum radius of curvature is not the same for the left corner, centerline, and right corner displacements. With a point cloud measurement approach, curvatures of all three corners can be considered to determine the controlling value. In most cases, the radius of curvature values are similar for both hand measurements and point cloud measurements.

Table 2. Horizontal Displacement Minimum Radii of Curvature Near the Impact Location

Bridge	Girder	Longitudinal interval (cm) [in.]	Point cloud left-corner min. radius of curvature (m)	Point cloud centerline min. radius of curvature (m)	Point cloud right-corner min. radius of curvature (m)	Hand measurement min. radius of curvature (m)
SN 084-0014	18	122 [48]	35.6	34.2	34.3	36.0
SN 084-0077	19	61 [24]	5.9	9.1	11.5	4.1
SN 016-0918	1	7.6 [3]	9.8	8.8	8.7	0.9
SN 041-0067	6	30 [12]	0.9	3.8	3.5	N/A

Table 3. Vertical Displacement Minimum Radii of Curvature Near the Impact Location

Bridge	Girder	Longitudinal interval (cm) [in.]	Point cloud left-corner min. radius of curvature (m)	Point cloud centerline min. radius of curvature (m)	Point cloud right-corner min. radius of curvature (m)	Hand measurement min. radius of curvature (m)
SN 084-0014	18	122 [48]	108.3	847.7	70.5	N/A
SN 084-0077	19	61 [24]	45.8	19.1	7.6	15.2
SN 016-0918	1	7.6 [3]	25.5	42.9	25.0	0.6
SN 041-0067	6	30 [12]	7.9	1.9	1.6	N/A

In this limited case study, the point cloud and hand measurement radius of curvature values are more similar for longer longitudinal intervals. With a smaller 7.6 cm (3 in.) interval for the bridge SN 016-0918 horizontal and vertical measurements, the radii of curvature from hand measurements are one to two orders of magnitude smaller than the radii of curvature from the point cloud measurements. There are a few possible explanations for this discrepancy.

First, it is possible that there was an error in the hand measurements, resulting in a sharper curvature than was physically present. Additionally, for this case, hand measurements were rounded in 3.2 mm (1/8 in.) increments, which may have artificially increased the curvature sharpness. For example, at the point of sharpest curvature in the vertical displacement hand measurement, the recorded displacements (at 7.6 cm [3 in.] intervals) were 18.4 mm, 21.6 mm, 18.4 mm (0.725 in., 0.85 in., 0.725 in.), but the true displacements (without rounding) could have been closer, such as 19.8 mm, 20.3 mm, 19.8 mm (0.78 in., 0.8 in., 0.78 in.), for a considerably shallower curvature. The point cloud measurement procedure avoids this rounding error, potentially capturing curvature more accurately. Computing curvature over a longer interval, such as 12 in., may also be more consistent.

Second, in the point cloud measurement procedure, judgment is required to select appropriate noise-removal parameters. The previous point cloud measurement steps result in a curve with noise—small, frequent fluctuations in displacement. This noise typically does not represent any physical feature and is therefore removed. However, if there were truly some localized features of the damage, they would be unintentionally removed as well, resulting in an overestimated radius of curvature in the point cloud measurements. Overall, there are many nuances to a damaged girder curvature assessment, so future study should consider the implications of these assessments, including their relationship to current repair practices.

CHAPTER 4: FINITE ELEMENT NUMERICAL MODELING

NUMERICAL MODELING APPROACH

Due to the lack of full-scale bridge-vehicle collision experiments and the limitations of drop-weight tests in replicating realistic damage from over-height vehicle strikes, numerical simulations are commonly used to study the behavior of steel girders subjected to vehicular collision. To rigorously simulate damage effects in steel girders due to bridge strikes and evaluate their residual load-carrying capacity, a 3D nonlinear finite element model was developed using Abaqus/CAE (2021). The two-span I-girder was modeled using three plates representing the web and two flanges. Four-node quadrilateral linear shell elements with reduced integration (S4R) were adopted to discretize the model, with a mesh size of 2.54 cm (1 in.) determined from a sensitivity analysis to achieve numerical accuracy with reasonable computational effort. Steel material properties were defined as nonlinear elastic-perfectly plastic behavior—with a modulus of elasticity of 200 GPa (29,000 ksi), a Poisson's ratio of 0.3, and a yield stress of 248 MPa (36 ksi)—representative of older existing bridge girders considered in this study (Wang et al. 2022). Plasticity was defined using the von Mises yield criterion with an associated flow rule.

The models incorporate the supports, using realistic bearing areas, through rigid body constraints with reference points to better represent load distribution. End supports were assigned roller boundary conditions, while the interior support was modeled as pinned, consistent with typical structural plans for stub abutment bridges. Moreover, lateral constraints were applied along the entire centerline of the top flange to prevent lateral displacement, in agreement with observations from site inspections of struck girders restrained by the concrete deck above. Vertical forces were applied uniformly over the full top flange area of the girders, as illustrated in Figure 24.

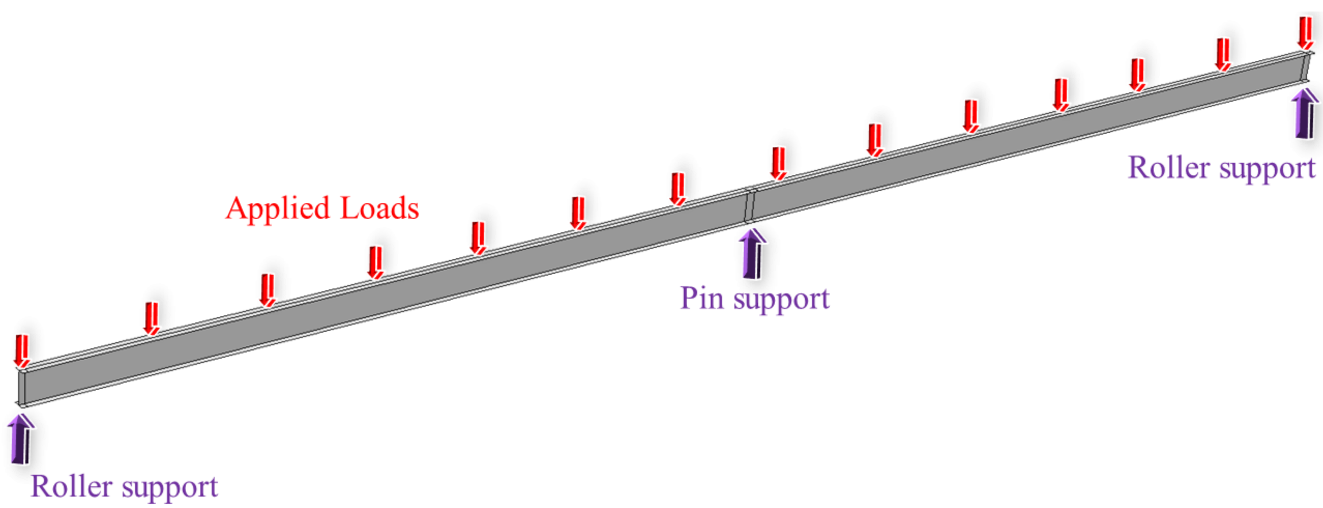

Figure 24. Diagram. Finite element model of two-span steel I-girder with applied forces and boundary conditions.

Load-deflection curves of 18 baseline girders (discussed in Chapter 5) in their undamaged condition, shown in Figure 25, were obtained using the sum of vertical reaction forces at the supports versus midspan deflection (for either of the two equal spans). The curves indicate that the girder dataset captures a broad range of elastic and inelastic characteristics. Load-carrying capacity of a girder is defined by the peak value of total vertical reaction forces, corresponding to the plateau regions of the load-deflection curves.

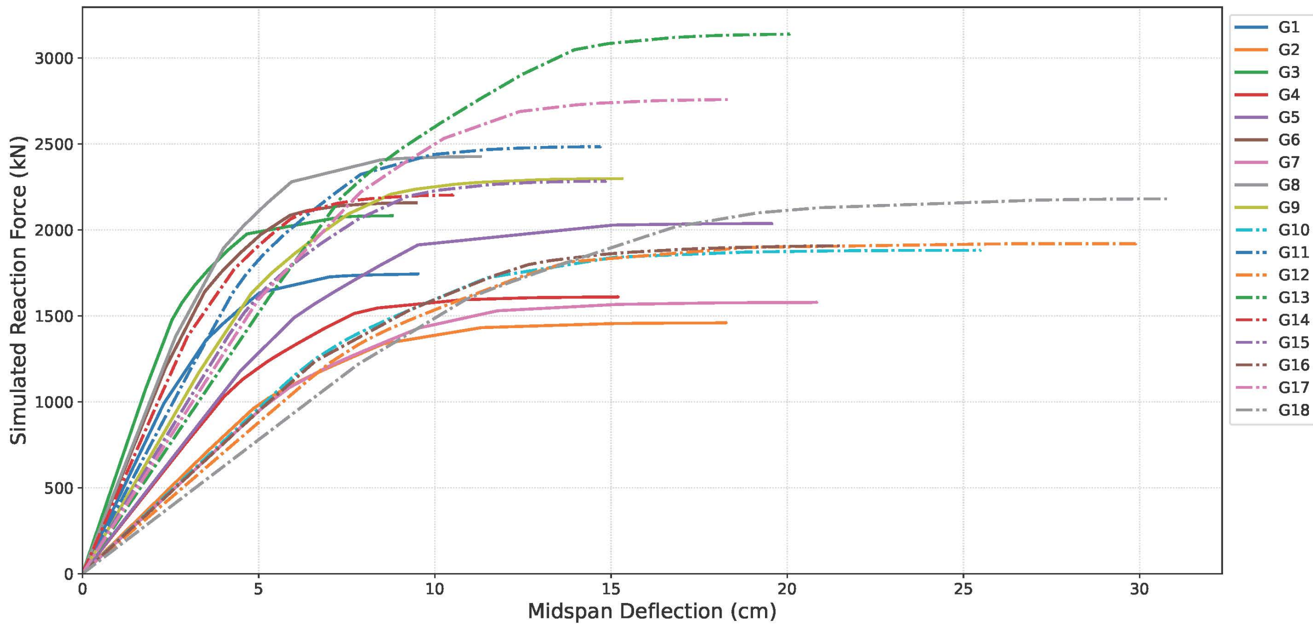

Figure 25. Graph. Load-deflection curves of 18 baseline girders depicting undamaged behavior.

To simulate damage mechanisms observed in real bridge strike incidents, a 30.48 cm (12 in.) long partition was introduced in the girder model at a specified damage location, as shown in Figure 26. Horizontal and vertical displacement-controlled boundary conditions were imposed at the junction of the web and bottom flange of the partition. Finally, two rigid plates (one for each span) were positioned above the top flange to replicate the restraining effect of the overhead concrete deck. The plates were fixed in space by constraining all translational and rotational degrees of freedom, while contact interactions governed the behavior between the plates and the top flange.

The role of the rigid plates is to act as kinematic restraints that limit upward movement of the top flange only during the imposed damage step. If the rigid plates are extended over the interior and end supports, the top flange in these regions would become fully restrained against hogging deformation during the subsequent vertical loading. This over-constraint leads to artificial local compressive stresses in the web and flanges, resulting in unintended local buckling of these elements. To prevent inducing this spurious behavior, each rigid plate was positioned over the clear span and not extended over the interior or end supports, as illustrated in Figure 26.

Contact between the plates and the top flange was defined using hard contact in the normal direction and a tangential friction behavior with a penalty coefficient of 0.9. This modeling approach reduces tangential displacement of the top flange relative to the bridge deck, consistent with field observations.

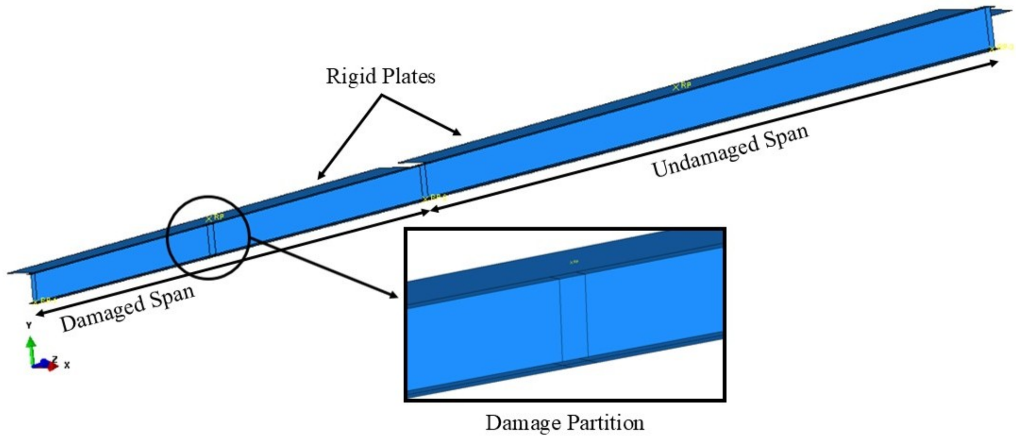

Figure 26. Diagram. Modeling of damaged girder with a damage partition and rigid plates.

DATA EXTRACTION

To reproduce field loading conditions of steel I-girders both before and after a strike, numerical simulations were carried out in four sequential steps using standard (implicit) analysis. First, a uniform load of 34.47 kPa (5 psi) was applied to the top flange as a representative value of the concrete deck weight acting on the girder, based on a typical tributary width, corresponding to the weight of a 20.3 cm (8 in.) thick normal-weight concrete bridge deck, which is typical of most steel bridges considered in this study. Second, prescribed damage displacements (see Chapter 5 for more details) were applied at the partitioned junction of the web and bottom flange to simulate strike-induced deformations.

Third, the imposed displacements were removed, allowing the steel to elastically recover while retaining permanent deformations. The resulting deflected shapes represent those observed in field conditions during actual bridge-strike incidents. Fourth, downward vertical loads were applied incrementally to the top flange until the load-deflection response reached a stable plateau, indicating peak capacity. Because vehicle wheel loads in bridge systems are distributed through the concrete deck and shared among multiple girders, the applied loading was represented as a uniformly distributed load along the top flange. This simplified approach provides a consistent means of assessing the global flexure resistance of the damaged girder and determining its residual capacity independent of a particular vehicle configuration or location. The key output is the ratio of residual (damaged) capacity to undamaged capacity. The resulting capacity ratio can subsequently be used to infer revised girder rating factors for demand effects associated with standard vehicles or other loading scenarios. The residual load-carrying capacity was computed as the sum of reaction forces at the supports at the end of this step. For each simulated girder, the maximum horizontal and vertical displacements (at the end of the third step) and the residual capacity (at the end of the fourth step) were extracted and recorded for subsequent analysis and training of machine learning models.

MODEL VALIDATION

Applicability of the numerical simulations used to generate the dataset of damaged steel I-girders was validated at multiple levels. First, the finite element (FE) girder models were developed following most of the modeling details and assumptions established and validated in the single girder studies by Wang et al. (2022). Second, damage profiles obtained from the FE simulations were compared with displacement measurements from a documented real bridge-strike case. The selected case involves a highway bridge located at the intersection of I-64 and IL-37 near Mt. Vernon, Illinois, identified as IDOT structure number (SN) 041-0067. The bridge consists of two continuous spans for seven composite steel W33x118 girders, with a vertical under-clearance of 4.4 m (14 ft 5 in.). On July 18, 2023, a truck carrying an oversized metal pipe struck six of the seven steel girders near midspan, resulting in severe permanent deformations of interior girders 5 and 6, moderate damage to fascia girder 7, and minor distortions in girders 1, 3, and 4 (as shown earlier in Figure 1).

IDOT inspectors conducted a laser scan of the damaged span, and the point cloud-based method proposed by Schissler et al. (2026b) was used to extract the permanent deformation profile of damaged girder 5. Correspondingly, the permanent damage profiles from the FE analysis of the same girder were obtained at the end of the third simulation step after releasing the imposed displacements, which were selected to reproduce the observed field damage. Horizontal and vertical deflections were referenced relative to the location of maximum displacement for direct comparison. As shown in Figure 27, the numerical model provided a close prediction of the damage profile and magnitude observed in the field. The maximum horizontal deflections obtained from field measurements and FE simulations were 33.9 cm (13.3 in.) and 32.8 cm (12.9 in.), respectively, corresponding to a deviation of 3.2%. Similarly, the maximum vertical deflections were 7.5 cm (2.95 in.) and 7.7 cm (3.03 in.) for the field and FE results, corresponding to a deviation of 2.7%. The slightly narrower horizontal deformation profile observed in the field measurements is attributed to lateral restraint provided by diaphragms. Nonetheless, the numerical model accurately captures the peak deformations and overall deformation pattern observed in the real bridge-strike case. Thus, evaluation of post-strike deformations confirms the accuracy and assumptions of the FE modeling approach and provides validation for the FE-generated dataset in this study.

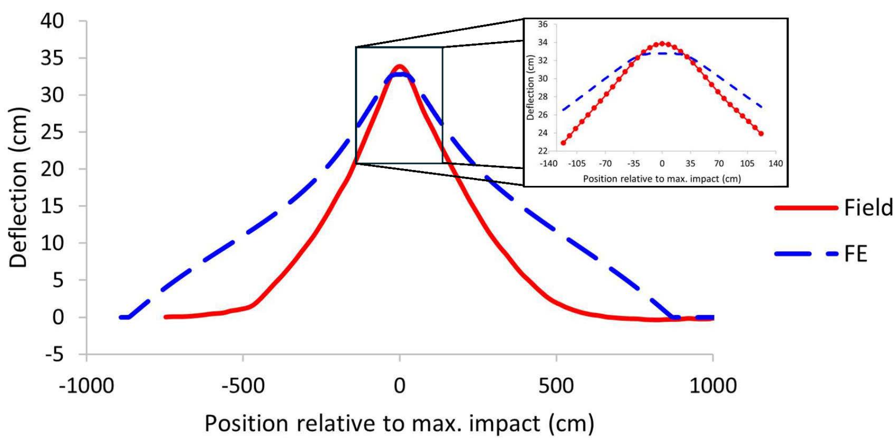

A. Horizontal deflection

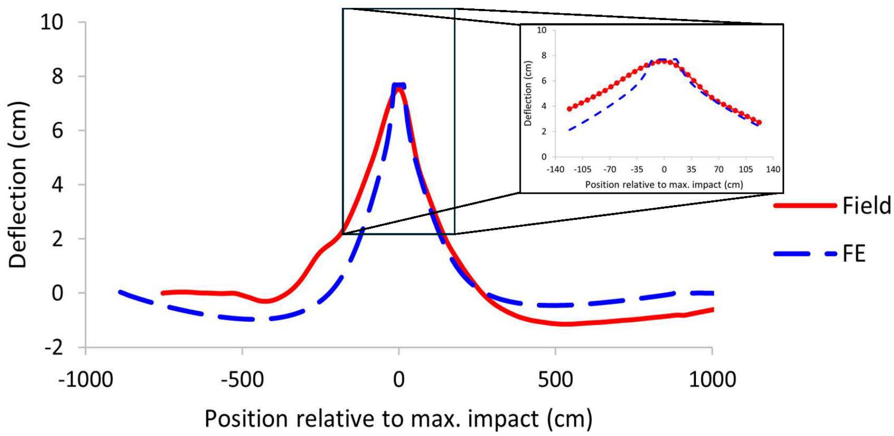

B. Vertical deflection

Figure 27. Graph. Comparison between FE simulation results and field measurements, obtained using the method of Schissler et al. (2026b), for (a) horizontal and (b) vertical permanent deflections of girder 5 in bridge SN 041-0067.

COMPARISON OF TWO-SPAN AND MULTI-SPAN GIRDER RESPONSE

A comparative analysis of two-span and three-span steel I-girders subjected to damage was conducted to investigate the applicability of the developed modeling framework to multi-span bridge configurations. The study considered a W33x118 girder section, with equal two-span lengths of 17.8 m (58.3 ft), and a three-span configuration comprising end spans of 11.8 m (38.8 ft) and an interior span of 17.8 m (58.3 ft), corresponding to a span length ratio of 1 ∶ 1.5 ∶ 1.

The undamaged load-carrying capacities of the two-span and three-span girders are 2282 kN (513 kips) and 3545 kN (797 kips), respectively, reflecting the increased continuity and redundancy of the multi-span system. Consequently, damage in the three-span configuration was applied to the interior span, which represents a critical region where damage can have a significant influence on the girder's load-carrying capacity. Three damage scenarios of varying magnitudes and locations were simulated and compared between the two configurations.

As shown in Table 4, the three-span girder consistently exhibited higher residual capacities and capacity ratios compared to the two-span girder for all damage scenarios considered. This behavior is attributed to the increased continuity provided by additional supports, which enables more effective redistribution of internal forces and reduces the localized effect of the damage. Notably, the difference in capacity ratios, although moderate, consistently indicates improved structural performance of the multi-span system.

These results demonstrate that the developed finite element modeling framework captures the effects of structural continuity and provides conservative estimates when applied to multi-span configurations. Because the analysis includes damage cases at both midspan and locations away from midspan, the comparison captures representative behavior of interior and edge regions of multi-span girders. Accordingly, the findings provide a rational basis for extending the developed framework to bridges with more than two spans. The findings also support the applicability of the machine learning models presented in the following chapter to multi-span girders, while maintaining a conservative prediction of the residual capacity. Future work may expand this analysis to include additional span configurations and explicitly validate these trends using numerical and field data.

Table 4. Comparison of Residual Capacities for Two-Span and Three-Span Girders

Case	Horizontal Damage (cm)	Vertical Damage (cm)	Damage Location Ratio	Two-Span Residual Capacity (kN)	Two-Span Capacity Ratio	Three-Span Residual Capacity (kN)	Three-Span Capacity Ratio
1	17.2	9.1	0.50	1882	0.82	3020	0.85
2	25.3	11.0	0.50	1757	0.77	2922	0.82
3	38.1	19.5	0.75	1922	0.84	3034	0.86

CHAPTER 5: MACHINE LEARNING PREDICTION OF RESIDUAL CAPACITY

DEVELOPMENT OF TRAINING DATASET

The core principle of training machine learning models is to automatically identify and extract patterns from the data to make informed predictions. This is accomplished by collecting a diverse dataset that accurately represents the parameter space of the problem being addressed and that can be used to train and validate machine learning models. For this purpose, data on actual bridge-strike incidents involving steel girders impacted by over-height vehicles in Illinois were obtained from the Illinois Department of Transportation (IDOT) and utilized to develop a comprehensive dataset of simulated damaged steel I-girders using finite element analysis.

Gather Data on Actual Bridge-Strike Incidents

To determine the parameters required to train the machine learning models, numerous steel girder strike events involving over-height vehicles in Illinois were surveyed and documented by the researchers from IDOT inspections and site visits. All relevant data for the damaged girders were collected, including standard wide flange girder sizes (as provided by the American Institute of Steel Construction [AISC, 2017]), span length, steel material, horizontal and vertical damage measurements, and damage location along the span. Table 5 presents the modeled properties of 18 selected girders that serve as the baseline for the damaged girders in the dataset.

Table 5. Modeled Properties of the Girders Forming the Baseline of the Database

Girder #	L (m)	d (cm)	b_f (cm)	t_f (cm)	t_w (cm)	h_w (cm)	r_x (cm)	r_y (cm)	I_x(×10^{-3} m^4)	I_y(×10^{-5} m^4)	Capacity (kN)
G1	11.7	62.5	22.8	1.73	1.12	58.9	25.2	4.88	0.92	3.43	1744
G2	15.8	63.3	22.9	1.96	1.19	59.2	25.7	4.95	1.05	3.93	1459
G3	11.4	69.3	25.4	1.63	1.17	66.3	27.7	5.28	1.23	4.45	2082
G4	15.2	69.3	25.4	1.63	1.17	66.3	27.7	5.28	1.23	4.45	1610
G5	17.3	71.6	25.7	2.36	1.45	67.1	29.0	5.54	1.82	6.66	2037
G6	12.7	70.4	25.4	1.89	1.24	66.6	28.2	5.38	1.43	5.16	2157
G7	17.8	70.4	25.4	1.89	1.24	66.6	28.2	5.38	1.43	5.16	1579
G8	14.0	77.7	26.7	1.93	1.38	73.7	30.7	5.46	1.94	6.12	2429
G9	16.5	78.5	26.7	2.16	1.44	74.2	31.2	5.56	2.16	6.83	2300
G10	20.3	78.5	26.7	2.16	1.44	74.2	31.2	5.56	2.16	6.83	1882
G11	16.5	79.0	26.7	2.36	1.49	74.4	31.8	5.64	2.36	7.49	2482
G12	21.5	79.0	26.7	2.36	1.49	74.4	31.8	5.64	2.36	7.49	1922
G13	21.6	81.0	38.1	3.02	1.80	74.9	33.5	8.74	4.14	27.9	3118
G14	14.0	77.2	26.7	1.70	1.32	73.7	30.5	5.36	1.73	5.41	2202
G15	17.8	85.3	29.2	1.88	1.40	81.5	33.8	5.92	2.55	7.83	2282
G16	21.6	85.3	29.2	1.88	1.40	81.5	33.8	5.92	2.55	7.83	1908
G17	20.3	87.9	29.5	2.69	1.61	82.3	35.3	6.27	3.62	11.5	2758
G18	26.7	93.5	30.5	2.39	1.59	88.9	37.1	6.27	3.95	11.3	2180

Survey results indicated that most strike incidents occurred in low-clearance older bridges susceptible to over-height vehicle collisions. These bridges were found to have steel I-girders fabricated predominantly from A36 steel (Wang et al. 2022) and designed with specific bearing configurations, where end supports consisted of expansion (roller) bearings and interior supports consisted of rocker (pinned) bearings. Accordingly, these parameters were kept constant in the finite element simulations and were not considered as varying input features. Within the surveyed structures, bridge-strike incidents exhibited similar damage mechanisms characterized by lateral (horizontal) and vertical deflections of the girder web and bottom flange, while the top flange remained restrained by the overhead concrete deck. Consequently, field damage measurements obtained from IDOT were used to guide the generation of damage magnitudes in the dataset.

Latin hypercube sampling (LHS) (McKay et al. 2000) is a semi-random sampling approach used to generate damage magnitudes from field measurements. LHS ensures that each sample lies within a unique axis-aligned hyperplane, thereby capturing extreme damage magnitudes that are less frequent but can significantly influence the load-carrying capacity of steel girders. Furthermore, different strike locations along the span were considered. Since most strikes occur near girder midspan (over traffic lanes), while they are less frequent near the bearing supports (at the abutments and piers), each baseline girder is associated with six damage cases at midspan denoted by $DLR = 0.50$, two damage cases at the first quarter of the span (near the end support) denoted by $DLR = 0.25$, two damage cases at the third quarter of the span denoted by $DLR = 0.75$, and two damage cases closer to the interior support denoted by $DLR = 0.85$, where DLR represents the ratio of damage location to the total length of the damaged span (from an end support of the continuous two-span girder), as shown in Figure 28.

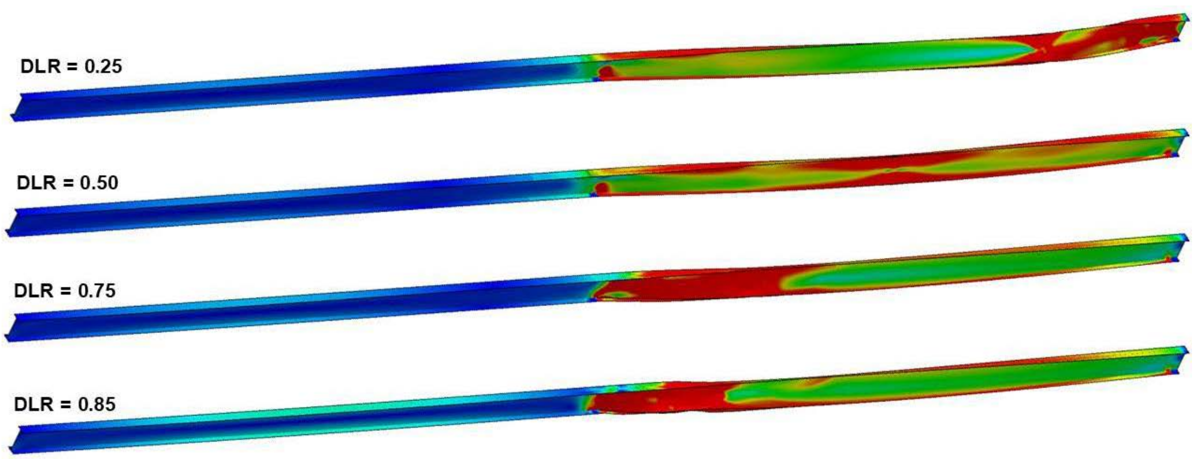

Figure 28. Illustration. Examples from the dataset of strike locations at quarter of span, midspan, three-quarters of span, and near the pier.

In this step, a representative girder dataset of 216 samples was developed by randomly assigning sampled damage magnitudes from LHS and damage locations to the 18 baseline girders. A sample of damaged girder cross-sections illustrating the diversity in damage magnitudes and deformation patterns represented in the dataset is shown in Figure 29. Using this constructed dataset to train the machine learning models resulted in a prediction accuracy of 96.79% on the unseen test set, as demonstrated in the validation section of the methodology. Furthermore, applicability of the finite element modeling framework to multi-span girders was presented in Chapter 4, which demonstrated that two-span finite element simulations produce conservative residual capacity estimates when extended to multi-span configurations.

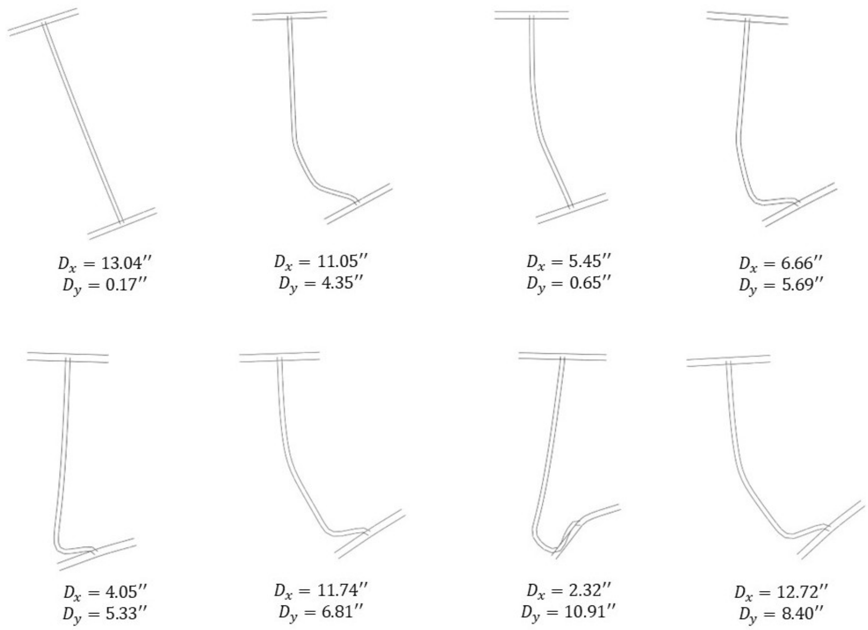

Figure 29. Illustration. Sample of damaged steel girder cross-sections from the constructed dataset.

Data Analysis and Preprocessing

In this step, the raw data collected from the previous step were analyzed and preprocessed, which is essential for effectively training machine learning models. The objectives of this step are to (1) identify girder variables most relevant to the residual capacity; (2) analyze and visualize the data to obtain meaningful insights; and (3) divide the dataset into training and test sets for developing and validating machine learning models.

First, variables from the developed FE models that influence the estimation of residual capacity were identified to construct the dataset. These variables form the input features for the machine learning models and are selected based on prior related studies (Hosseinpour et al. 2020; Liu et al. 2023; Liu et al. 2025) and quantities readily available from bridge structural plans and post-impact inspection reports (IDOT 2024; Shanafelt and Horn 1984). Other factors, such as material nonlinearity, damage-induced stresses, and damaged girder deformations, are inherently represented in the numerical modeling of damaged girders and are therefore embedded in the FE computation of residual capacity. Table 6 summarizes 13 selected features based on geometric properties of the steel I-girders and characteristics of the observed damage. The observed horizontal deflection D_x and vertical deflection D_y represent the maximum values recorded after the elastic recovery step of the FE simulation. The damage location ratio DLR consists of four numeric values (0.25, 0.50, 0.75, 0.85), indicating the strike location as a fraction of the span length. The output variable in the dataset is the residual load-carrying capacity C_R.

Table 6. Description of the Input and Output Parameters

Variables	Parameters	Symbols
Inputs	Span length (cm)	L
	Girder depth (cm)	d
	Flange width (cm)	b_f
	Flange thickness (cm)	t_f
	Web thickness (cm)	t_w
	Web height (cm)	h_w
	Radius of gyration about *x*-axis (cm)	r_x
	Radius of gyration about *y*-axis (cm)	r_y
	Moment of inertia about *x*-axis (cm^4)	I_x
	Moment of inertia about *y*-axis (cm^4)	I_y
	Observed horizontal deflection (cm)	D_x
	Observed vertical deflection (cm)	D_y
	Damage location ratio (—)	DLR
Output	Residual load-carrying capacity (kN)	C_R

Second, exploratory data analysis was conducted to examine the underlying distributions and relationships of the input and output variables. Data were imported and analyzed in Python (Van Rossum and Drake 1995) using `pandas` (McKinney 2010) and `seaborn` (Waskom 2021) libraries, selected for their strong capabilities in data science and visualization. Statistical properties of the dataset, presented in Table 7, indicate a wide range of values for each parameter.

Table 7. Statistical Summary of Database

Parameter	Minimum	Maximum	Mean
L (cm)	1143	2667	1737
d (cm)	62.43	93.57	76.64
b_f (cm)	22.83	38.10	27.19
t_f (cm)	1.63	3.02	2.09
t_w (cm)	1.12	1.80	1.39
h_w (cm)	58.98	88.80	72.46
r_x (cm)	25.17	37.13	30.66
r_y (cm)	4.88	8.74	5.72
I_x (×10^{-3} cm^4)	91.75	413.4	214.5
I_y (×10^{-3} cm^4)	3.43	27.88	7.76
D_x (cm)	−0.18	50.27	20.06
D_y (cm)	−2.49	27.70	10.78
DLR (—)	0.25	0.85	0.56
C_R (kN)	907	2950	1689
C_R/C	0.519	0.995	0.798

Negative values for deflection indicate a girder that experienced a final displacement opposite to the direction of the strike. The residual load-carrying capacity (C_R) ranges from 907 kN (203.8 kips) to 2,950 kN (663 kips), with an average of 1,689 kN (379.6 kips). In addition, a residual capacity ratio (C_R/C) was computed by normalizing the residual capacity of each damaged girder by its corresponding undamaged capacity listed in Table 5. The residual capacity ratio in the database ranges from 0.519 to 0.995, with a mean of 0.798, reflecting the relative reduction in I-girder capacity due to bridge strike damage.

To visualize the statistical distribution of each parameter in the dataset and gain a clearer understanding of the data, histograms of the input and output variables are shown in Figure 30. The histogram of damage location ratio (DLR) indicates that most damage cases occur at midspan, while the remaining locations are uniformly represented.

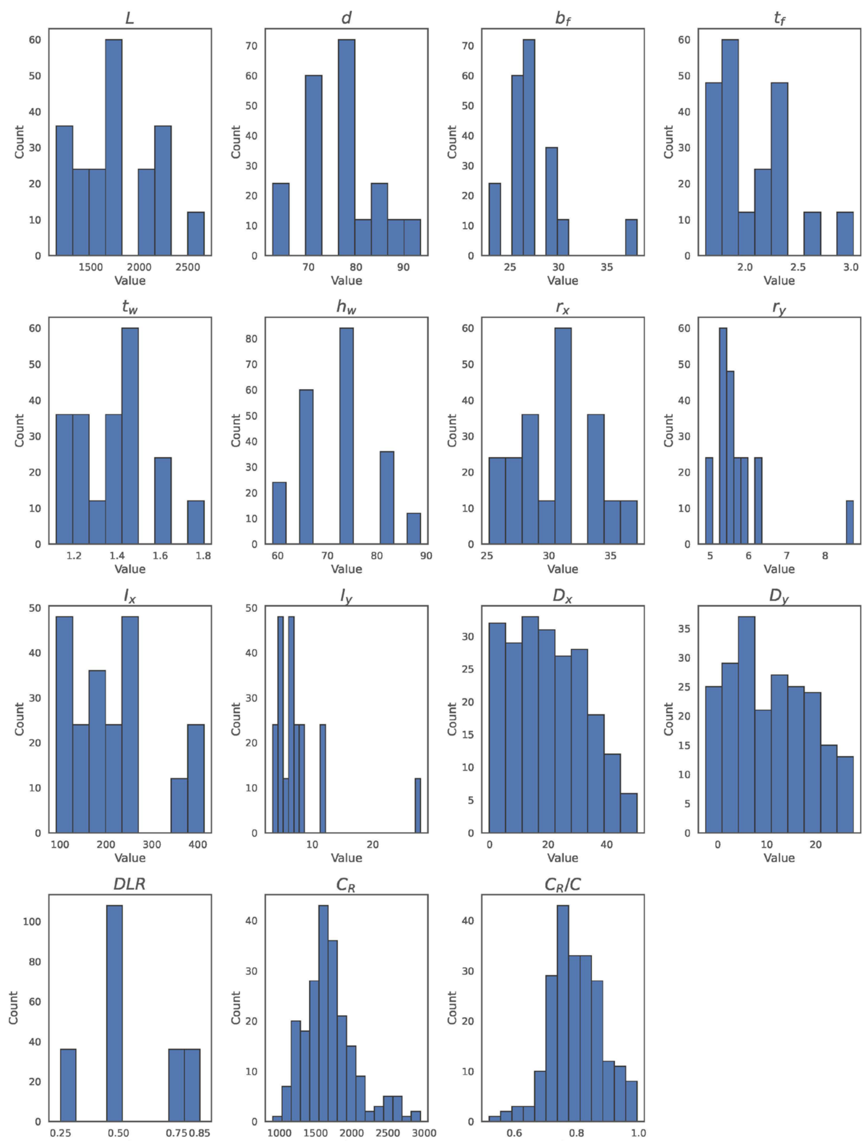

Figure 30. Graph. Distribution of dataset parameters.

Linear regression relationships were fitted between the residual capacity (C_R) and each input variable, as shown in Figure 31. Residual capacity generally increases with increasing geometric cross-sectional properties of the girders and slightly decreases with increasing damage deflections. Since the damage location ratio is represented by four discrete values, capacity values for each ratio were averaged for clearer visualization. As expected, strikes at midspan ($DLR = 0.50$) result in lower residual capacities compared to the other three locations.

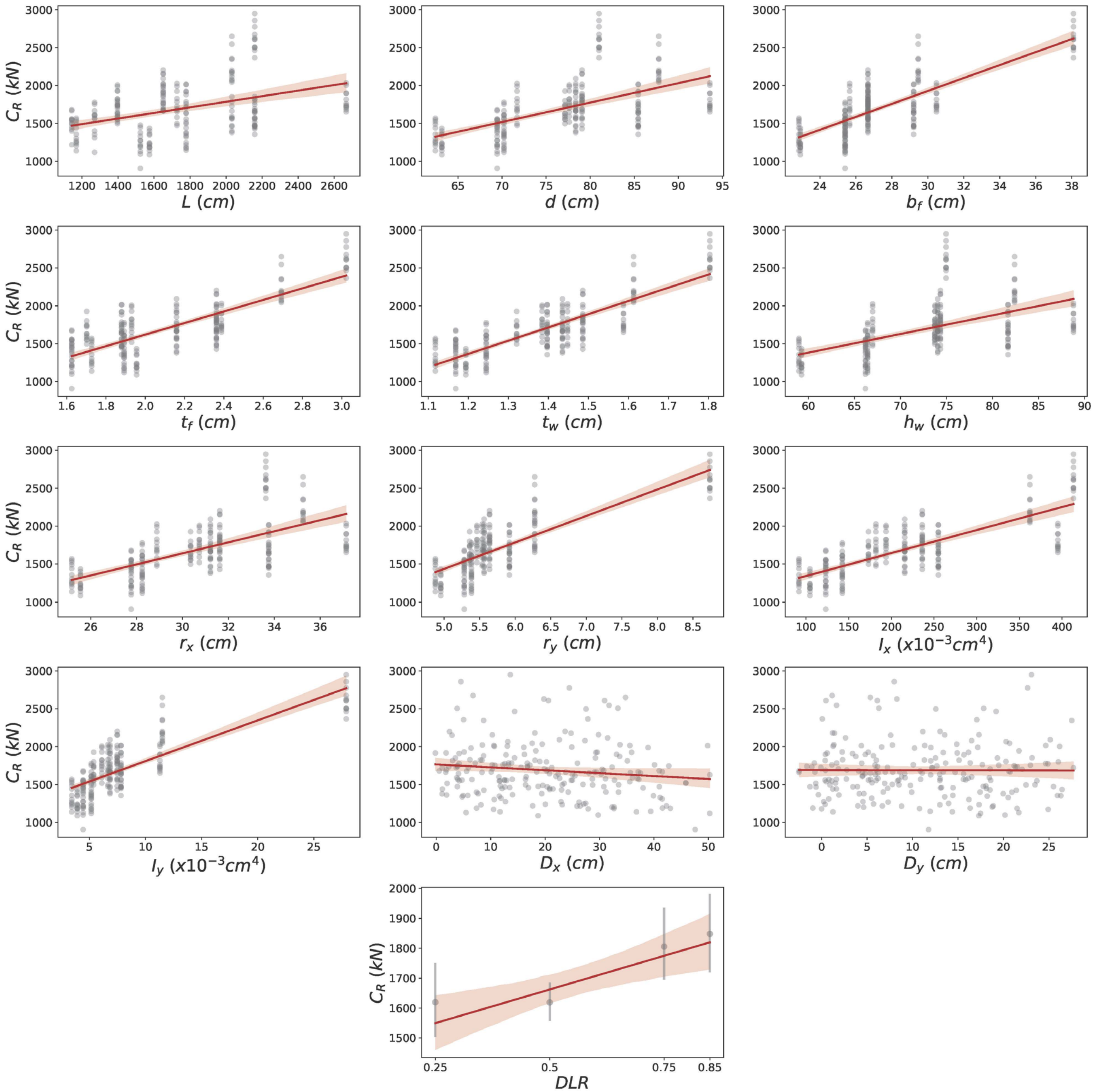

Figure 31. Graph. Regression graphs of dataset parameters.

Third, data preprocessing involved randomly splitting the dataset of 216 samples into an 80% training set and a 20% test set. The training set consisted of 172 samples, while the test set included 44 samples. In later stages of the machine learning methodology, the training set was used to develop the models, whereas the test set was utilized to evaluate their performance and assess generalizability.

Subsequently, all raw input variables were scaled to the range [0, 1] using the min-max normalization technique (Pedregosa et al. 2011), as defined in Figure 32, where x is the original value, x_{min} and x_{max} represent the minimum and maximum values of the feature, respectively, and x_{norm} is the normalized value. The normalization parameters were determined from the training set and then applied to both the training and test sets to prevent data leakage. This scaling ensures that all features contribute equally to the models and avoids a situation where those with larger magnitudes could dominate the training process.

$$x_{norm} = \frac{x - x_{min}}{x_{max} - x_{min}}$$

Figure 32. Equation. Min-max normalization for scaling dataset input variables.

MACHINE LEARNING MODELS

Five machine learning algorithms commonly implemented in similar studies (Almustafa and Nehdi 2022; Dissanayake et al. 2022) were selected: (1) Multi-layer Perceptron Neural Networks (MLP), (2) Ridge Regression (RR), (3) K-Nearest Neighbors (KNN), (4) eXtreme Gradient Boosting (XGBoost) (Chen and Guestrin 2016), and (5) Gaussian Process Regression (GPR) (Williams and Rasmussen 2006).

The first model was developed using the MLP algorithm consisting of an input layer, hidden layers, and an output layer for prediction. This network was inspired by biological operations of neural networks in the human brain and learns patterns in data through gradient descent and backpropagation (Rosenblatt 1962; Rumelhart et al. 1985). The developed architecture includes 13 input neurons representing the input variables of the dataset, two hidden layers with 128 and 64 neurons, respectively, and a single output neuron for predicting the residual capacity, as illustrated schematically in Figure 33. A rectified linear unit (ReLU) activation function was used to introduce nonlinearity into the model, and the optimization process was carried out using the Adam optimizer trained for 10,000 epochs.

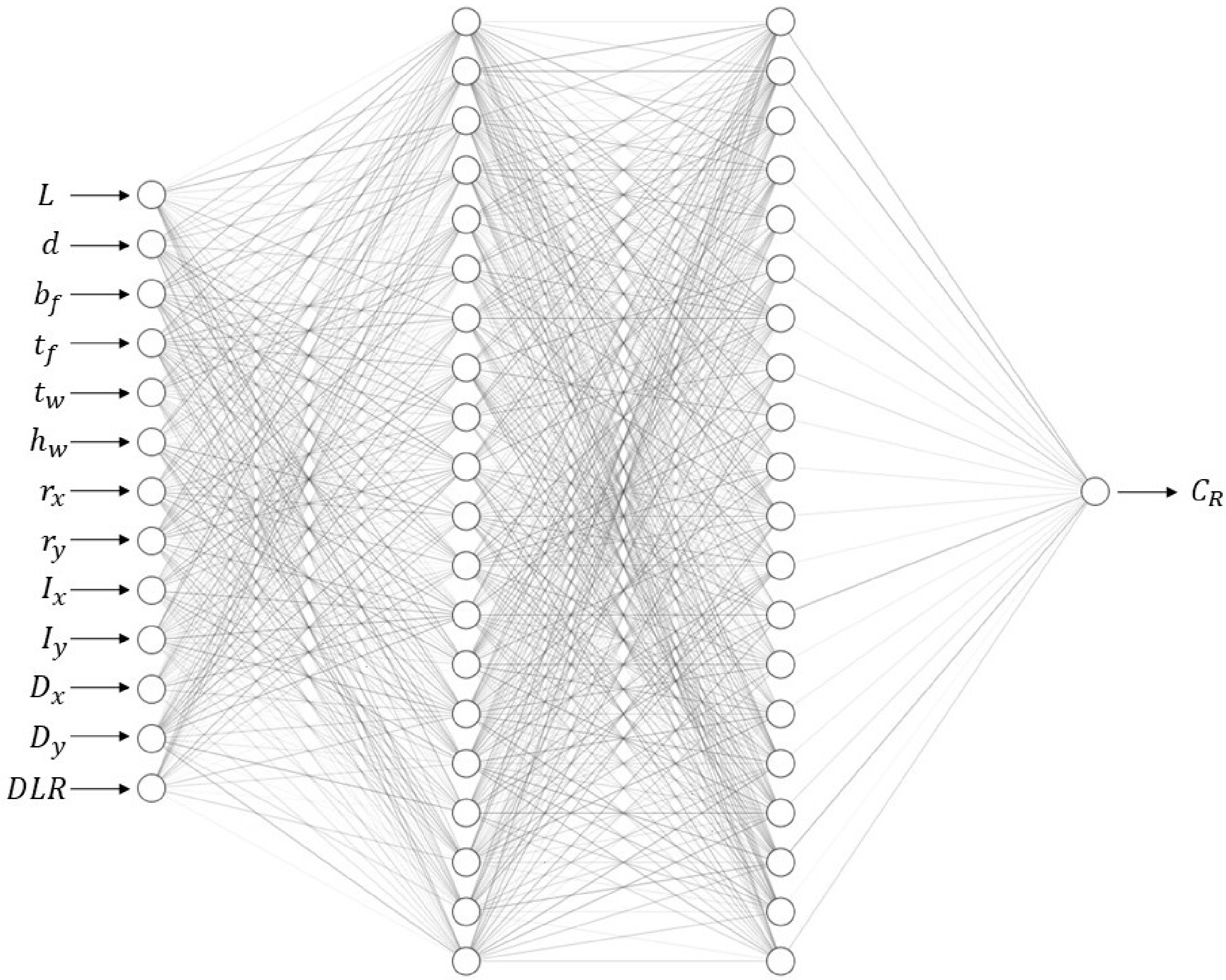

Figure 33. Illustration. Graphical representation of the architecture of a multi-layer perceptron neural network model.

The second model used RR, a variant of linear regression that minimizes an objective function composed of a linear least squares loss and an l_2-norm regularization term, as shown in Figure 34, where $L(\boldsymbol{w})$ is the loss function to be minimized; y_i is the target variable of the i^{th} sample; $\boldsymbol{x}_i$ is the feature vector of the i^{th} sample; $\boldsymbol{w}$ is the vector of learnable weights; $||\boldsymbol{w}||_2^2$ is the squared l_2-norm of the weight vector; and λ is the regularization parameter (set to 1.0 in this study). This formulation penalizes large regression coefficients through the l_2-norm of the model weights scaled by the regularization parameter λ to reduce overfitting.

$$L(\boldsymbol{w}) = \sum_{i=1}^{n} (y_i - \boldsymbol{w}^T \boldsymbol{x}_i)^2 + \lambda ||\boldsymbol{w}||_2^2$$

Figure 34. Equation. Ridge regression loss function.

The third model was developed using KNN, a nonparametric supervised learning method that predicts an output value by averaging the target values of the K^{th} closest training examples. In the developed KNN model, the predicted value is calculated as the average of the three nearest neighbors ($K = 3$) based on their Euclidean distances, as defined in Figure 35, where $d(\boldsymbol{x}, \boldsymbol{x}')$ is the Euclidean distance between feature vectors $\boldsymbol{x}$ and $\boldsymbol{x}'$, and n is the number of features. The Euclidean distance defines the closeness between input vectors in the feature space and is used to identify the K-Nearest Neighbors.

$$d(\boldsymbol{x}, \boldsymbol{x}') = \sqrt{\sum_{i=1}^{n} (x_i - {x_i}')^2}$$

Figure 35. Equation. Euclidean distance used in KNN algorithm.

The fourth model employed the XGBoost algorithm, an ensemble learning technique that trains a sequence of weak decision trees using a boosting approach. The algorithm minimizes the loss function of each decision tree through gradient descent and combines their predictions to produce a strong predictor with improved performance and generalizability. The model hyperparameters, including regularization factors, were tuned to reduce overfitting using grid search with *K*-fold cross-validation, as presented later in this report.

The optimized XGBoost model consisted of 600 decision trees (*n_estimators* = 600) with a learning rate of 0.03, a maximum tree depth of four (*max_depth* = 4), a minimum child weight of four (*min_child_weight* = 4), subsampling of 70% of the observations and features for each tree (*subsample* = 0.7, *colsample_bytree* = 0.7), an L_2 regularization parameter of 2 (*reg_lambda* = 2), and a split regularization term (*gamma* = 0.2) to further control model complexity and reduce overfitting.

The fifth model was developed using GPR, a nonparametric Bayesian regression algorithm that treats the underlying function mapping input features to the output as a realization from a Gaussian process defined by a mean function and a kernel function. The trained GPR model utilized a joint kernel comprising a Rational Quadratic kernel that captures smooth nonlinear relationships between the input features and the output, combined with a white noise kernel that represents observation noise and provides regularization.

The joint kernel is defined in Figure 36, where $\|\boldsymbol{x}_i - \boldsymbol{x}_j\|$ denotes the Euclidean distance between input vectors $\boldsymbol{x}_i$ and $\boldsymbol{x}_j$ in the feature space; α is the parameter controlling the kernel shape, with an initial value of 1.0; l is the characteristic length scale, also initialized to 1.0; σ_n^2 is the variance of the white noise term that governs the magnitude of the observation noise, initialized to 0.01; and δ_{ij} is the Kronecker delta, which adds the noise term to the diagonal entries of the covariance matrix. All hyperparameters, including α, l, and σ_n^2, were determined by maximizing the log marginal likelihood.

$$k(\boldsymbol{x}_i, \boldsymbol{x}_j) = \left[1 + \frac{\left\|\boldsymbol{x}_i - \boldsymbol{x}_j\right\|^2}{2\alpha l^2}\right]^{-\alpha} + \sigma_n^2 \delta_{ij}$$

Figure 36. Equation. Joint kernel function composed of Rational Quadratic and white noise kernels used in GPR algorithm.

MODEL TRAINING AND VALIDATION

The primary objective of this step is to develop and validate the performance of machine learning models capable of accurately and efficiently predicting the residual load-carrying capacity of damaged steel I-girders. All models were trained and tested in Python (Van Rossum and Drake 1995), using the `XGBoost` library (Chen and Guestrin 2016) for the XGBoost model and the `scikit-learn` library (Pedregosa et al. 2011) for the remaining four models.

Figure 37 presents a comparison of training results between the target residual capacities from FE analysis and the predicted capacities from the XGBoost model. (See Ibrahim et al. [2026] for results on training performance of remaining models.) Such comparisons indicate that the trained models demonstrated strong training performance, closely matching the target values. Notably, predictions from the XGBoost and GPR models showed particularly close agreement with the target values, while the remaining models exhibited slight deviations.

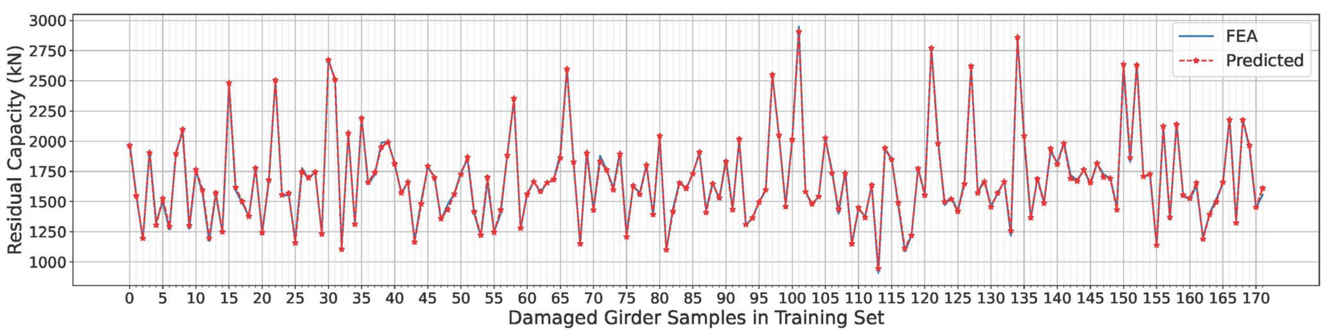

Figure 37. Graph. Comparison of target and predicted samples for the training set using the XGBoost model.

To quantitatively evaluate and compare the performance of the developed machine learning models, five evaluation metrics were used: mean absolute percentage error (MAPE), mean absolute error (MAE), mean squared error (MSE), root mean squared error (RMSE), and the coefficient of determination (R^2). These statistical measures are defined in Figure 38, where n is the total number of samples in the training set; y_i is the target value of the i^{th} observation; $\hat{y}_i$ is the predicted value of the i^{th} observation; and $\bar{y}$ is the mean of all target values. According to Lewis (1982), MAPE scores less than 10% are considered highly accurate, while scores between 10% and 20% indicate good predictions; values from 20% to 50% suggest reasonable accuracy, and those exceeding 50% are regarded as inaccurate.

$$MAPE = \frac{1}{n}\sum_{i=1}^{n}\left|\frac{y_i - \widehat{y_i}}{y_i}\right| \times 100\%$$

A. Mean Absolute Percentage Error

$$MAE = \frac{1}{n}\sum_{i=1}^{n}|y_i - \hat{y}_i|$$

B. Mean Absolute Error

$$MSE = \frac{1}{n}\sum_{i=1}^{n}(y_i - \widehat{y_i})^2$$

C. Mean Squared Error

$$RMSE = \sqrt{\frac{1}{n}\sum_{i=1}^{n}(y_i - \widehat{y_i})^2}$$

D. Root Mean Squared Error

$$R^2 = 1 - \frac{\sum_{i=1}^{n}(y_i - \widehat{y_i})^2}{\sum_{i=1}^{n}(y_i - \overline{y_i})^2}$$

E. Coefficient of Determination

Figure 38. Equation. Five evaluation metrics used to quantify the performance of the developed machine learning models.

Table 8 summarizes the evaluation metrics for the developed models. Training results show that the XGBoost and GPR models achieved the highest accuracies, with MAPE scores of 0.85% and 0.80%, respectively. To validate the generalizability of all models to unseen data, the five models were subsequently evaluated on the test set. Figure 39 displays the predictions of 44 test samples by the trained XGBoost model, showing excellent agreement with the target values. (See Ibrahim et al. [2026] for additional results on test performance.) Among the models, XGBoost and GPR exhibit the strongest performance on the test set, while RR and KNN provide the lowest performance, as indicated by the metric scores in Table 8 (best test metrics are shown with an asterisk). GPR achieved a slightly lower MAPE of 2.60% and MAE of 45.48 kN (10.22 kips), whereas XGBoost yielded significantly lower MSE and RMSE scores of 4799 kN^2 (242.6 $kips^2$) and 69.28 kN (15.57 kips), respectively. This distinction arises because MAPE and MAE measure average absolute errors, while MSE and RMSE assign greater penalties to larger errors. On the other hand, the KNN and RR models showed higher errors, with MAPE values of 5.16% and 5.40% and MAE values of 88.66 kN (19.93 kips) and 89.43 kN (20.10 kips), respectively.

Table 8. Evaluation Metrics of the Five Machine Learning Models (Best Test Metrics Shown with an Asterisk)

Model	Dataset	MAPE	MAE (kN)	MSE (kN^2)	RMSE (kN)	R^2
Multi-layer Perceptron (MLP)	Training	2.72%	44.53	4207	64.86	97.00%
	Test	3.93%	66.06	6988	83.59	93.35%
Ride Regression (RR)	Training	5.71%	92.01	12930	113.7	90.78%
	Test	5.40%	89.43	12137	110.2	88.46%
K-Nearest Neighbors (KNN)	Training	4.36%	68.87	8235	90.75	94.13%
	Test	5.16%	88.66	12988	114.0	87.65%
eXtreme Gradient Boosting (XGBoost)	Training	0.85%	13.46	302.0	17.39	99.78%
	Test	3.21%	52.90	4799*	69.28*	95.44%*
Gaussian Process Regression (GPR)	Training	0.80%	12.70	347.0	18.64	99.75%
	Test	2.60%*	45.48*	5882	76.69	94.41%

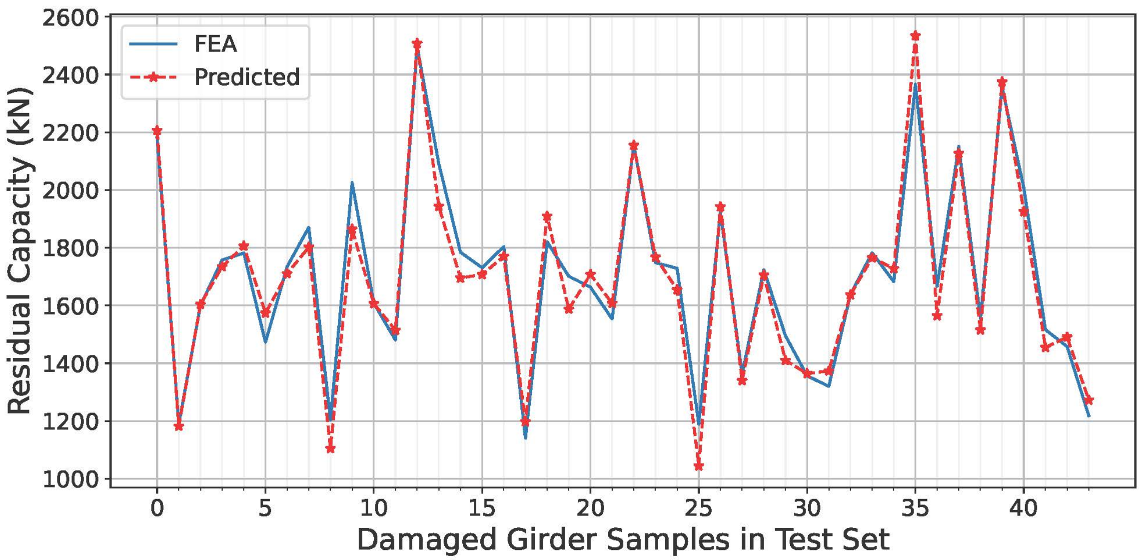

Figure 39. Graph. Comparison of target and predicted samples for the test set using the XGBoost model.

Figure 40 presents the prediction regression graph of the developed XGBoost model for the test set, showing predicted versus target values of the residual load-carrying capacity. The dashed diagonal line represents ideal predictions that perfectly match the targets, while the solid fitting line represents the best fit linear regression between the predicted and target values. The fitting line of the XGBoost model is closely aligned with the equal line, achieving a coefficient of determination (R^2) of 0.95 (which exceeds the other four models). (Additional results are discussed in Ibrahim et al. [2026].) Figure 41 illustrates the residuals of the XGBoost model's predicted values in the test set. While the other models exhibit samples with relatively large residuals, XGBoost predictions are limited within $\pm$200 kN ($\pm$45 kips) from the target values.

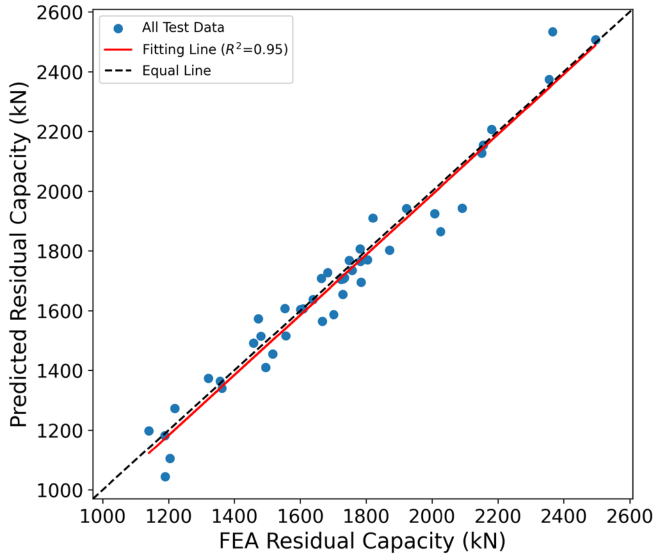

Figure 40. Graph. Prediction regression graphs for the test set using the XGBoost model.

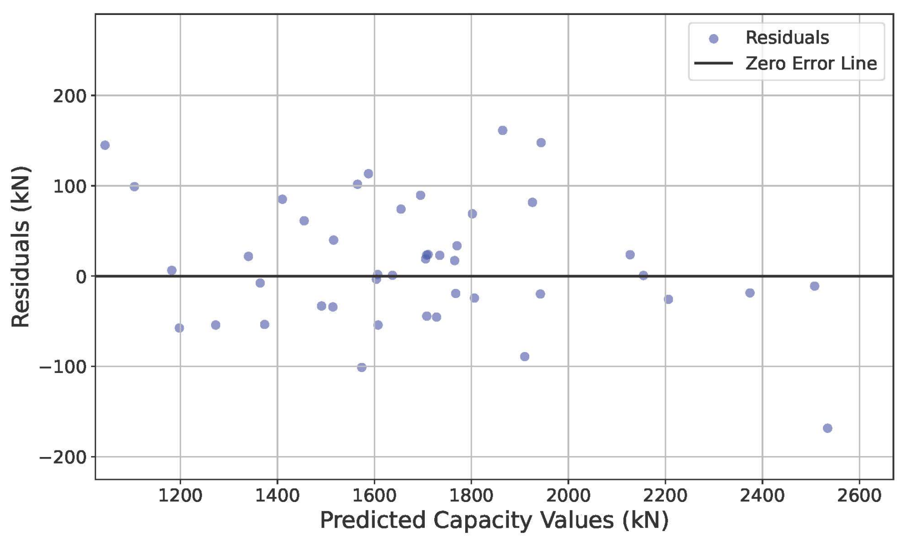

Figure 41. Graph. Residual plots of the test set for the XGBoost model.

Thus, the developed XGBoost model demonstrates excellent learning and prediction capabilities and shows superior performance for estimating the load-carrying capacity of damaged steel I-girders. Therefore, it can be considered the most suitable candidate model for further interpretation and explanation in the final step of the methodology.

Additionally, *K*-fold cross-validation was conducted to evaluate the ability of all models to generalize to unseen data. *K*-fold cross-validation partitions the training set into *K* subsets, trains the model on *K*-1 subsets, and validates its performance on the remaining subset. Given the total training set size of 172 samples, *K* was set to 5 to provide sufficiently large validation subsets that increase the variance of the performance estimate and help expose potential overfitting, while maintaining enough training data in each iteration.

The training set was divided randomly into five folds. In each cross-validation iteration, four folds were used to train the model, while the remaining fold was used for validation. This process was repeated five times, ensuring each fold served once as the validation set. Figure 42 presents cross-validation results for the XGBoost model across the five iterations using the mean absolute error and coefficient of determination metrics. The box-and-whisker plots summarize the distribution of the metric values across the five folds, showing the median score, interquartile range, and the minimum and maximum values obtained for each metric.

XGBoost five-fold cross-validation results demonstrated robust and stable generalization capability across all iterations, with a mean MAPE score of 4.45% and a standard deviation of 0.69%, confirming its ability and consistency to generalize effectively to unseen data. These findings highlight the high predictive accuracy of the developed models, particularly XGBoost, which achieved an accuracy of 96.79% on the test set in predicting the residual load-carrying capacity of damaged steel I-girders.

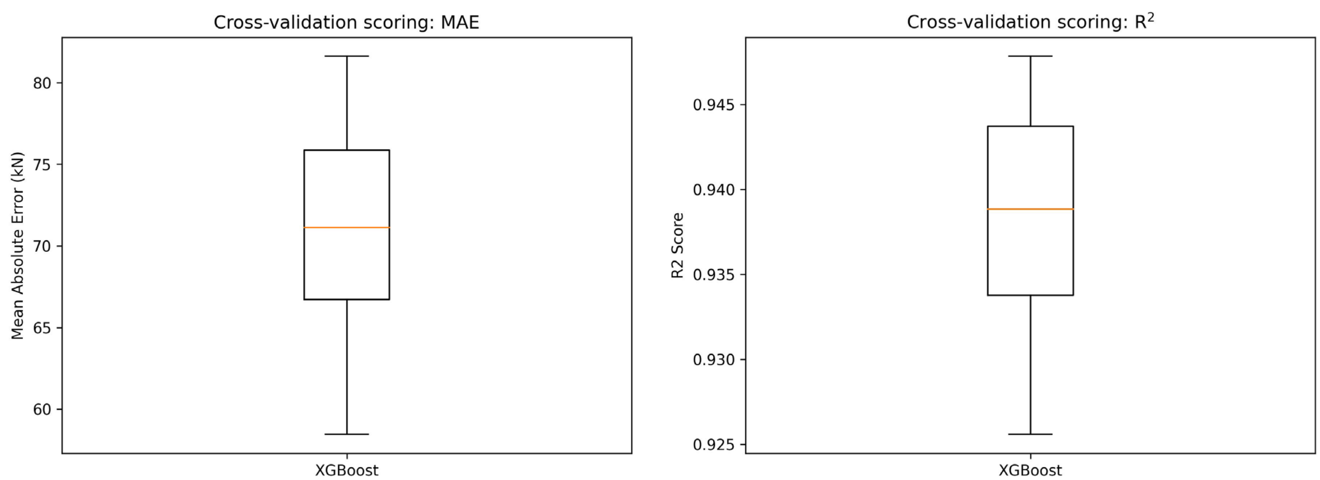

Figure 42. Chart. *K*-fold cross-validation results for the XGBoost model.

PREDICTION EXPLAINABILITY

The final stage of the machine learning methodology is model interpretation, employing explainable artificial intelligence (XAI) techniques to understand and explain why and how a machine learning model produces predictions. Most machine learning models are inherently complex and do not provide explanations into their decision-making processes, thereby functioning as "black-box" models (Hassija et al. 2024). Therefore, it is essential to develop models that not only predict outputs accurately, but also provide transparent and interpretable explanations for their predictions to increase confidence in their performance.

XGBoost Feature Importance

The tree architecture of the developed XGBoost model makes it more intrinsically interpretable than other machine learning models, such as deep neural networks (Hassija et al. 2024). Feature importance scores of input variables were automatically extracted from the trained XGBoost model. Figure 43 shows the weight score of each input variable, indicating its influence on the model's predictions. The weight score is computed based on the number of times a given variable is used to split the data across all trees in the ensemble model (Chen and Guestrin 2016). The scores indicate that the five most important input variables in predicting the residual capacity of damaged steel girders are observed horizontal damage deflection (D_x), observed vertical damage deflection (D_y), span length (L), damage location ratio (DLR), and girder depth (d).

However, weight scores in trees do not account for the quality of the splits and may be inconsistent with other feature importance approaches, such as the gain and cover scores (Lundberg et al. 2018). Consequently, the SHapley Additive exPlanations (SHAP) (Lundberg and Lee 2017) and Local Interpretable Model-Agnostic Explanations (LIME) (Ribeiro et al. 2016) frameworks were further employed to evaluate the influence of each input variable on the predictions of the trained XGBoost model, providing consistent and locally accurate methods for feature attribution in tree ensembles.

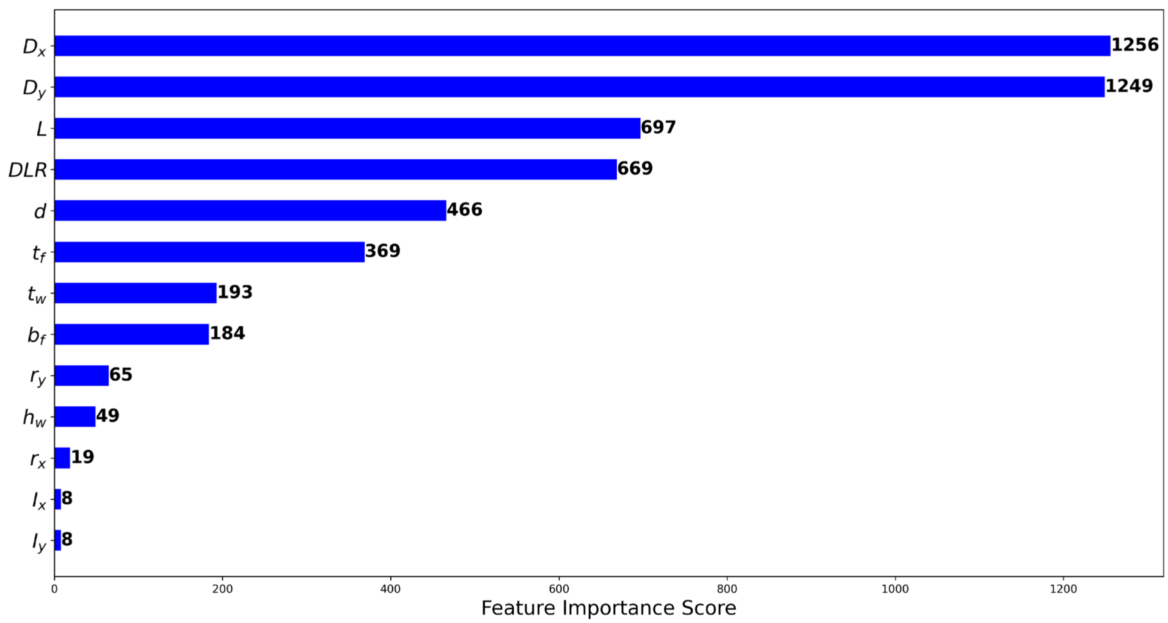

Figure 43. Chart. Feature importance of dataset inputs based on XGBoost model weights.

SHAP Explainability Framework

SHAP is a model-agnostic framework that provides enhanced interpretability and local explainability of individual predictions for machine learning models. The SHAP algorithm is widely used for its fast implementation for tree-based models (Molnar 2025), making it well-suited for explaining the performance of the developed XGBoost model. The SHAP framework is based on Shapley values, which are derived from cooperative game theory to compute the contribution of each feature to the model's prediction.

In Shapley game theory, each feature is treated as a player in a game, while the model's prediction represents the total payoff or gain that is fairly distributed among the players based on the relative importance of their contributions to the outcome of the game (Shapley 1953). A SHAP explanation model is an additive feature attribution method that uses a linear surrogate model g to explain the complexity of a machine learning model prediction based on the sum of feature contributions and the base value, as shown in Figure 44, where ϕ_i is the SHAP value for the i^{th} feature; $z_i' \in \{0,1\}$ is a binary indicator for whether feature i is present (1) or absent (0); ϕ_0 is the base value representing the model's expected value across all training data; and M is the total number of input features. The additive surrogate model decomposes a prediction into a baseline value and feature contributions, thereby quantifying and interpreting the influence of each input feature on the prediction.

$$g(z^{'}) = \phi_0 + \sum_{i=1}^{M} \phi_i z_i{}'$$

Figure 44. Equation. Linear surrogate model equation composed of sum of feature contributions.

The SHAP value ϕ_i of the i^{th} feature is computed by Figure 45, where F is the set of all input features; S is a subset of F that does not include feature i; and $f_S(x_S)$ is the model prediction using only the feature values x_S in subset S. This formulation determines the marginal contribution of feature i by comparing model predictions with and without the feature across all possible feature combinations.

$$\phi_i = \sum\nolimits_{S \subseteq F \setminus \{i\}} \frac{|S|!\,(|F| - |S| - 1)!}{|F|!} \left[f_{S\cup\{i\}}\left(x_{S\cup\{i\}}\right) - f_S(x_S) \right]$$

Figure 45. Equation. Calculation of SHAP value for the i^{th} feature.

The SHAP algorithm was used to quantify the contribution of each input variable to the XGBoost model's predictions and to provide global explanations of its performance. SHAP values share the same units as the model output, which represents the residual load-carrying capacity (C_R). A positive SHAP value indicates that the feature increases the model output, while a negative SHAP value decreases the output.

Figure 46 shows a SHAP summary plot highlighting the contribution of each input feature to predictions across the entire dataset. Individual points represent SHAP values of all samples for each input feature. The color of the points indicates the actual value of that feature, using red for high values and blue for low values. For example, results show that high values (red points) of observed horizontal and vertical damage deflection (D_x and D_y) have negative SHAP values, leading to lower predicted values of the residual load-carrying capacity, whereas smaller damage deflections have positive SHAP values, indicating less reduction in capacity.

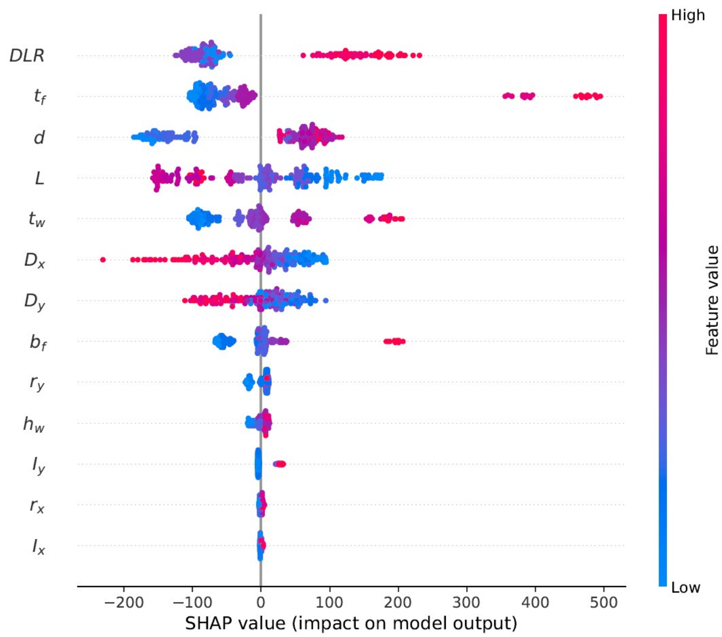

Figure 46. Graph. SHAP summary plot.

Figure 47 presents the global importance of each input variable based on their mean SHAP values. Features are ranked according to their global importance and influence on XGBoost model predictions, using their average absolute SHAP value. The most important features affecting XGBoost prediction of residual capacity were damage location ratio (DLR), flange thickness (t_f), girder depth (d), span length (L), web thickness (t_w), observed horizontal damage deflection (D_x), observed vertical damage deflection (D_y), and flange width (b_f).

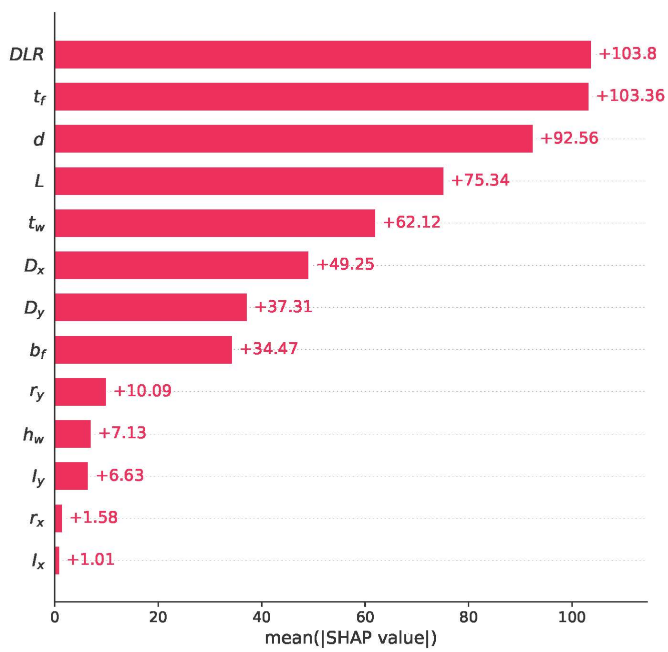

Figure 47. Graph. SHAP importance bar plot.

These results are further supported by the SHAP dependence plots shown in Figure 48, which illustrate how SHAP values of a given feature vary with its actual values. Each point represents an individual prediction instance, colored based on the value of a second feature to reveal interaction effects. For instance, Figure 48-C shows a negative linear relationship between observed horizontal deflection (D_x) and its SHAP values. Similarly, Figure 48-D shows that the SHAP values of observed vertical deflection (D_y) decrease as its actual values increase. This indicates a physically intuitive finding that larger damage deflections due to strikes significantly reduce the residual capacity of steel I-girders.

In addition, Figure 48-E reveals that strikes occurring at girder midspan ($DLR = 0.50$) have more negative SHAP values than those at other locations, suggesting a stronger effect on girder residual capacity reduction. From a structural mechanics perspective, this pattern is expected, as the maximum (controlling) positive bending moment in continuous steel girders typically occurs near midspan, so damage at that location has a greater impact on a girder's load-carrying capacity (Ibrahim 2026). In contrast, strikes located closer to a support benefit from force redistribution and greater restraint from the supports, which can limit the reduction in girder global capacity. The negative SHAP values associated with $DLR = 0.50$ therefore reflect the greater influence of damage at the location of maximum moment.

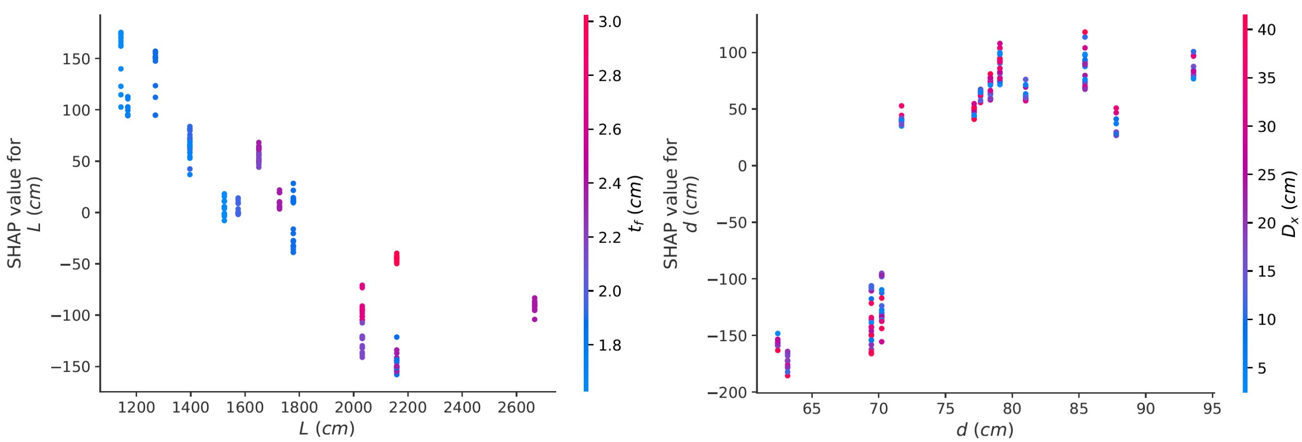

A. Span length

B. Girder depth

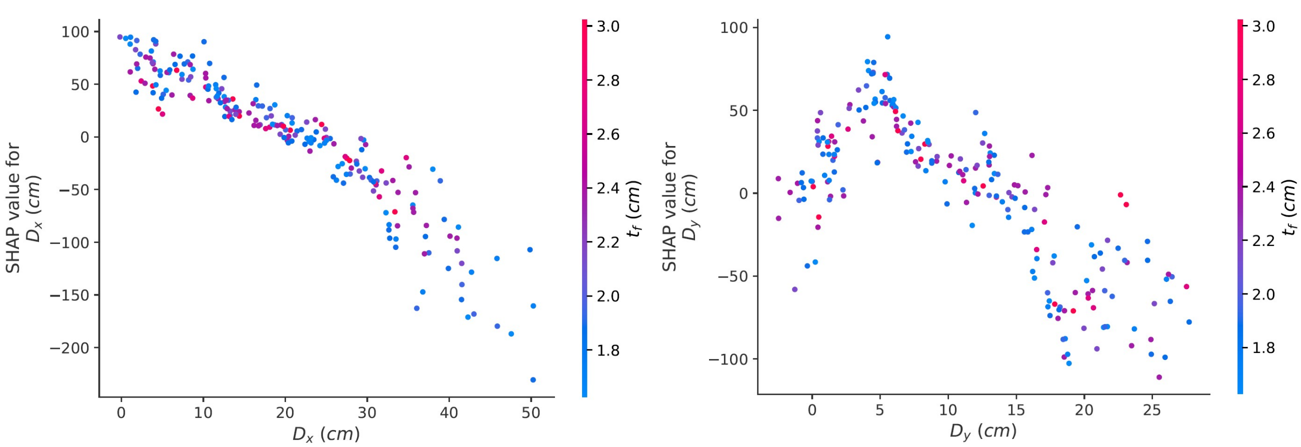

C. Observed horizontal deflection

D. Observed vertical deflection

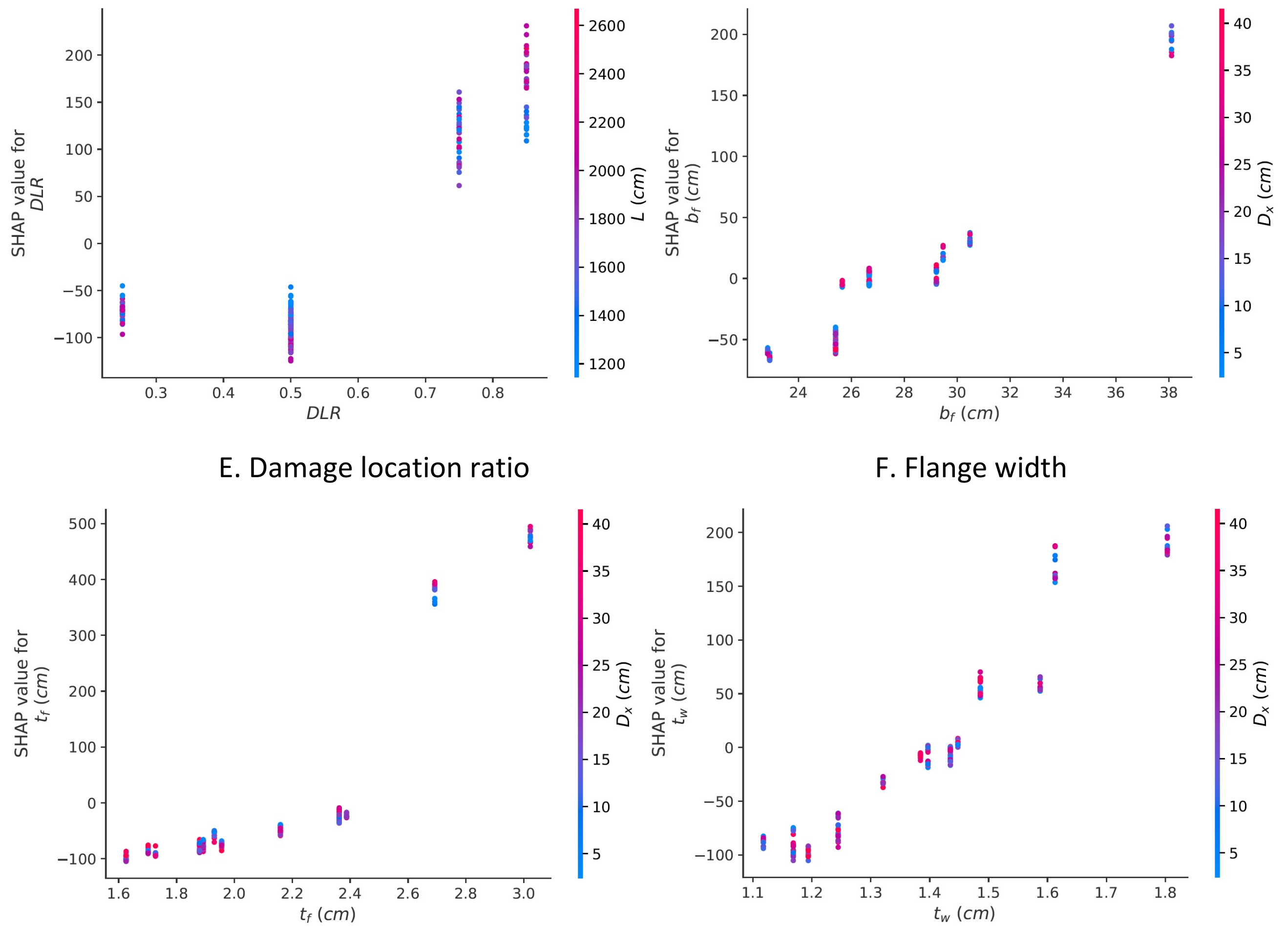

E. Damage location ratio

F. Flange width

G. Flange thickness

H. Web thickness

Figure 48. Graph. SHAP dependence scatter plots.

Additionally, the dependence plots show that SHAP values tend to become positive once the girder depth (d), flange width (b_f), flange thickness (t_f), and web thickness (t_w) exceed approximately 72 cm (28.3 in.), 26 cm (10.2 in.), 2.4 cm (0.94 in.), and 1.4 cm (0.55 in.), respectively, whereas SHAP values for span length (L) gradually transition from predominantly positive to predominantly negative over the range of 16–18 m (630–709 in.) of span length, as summarized in Table 9.

These findings are consistent with structural mechanics and design principles, as deeper girders with wider and thicker flanges and webs exhibit higher residual load-carrying capacity even after damage. Conversely, longer spans are associated with larger bending moment demands, so increasing L naturally leads to a reduction in residual capacity. The numerical thresholds identified from the SHAP framework could be used to inform limit checks in existing design codes and evaluation provisions for steel bridge I-girders susceptible to over-height vehicle strikes, by indicating ranges of geometric properties that help mitigate reductions in post-strike residual capacity.

These results capture the expected mechanical behavior by assigning more negative contributions to midspan strikes and smaller or positive contributions to strikes closer to supports. The explainability of the XGBoost model is consistent with engineering intuition and provides interpretable insights into the decision-making process for evaluating damaged steel bridge girders.

Table 9. Threshold Values Derived from SHAP Dependence Plots

Variable	Threshold Value
Span length (L)	$>$ 16 m–18 m
Girder depth (d)	$<$ 72 cm
Observed horizontal deflection (D_x)	$>$ 23 cm
Observed vertical deflection (D_y)	$>$ 14 cm
Damage location ratio (DLR)	$=$ 0.5 (midspan)
Flange width (b_f)	$<$ 26 cm
Flange thickness (t_f)	$<$ 2.4 cm
Web thickness (t_w)	$<$ 1.4 cm

LIME Explainability Framework

To gain insight into how input features contribute to individual predictions, two representative samples from the training and test sets are presented in Table 10 and examined for their local feature contributions. Compared to the SHAP technique, which can explain both global and local model behavior, LIME is a local method that explains individual predictions of any model without capturing the global influence of input features across the entire dataset. LIME interprets the prediction of a given sample by locally constructing a linear surrogate model around the sample prediction to explain the behavior of the original model (Ribeiro et al. 2016). Coefficients of this surrogate model represent how strongly each feature influences the prediction for that specific sample. In this study, LIME is used to interpret predictions of the trained XGBoost model for two samples listed in Table 10. Figure 49 and Figure 50 show the local LIME explanations for samples 1 and 2, respectively, where green bars indicate features that increase the predicted residual capacity and red bars indicate features that decrease it.

Table 10. Variable Values of Damaged Girder Samples

Sample #	**1**	**2**
Dataset	**Training**	**Test**
L (cm)	1524	1575
d (cm)	69.4	63.2
b_f (cm)	25.4	22.9
t_f (cm)	1.63	1.96
t_w (cm)	1.17	1.19
h_w (cm)	66.2	59.3
r_x (cm)	27.8	25.6
r_y (cm)	5.28	4.95
I_x ($\times 10^{-4}$ cm^4)	12.3	10.5
I_y ($\times 10^{-3}$ cm^4)	4.45	3.93
D_x (cm)	41.1	1.88
D_y (cm)	20.5	1.91
DLR	0.75	0.50

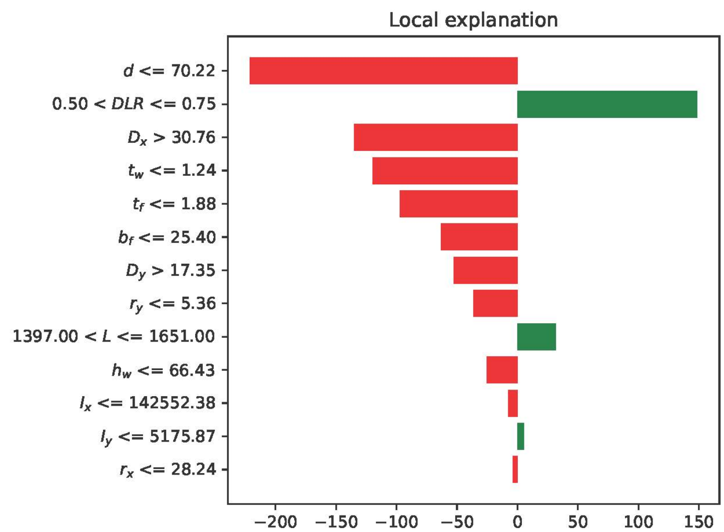

Figure 49. Graph. LIME importance bar plots for individual sample girder #1.

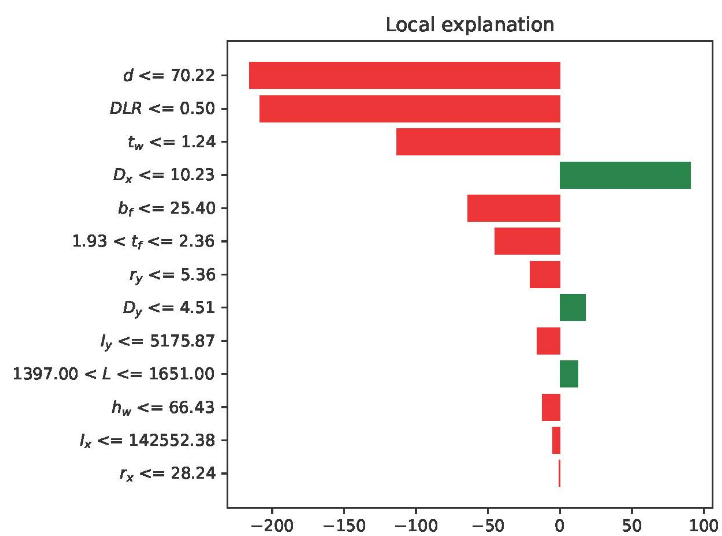

Figure 50. Graph. LIME importance bar plots for individual sample girder #2.

The feature ranges in the LIME plots also indicate the value limits of each feature that lead to an increase or decrease in the predicted capacities. For example, an observed horizontal damage deflection (D_x) value greater than 30.76 cm (12.1 in.) reduces the predicted capacity of sample 1, whereas a D_x value less than or equal to 10.23 cm (4.0 in.) for sample 2 increases the predicted residual capacity. Furthermore, the girder depth (d) being less than or equal to 70.22 cm (27.6 in.) in both samples leads to the largest reduction in the predicted capacity, suggesting that the cutoff for girder depth to avoid a significant capacity reduction is around 70 cm (27.56 in.). This is further supported by the SHAP dependence plot of girder depth (d) in Figure 48-B, where the SHAP values become positive for $d \gtrsim 70$ cm, indicating a positive contribution to predicted capacity beyond that depth.

CHAPTER 6: DEVELOPMENT OF DIAGNOSTIC TOOLS

Two interactive diagnostic tools have been developed to translate the methodologies and findings of this research into practical, user-oriented applications for bridge evaluation. These tools are intended to support state departments of transportation (DOTs) in assessing damaged steel I-girders through accessible and efficient workflows. The first tool has been designed to follow the point cloud-based measurement framework, enabling users to process terrestrial laser scanning (TLS) data and obtain girder deformation profiles. The second tool has been developed to integrate the trained XGBoost model with user-defined inputs to predict the residual load-carrying capacity of damaged girders. Both tools are implemented in Python using the `Streamlit` library and are deployed through an interactive web interface to enhance accessibility and practical use by state DOT personnel.

PROCESSING OF POINT CLOUD MEASUREMENTS

The point cloud measurement tool has six modules for the processing steps listed in Chapter 3: girder segmentation, outlier removal, longitudinal alignment, measurements, adjusting for cover/splice plates, and noise removal. For each module, the user inputs manual parameters, then presses the "Run" button to perform automated processing. The tool shows visualizations for the output—such as measurement plots, cross-sections, or interactive 3D views of point clouds—so the user can evaluate whether the result is satisfactory before proceeding to the next step. Intermediate results can be saved after each step so the user can pause and resume the procedure. Screenshots of select input screens are included in this report. All parameters are defined in Chapter 3 and/or in Schissler et al. (2026b). Throughout the tool, care should be taken to use the same units for the diagnostic tool manual inputs as are in the point cloud file (e.g., inches, meters, etc.). Example values for bridge SN 084-0014 Girder 18 (as presented in Schissler et al. 2026b) are included in the input screenshots; units for that example are in inches. A full tutorial for the measurement diagnostic tool, which will include output visualizations and detailed parameter descriptions, is forthcoming.

Currently, separate software (such as the open-source package CloudCompare, or similar) is required for the initial qualitative girder segmentation. Then, a user uploads the point cloud to the diagnostic tool for the remaining steps, starting with outlier removal (using the simple radius outlier removal algorithm), as shown in Figure 51. A 3D point cloud viewer opens to show the output.

The longitudinal alignment step includes two sets of manual parameters, as shown in Figure 52. The first set of parameters are used for the endpoint search, including the longitudinal tolerance, width of slice at girder ends, threshold number of points skipped in RANSAC fit, and girder depth. These parameters typically require adjustment for each damage case. The second set of parameters are specific to the RANSAC fit used for locating the endpoints of the span. Please see Schissler et al. (2026b) for a full description of the parameters.

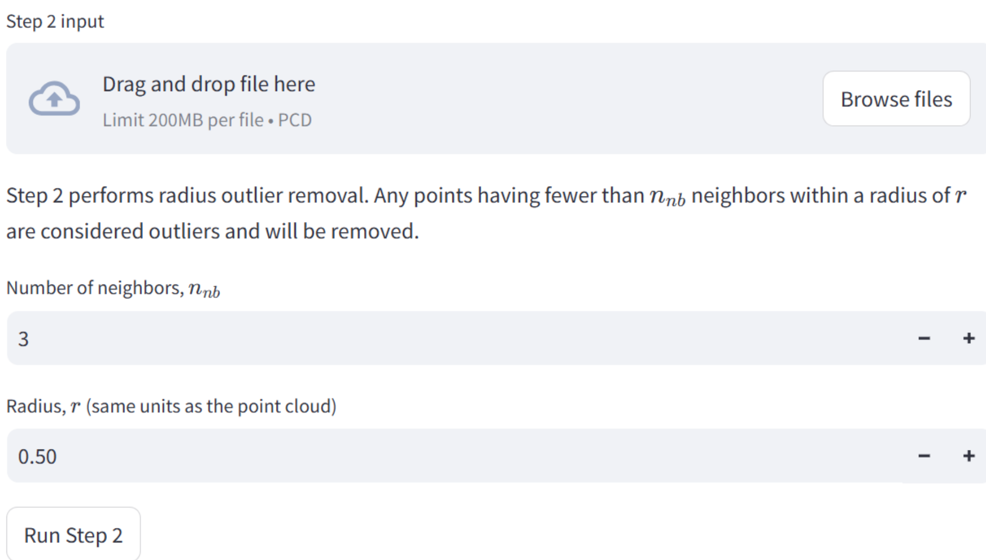

Figure 51. Illustration. User inputs for point cloud processing Step 2: outlier removal.

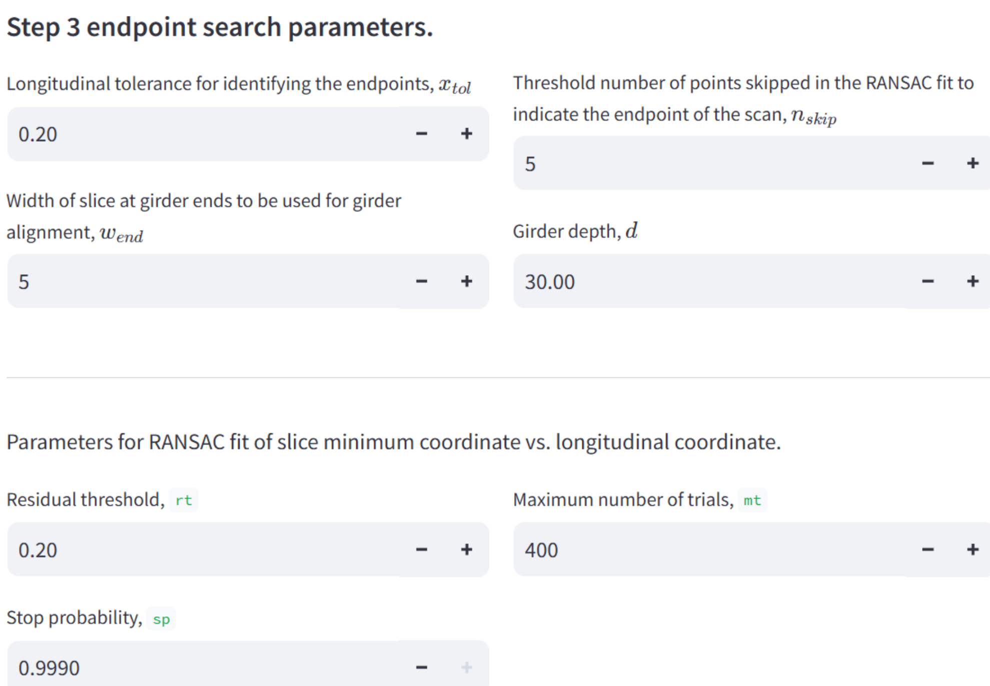

Figure 52. Illustration. User inputs for point cloud processing Step 3: longitudinal alignment.

For the coordinate measurement step, the user enters the desired longitudinal measurement interval and voxel side length, along with the girder flange width, as shown in Figure 53-A. The flange width from the construction drawings is typically sufficient. The same RANSAC parameters as in the longitudinal alignment step are also needed, but the values do not need to be the same as for the longitudinal alignment step. The user can opt to generate cross-sectional slices (along the entire span or a portion of the span) showing the bottom flange region, bottom flange RANSAC line, and measured points. The user enters the parameters in Figure 53-B for consistent slice visualizations. Generating cross-sectional slice plots increases computational time but can provide helpful information for evaluating or troubleshooting the measurement step.

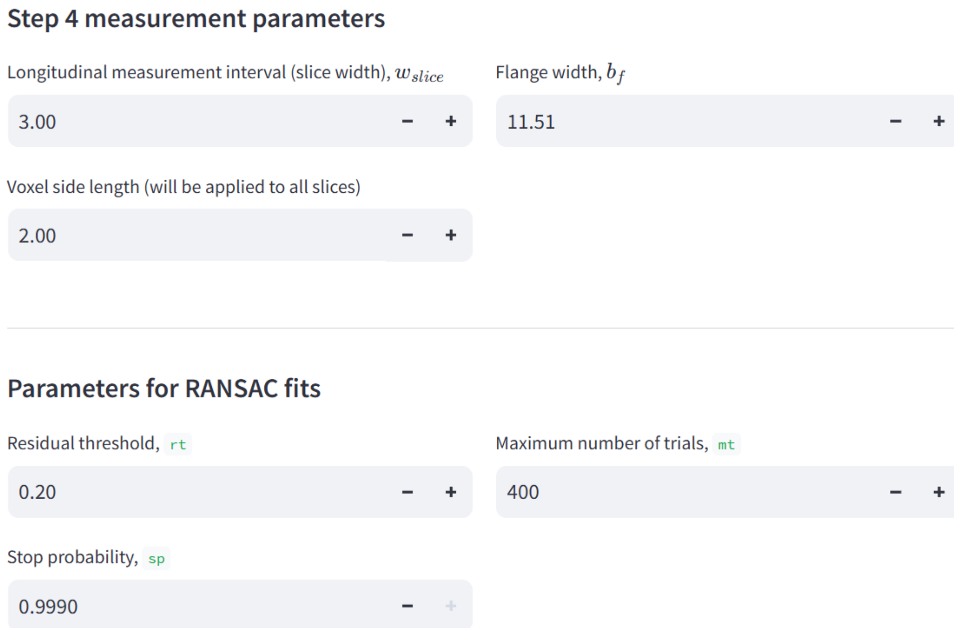

A. Inputs for the automatic displacement measurement process.

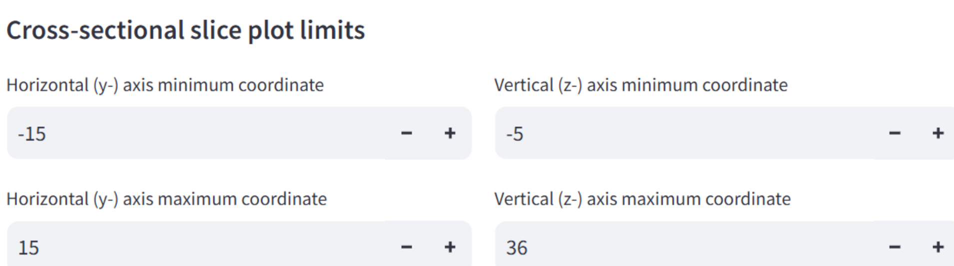

B. Inputs to adjust the cross-sectional slice plots, which are an optional output useful for troubleshooting.

Figure 53. Illustration. User inputs for point cloud processing Step 4: coordinate measurements.

In the step adjusting for cover/splice plates, the user can select how many plates are present within the span. Then, the user can enter different coordinate values of plates for the left corner, centerline, and right corner (for flexibility). In Figure 54, the tab for the left corner is selected. For cross-sectional slices around plate ends, the bottom-flange region (automatically detected in the coordinate measurement step) may include points on both the plate and bottom surface of the flange of the W-section, resulting in a RANSAC line that represents neither surface. The result can be inconsistent for the left corner, centerline, and right corner measurements, so slightly different values for the "start" and "end" longitudinal (x-) coordinates may be needed. Results for the left corner, centerline, and right corner are shown separately so the user can evaluate accordingly.

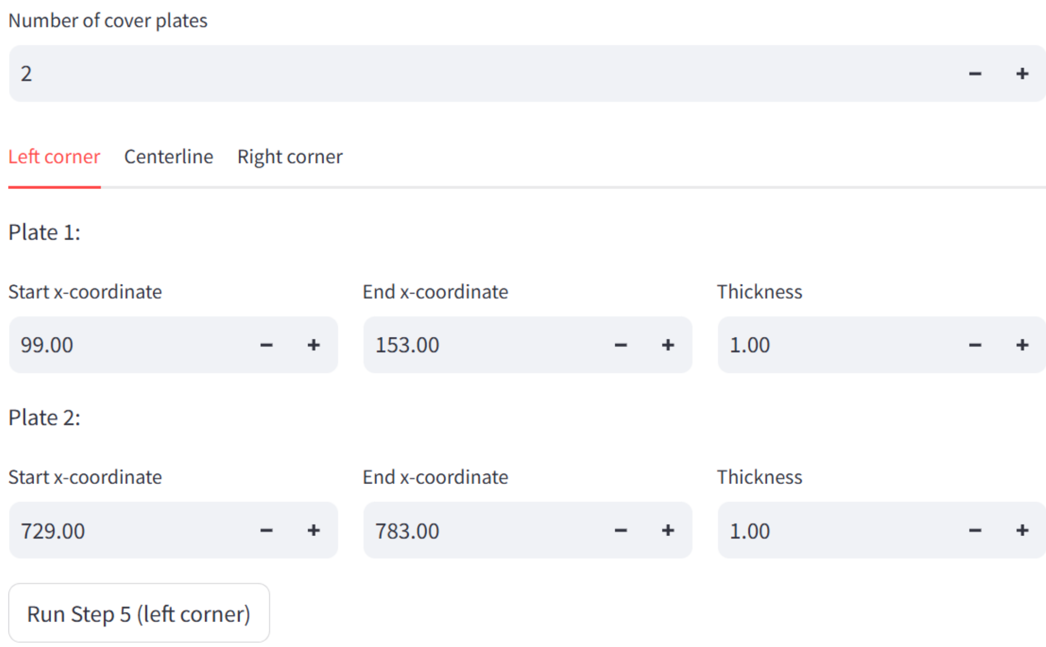

Figure 54. Illustration. User inputs for point cloud processing Step 5: adjusting for cover/splice plates.

In the noise-removal step, the user also considers the left corner, centerline, and right corner measurements separately, as shown in the tabs at the top of Figure 55. For both horizontal and vertical displacement measurements, the user enters the minimum (physical) period to be preserved (in the same units as the measurements), the order of the Butterworth filter, and selects whether to include a spline at the location of maximum displacement. The result of each reference point (left corner, centerline, and right corner) can be evaluated and refined separately. Finally, the results from all three reference points are plotted together.

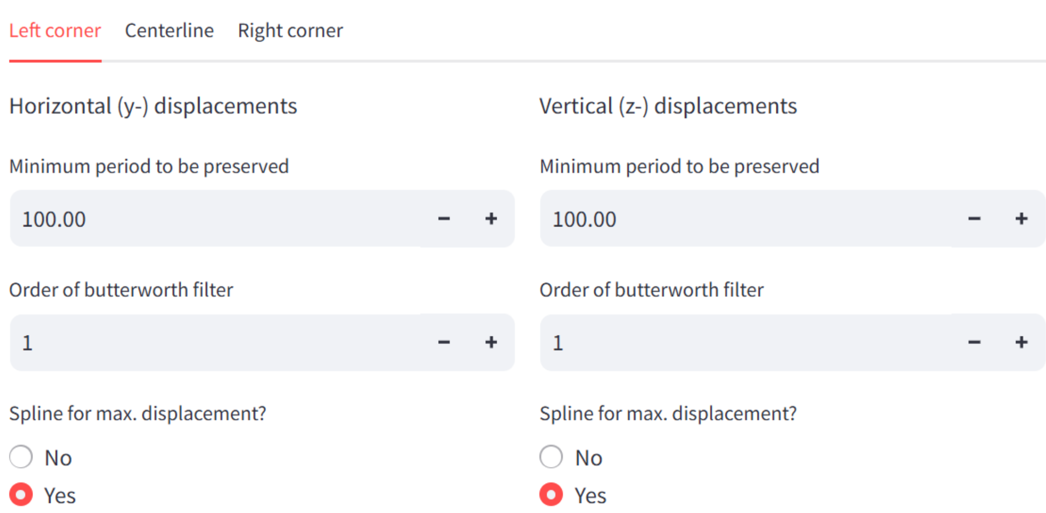

Figure 55. Illustration. User inputs for point cloud processing Step 6: noise removal.

AI-BASED CAPACITY PREDICTION

Geometric properties of the steel I-girder cross-section are defined by the user, either through manual entry or by selecting from a suite of standard AISC steel rolled sections. When a standard section is selected, the corresponding properties are automatically populated, as shown in Figure 56. In all cases, the span length must be provided to complete the required geometric inputs for girder capacity analysis.

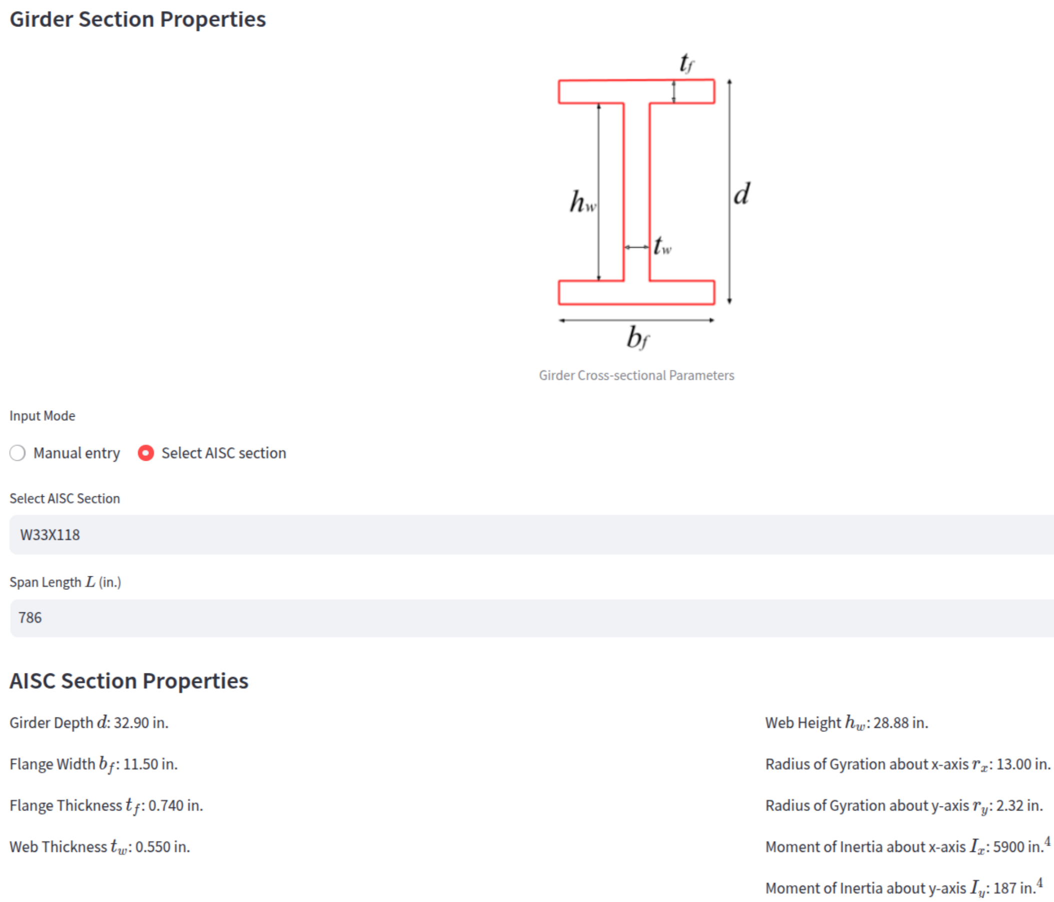

Figure 56. Illustration. Input of girder sectional properties.

Additionally, damage characteristics of the girder are specified by the user, including the maximum observed horizontal and vertical bottom flange deflections and the damage location expressed as a fraction of the span length, as shown in Figure 57. These inputs represent the key parameters required by the trained machine learning model. Once the inputs are provided, the analysis is initiated by selecting the "Run Prediction" button.

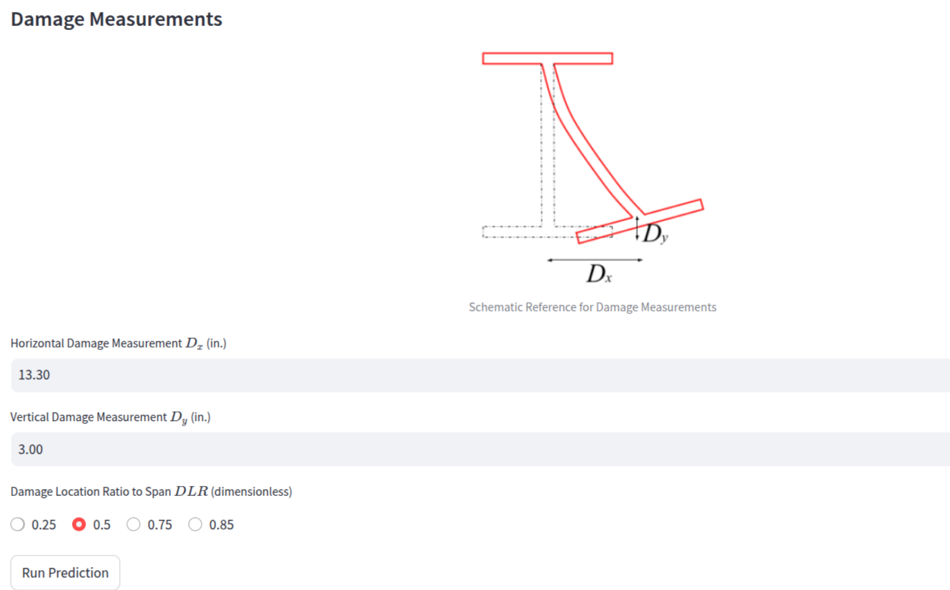

Figure 57. Illustration. Input of damage characteristics and location ratio.

Output from the machine learning model includes the predicted residual load-carrying capacity—expressed as an equivalent uniformly distributed load—along with an additional self-load percentage to account for the presence of damage, as shown in Figure 58. These outputs provide a quantitative basis for evaluating the structural performance of a damaged girder and can be used to inform load rating procedures, as described in the following section. The additional self-load percentage is intended as part of a surrogate method to indirectly account for damage effects using an undamaged girder model.

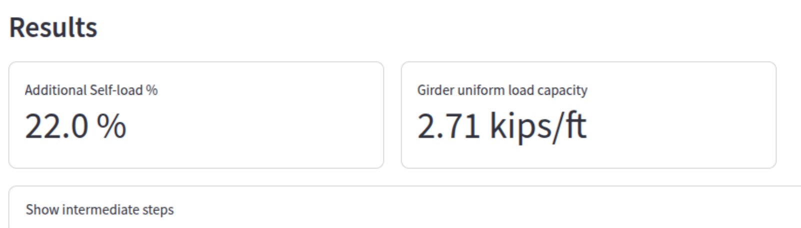

Figure 58. Illustration. Machine learning model outputs.

Finally, the contribution of input parameters to the predicted capacity is evaluated using the LIME framework, as shown in Figure 59. A case-specific bar plot ranks the most influential parameters, where red bars indicate parameters contributing to a reduction in the predicted capacity, and green bars indicate parameters that do not directly contribute to capacity reduction. Parameters with negative contributions can give insight into potential mitigation strategies in accordance with established guidelines for the evaluation and repair of damaged steel girders (e.g., Shanafelt and Horn 1984).

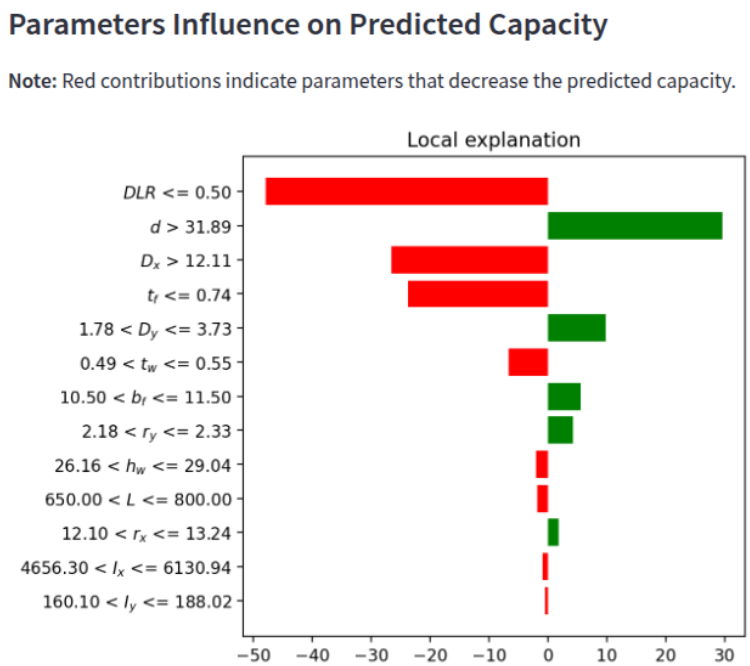

Figure 59. Illustration. LIME-based feature contributions.

IMPLEMENTATION OF CAPACITY PREDICTION IN IDOT WORKFLOW

As specified in AASHTO *LRFD Bridge Design Specifications* (2020), extreme limit states, such as vehicle collisions, are unique events that must be considered to ensure the structural survival of a bridge. In this context, the residual capacity ratio C_R/C—where C_R and C are the corresponding capacities of the damaged and undamaged girders, respectively—may be utilized as a damage-induced reduction factor to scale nominal resistances and obtain equivalent residual resistances for post-strike evaluation.

The predicted additional self-load percentage obtained from the machine learning model can be incorporated into the bridge evaluation process within the AASHTOWare Bridge Rating software to account for the effects of damage on I-girder capacity (when the girder is still modeled as undamaged). This integration establishes a direct connection between the data-driven predictions and standard load rating procedures used by state departments of transportation.

Specifically, the damaged girder is modified within the software through the “Member Alternative Description” tab by assigning the computed additional self-load percentage to the “additional self-load” field, as shown in Figure 60. This modification introduces an equivalent increase in dead load to reflect the reduction in structural capacity due to damage, allowing the analysis to consider the degraded condition of the girder without the need for explicitly modifying its geometry to account for the damage. If an additional self-load percentage already exists to account for secondary members and connection weight, the value provided by the diagnostic tool should be added to the existing percentage rather than replacing it.

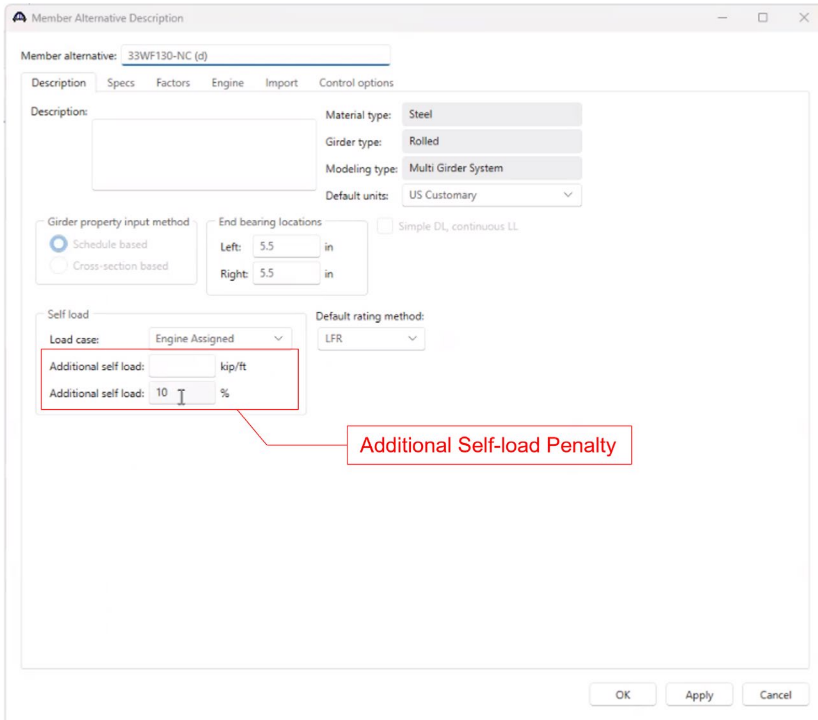

Figure 60. Illustration. Implementation of additional self-load percentage in AASHTOWare Bridge Rating.

Once implemented, the girder with modified loading can be evaluated using the full capabilities of the software, including line-girder, 2D, or 3D analysis methods, as well as permit and routing evaluations and other integrated applications. Rating factors for the damaged bridge can then be computed under various loading scenarios, including standard design truck configurations, user-defined vehicles, and load and resistance factors, in accordance with AASHTO LRFD or LFD specifications. Since damage from over-height vehicle strikes is often limited to a portion of the girder length, the reduction in rating factors should be evaluated primarily within the damaged region, where the damage effects are most pronounced, rather than along the entire length of the girder. This approach enables a streamlined and consistent workflow for incorporating machine learning–based predictions into established bridge rating practices.

The proposed implementation is intended to provide a practical analysis framework for incorporating girder damage effects into routine bridge evaluation workflows. Because the residual capacity of a damaged girder is influenced by numerous factors—including girder geometry, span length, damage magnitude and location—that collectively determine its value, the development of new simple structural analysis guidelines was not pursued. Instead, machine learning serves as a surrogate model to detailed finite element analyses by predicting an equivalent load amplification that approximates the effect of the damaged condition. This approach enables rapid evaluation of bridge strikes while preserving the underlying structural mechanics and supporting consistent application within existing bridge rating procedures. The current IDOT damage evaluation procedure remains as a reasonable simplified approach, which appears to be conservative based on pilot comparisons to the new capacity prediction approach.

CHAPTER 7: SUMMARY AND CONCLUSIONS

Steel I-sections damaged in impact events must be inspected and assessed quickly and effectively to maintain safe conditions and minimize negative effects on infrastructure users. This research project aimed to develop an integrated, data-driven framework for rapid inspection, assessment, and evaluation of steel bridge girders damaged by over-height vehicle strikes.

To this end, the researchers developed a novel procedure for obtaining a bottom-flange displacement profile from a laser-scan point cloud. The semiautomated modular procedure consists of six key steps: girder segmentation, outlier removal, longitudinal alignment, coordinate measurements, adjusting for cover/splice plates, and noise removal. Because the proposed procedure measures three key cross-sectional locations (the left corner, centerline, and right corner) on the bottom surface of the I-girder bottom flange, the displacement and tilt can be characterized accurately, as illustrated in the four case studies presented in this report. Laser scanning for damage characterization offers several advantages over traditional approaches, such as reducing road closures, avoiding work at height, and capturing more comprehensive data.

Furthermore, this study developed a data-driven and interpretable machine learning framework to estimate the residual load-carrying capacity of steel bridge I-girders damaged by over-height vehicle impacts. The methodology integrates finite element–based data generation, informed by field girder information and displacement measurements, along with multiple machine learning algorithms to provide rapid capacity predictions, while incorporating explainable artificial intelligence (XAI) techniques to enhance transparency and engineering interpretability. The developed approach enables efficient and reliable assessment of damaged girders and supports informed decision-making within bridge evaluation workflows.

The main contributions of the study are summarized as follows:

- Review of current practices for damaged girder inspection, assessment, and repair.
- Creation of semiautomated modular procedure for processing a laser-scan point cloud to obtain displacement measurements over the span of a damaged girder.
- Implementation of the developed point cloud measurement procedure on case studies to evaluate its efficacy and consider implications.
- Development of machine learning models that provide accurate and computationally efficient surrogates to detailed finite element analyses for assessing residual capacity of damaged steel girders.
- Evaluation and comparison of multiple algorithms with demonstrated strong predictive performance, particularly the XGBoost model that achieved high R^2 values and low MAPE values on both training and test datasets.

- Validation of model robustness and generalizability through *K*-fold cross-validation, confirming consistent performance across different data partitions.
- Integration of explainable artificial intelligence techniques (SHAP and LIME) to interpret model predictions, identify key influencing parameters, and establish confidence in model outputs.
- Identification of physically meaningful relationships and threshold values from SHAP analyses and the influence of geometric properties, providing insights that align with structural mechanics and can inform evaluation practices.

The optimized machine learning models are trained based on a representative dataset constructed from finite element simulations informed by field observations, which defines the range of input features and damage scenarios considered in the dataset. The developed methodology can be used to extend the collected dataset to include additional girder types, span arrangements, material properties, and loading conditions, leading to a more comprehensive data-driven framework for assessing the residual load-carrying capacity of damaged steel bridge girders.

This project is an important step toward transitioning from current methods of practice—which involve hand measurements and approximate methods for damage evaluation—to more streamlined and automated approaches that leverage modern technology. More efficient and accurate measurement methods, combined with powerful mechanics-based and data-driven simulation tools, provide a pathway for bridge engineers to rapidly assess bridge damage, make critical operational decisions, and plan for appropriate repair and/or replacement. This new framework enables greater safety, sustainability, and service to the motoring public.

REFERENCES

American Association of State Highway and Transportation Officials. (2020). *LRFD bridge design specifications* (9th ed.). AASHTO.

American Institute of Steel Construction. (2017). *Steel construction manual* (15th ed.). AISC.

Agrawal, A. K., Xu, X., & Chen, Z. (2011). *Bridge-vehicle impact assessment* (Report No. C-07-10). University Transportation Research Center. https://rosap.ntl.bts.gov/view/dot/25150/dot_25150_DS1.pdf

Almustafa, M. K., & Nehdi, M. L. (2022). Machine learning prediction of structural response of steel fiber-reinforced concrete beams subjected to far-field blast loading. *Cement and Concrete Composites*, *126*, 104378. https://doi.org/10.1016/j.cemconcomp.2021.104378

Bedi, A. K. (2000). Study of a typical bridge girder damaged by vehicle impacts. In *Forensic Engineering (2000)* (pp. 263–272). https://doi.org/10.1061/40482(280)29

Cha, G., Park, S., & Oh, T. (2019). A terrestrial LiDAR-based detection of shape deformation for maintenance of bridge structures. *Journal of Construction Engineering and Management*, *145*(12), 04019075. https://doi.org/10.1061/(ASCE)CO.1943-7862.0001701

Chen, H., & Shen, J. (2018). Denoising of point cloud data for computer-aided design, engineering, and manufacturing. *Engineering with Computers*, *34*(3), 523–541. https://doi.org/10.1007/s00366-017-0556-4

Chen, T., & Guestrin, C. (2016, August). XGBoost: A scalable tree boosting system. In *Proceedings of the 22nd ACM SIGKDD International Conference on Knowledge Discovery and Data Mining* (pp. 785-794). https://doi.org/10.1145/2939672.2939785

Dassault Systèmes. (2021). *Abaqus/CAE (Version 2021)* [Computer software].

Deka, P. C. (2019). *A primer on machine learning applications in civil engineering*. CRC Press.

Di Mucci, V. M., Cardellicchio, A., Ruggieri, S., Nettis, A., Renò, V., & Uva, G. (2024). Artificial intelligence in structural health management of existing bridges. *Automation in Construction*, *167*, 105719. https://doi.org/10.1016/j.autcon.2024.105719

Dissanayake, M., Nguyen, H., Poologanathan, K., Perampalam, G., Upasiri, I., Rajanayagam, H., & Suntharalingam, T. (2022). Prediction of shear capacity of steel channel sections using machine learning algorithms. *Thin-Walled Structures*, *175*, 109152. https://doi.org/10.1016/j.tws.2022.109152

Dunne, R., & Thorkildsen, E. (2020). *Case study: Response to bridge impacts—An overview of state practices* (No. FHWA-HIF-20-087). https://rosap.ntl.bts.gov/view/dot/54456

Erdélyi, J., Kopáčik, A., & Kyrinovič, P. (2020). Spatial data analysis for deformation monitoring of bridge structures. *Applied Sciences*, *10*(23), 8731. https://doi.org/10.3390/app10238731

Finley, A. M. (2006). *Effects of corrosion and vehicular impact damage on ultimate capacity of steel bridge beams*. Oklahoma State University.

Fischler, M. A., & Bolles, R. C. (1981). Random sample consensus: a paradigm for model fitting with applications to image analysis and automated cartography. *Communications of the ACM*, *24*(6), 381-395. https://doi.org/10.1145/358669.358692

Fu, C. C., Burhouse, J. R., & Chang, G. L. (2004). Overheight vehicle collisions with highway bridges. *Transportation Research Record*, *1865*(1), 80–88. https://doi.org/10.3141/1865-12

Ghosn, M., Moses, F., & Wang, J. (2003). *Design of highway bridges for extreme events* (Vol. 30). Transportation Research Board.

Han, X. F., Jin, J. S., Wang, M. J., Jiang, W., Gao, L., & Xiao, L. (2017). A review of algorithms for filtering the 3D point cloud. *Signal Processing: Image Communication*, *57*, 103–112. https://doi.org/10.1016/j.image.2017.05.009

Hassija, V., Chamola, V., Mahapatra, A., Singal, A., Goel, D., Huang, K., ... & Hussain, A. (2024). Interpreting black-box models: A review on explainable artificial intelligence. *Cognitive Computation*, *16*(1), 45–74. https://doi.org/10.1007/s12559-023-10179-8

Hosseinpour, M., Sharifi, Y., & Sharifi, H. (2020, October). Neural network application for distortional buckling capacity assessment of castellated steel beams. In *Structures* (Vol. 27, pp. 1174–1183). Elsevier. https://doi.org/10.1016/j.istruc.2020.07.027

Ibrahim, A. E. (2026). *Automated inspection and assessment of damaged steel girders using computer vision and machine learning* (Ph.D. dissertation, University of Illinois Urbana-Champaign).

Ibrahim, A. E., Fahnestock, L. A., LaFave, J. M., & Elbanna, A. E. (2026). Explainable machine learning for predicting the load-carrying capacity of damaged steel girders after over-height vehicle strikes. *Engineering Structures*, *357*, 122517. https://doi.org/10.1016/j.engstruct.2026.122517

Illinois Department of Transportation. (2024). *Structural Services Manual*. Springfield, IL.

Lee, J., Lee, K. C., Lee, S., Lee, Y. J., & Sim, S. H. (2019). Long-term displacement measurement of bridges using a LiDAR system. *Structural Control and Health Monitoring*, *26*(10), e2428. https://doi.org/10.1002/stc.2428

Lewis, C. D. (1982). Industrial and business forecasting methods: A practical guide to exponential smoothing and curve fitting.

Liu, J., Alexander, J., Gu, Q., & Li, Y. (2023). Gaussian process regression-based load-carrying capacity models of corroded prestressed concrete bridge girders for fast-screening and reliability-based evaluation. *Engineering Structures*, *285*, 116040. https://doi.org/10.1016/j.engstruct.2023.116040

Liu, Y., Ji, W., Li, J., Liu, S., & Yang, W. (2025). Shear performance prediction for corrugated steel web girders based on machine-learning algorithms. *Thin-Walled Structures*, *206*, 112668. https://doi.org/10.1016/j.tws.2024.112668

Lundberg, S. M., Erion, G. G., & Lee, S. I. (2018). Consistent individualized feature attribution for tree ensembles. *arXiv preprint arXiv:1802.03888*. https://doi.org/10.48550/arXiv.1802.03888

Lundberg, S. M., & Lee, S. I. (2017). A unified approach to interpreting model predictions. *Advances in Neural Information Processing Systems*, *30*.

McKay, M. D., Beckman, R. J., & Conover, W. J. (2000). A comparison of three methods for selecting values of input variables in the analysis of output from a computer code. *Technometrics*, *42*(1), 55–61. https://doi.org/10.1080/00401706.2000.10485979

McKinney, W. (2010). Data structures for statistical computing in Python. *scipy*, *445*(1), 51–56.

Molnar, C. (2025). Interpretable Machine Learning: A Guide for Making Black Box Models Explainable (3rd ed.). christophm.github.io/interpretable-ml-book/

Oppong, K., Vakili, A., Saini, D., & Shafei, B. (2024). Characterization of damage to steel bridge girders subjected to over-height vehicle collision. *Journal of Constructional Steel Research*, *221*, 108926. https://doi.org/10.1016/j.jcsr.2024.108926

Pedregosa, F., Varoquaux, G., Gramfort, A., Michel, V., Thirion, B., Grisel, O., ... & Duchesnay, É. (2011). Scikit-learn: Machine learning in Python. *the Journal of machine Learning research*, *12*, 2825-2830.

Psomas, L., Trainor, R., & Alzraiee, H. (2022). Case study: Assessing the structural condition of steel bridges using terrestrial laser scanner (TLS). In *Construction Research Congress 2022* (pp. 433–442).

Rashidi, M., Mohammadi, M., Sadeghlou Kivi, S., Abdolvand, M. M., Truong-Hong, L., & Samali, B. (2020). A decade of modern bridge monitoring using terrestrial laser scanning: Review and future directions. *Remote Sensing*, *12*(22), 3796. https://doi.org/10.3390/rs12223796

Reich, Y. (1997). Machine learning techniques for civil engineering problems. *Computer-Aided Civil and Infrastructure Engineering*, *12*(4), 295–310. https://doi.org/10.1111/0885-9507.00065

Ribeiro, M. T., Singh, S., & Guestrin, C. (2016, August). “Why Should I Trust You?”: Explaining the Predictions of Any Classifier. In *Proceedings of the 22nd ACM SIGKDD International Conference on Knowledge Discovery and Data Mining* (pp. 1135–1144). https://doi.org/10.1145/2939672.2939778

Riveiro, B., González-Jorge, H., Varela, M., & Jáuregui, D. V. (2013). Validation of terrestrial laser scanning and photogrammetry techniques for the measurement of vertical underclearance and beam geometry in structural inspection of bridges. *Measurement*, *46*(1), 784–794. https://doi.org/10.1016/j.measurement.2012.09.018

Rosenblatt, F. (1962). *Principles of neurodynamics: Perceptrons and the theory of brain mechanisms* (Vol. 55). Washington, DC: Spartan books.

Rumelhart, D. E., Hinton, G. E., & Williams, R. J. (1985). *Learning internal representations by error propagation* (No. ICS8506). https://doi.org/10.21236/ADA164453

Rusu, R. B., Marton, Z. C., Blodow, N., Dolha, M., & Beetz, M. (2008). Towards 3D point cloud based object maps for household environments. *Robotics and Autonomous Systems*, *56*(11), 927–941. https://doi.org/10.1016/j.robot.2008.08.005

Schissler, L. R. (2024). *Laser scan point cloud processing for displacement measurements of damaged steel I-girders* (M.S. thesis, University of Illinois at Urbana-Champaign). https://hdl.handle.net/2142/124440

Schissler, L. R., Ahershinge, S., Ibrahim, A. E., Fahnestock, L. A., LaFave, J. M., & Elbanna, A. E. (2024). *Report on agency survey and national bridge inventory analysis for damaged steel girders* (Report No. FHWA-ICT-24-021). Illinois Center for Transportation. https://doi.org/10.36501/0197-9191/24-024

Schissler, L. R., Ahershinge, S., Ibrahim, A. E., Fahnestock, L. A., LaFave, J. M., & Elbanna, A. E. (2026a). Survey and review of bridge strikes and assessment methods for low-clearance steel-girder bridges. *Journal of Structural Design and Construction Practice*, *31*(1), 04025107. https://doi.org/10.1061/JSDCCC.SCENG-1807

Schissler, L. R., LaFave, J. M., Elbanna, A. E., & Fahnestock, L. A. (2026b). Point cloud processing for damage characterization of steel I-sections. *Journal of Structural Engineering*, *152*(6), 04026055. https://doi.org/10.1061/JSENDH.STENG-15640

Shapley, L. S. (1953). A value for n-person games. *Princeton University Press.* https://doi.org/10.1515/9781400881970-018

Shenton, H. W., Dawson, M., & Chavez, A. (2006). Evaluation and rating of damaged steel I-girders. In *3rd Int. Conf. on Bridge Maintenance, Safety and Management—Bridge Maintenance, Safety, Management, Life-Cycle Performance and Cost*.

Seo, H., Zhao, Y., & Chen, C. (2021). Displacement estimation error in laser scanning monitoring of retaining structures considering roughness. *Sensors*, *21*(21), 7370. https://doi.org/10.3390/s21217370

Shanafelt, G. O., & Horn, W. B. (1984). *Guidelines for evaluation and repair of damaged steel bridge members* (No. HS-037 759). National Cooperative Highway Research Program. http://onlinepubs.trb.org/Onlinepubs/nchrp/nchrp_rpt_271.pdf

Stark, T. D., Benekohal, R., Fahnestock, L. A., LaFave, J. M., He, J., & Wittenkeller, C. (2016). I-5 Skagit river bridge collapse review. *Journal of Performance of Constructed Facilities*, *30*(6), 04016061. https://doi.org/10.1061/(ASCE)CF.1943-5509.0000913

Stull, C. J., & Earls, C. J. (2009). A rapid assessment methodology for bridges damaged by truck strikes. *Steel Compos. Struct*, *9*(3), 223–237. https://doi.org/10.12989/scs.2009.9.3.223

Sun, H., Burton, H. V., & Huang, H. (2021). Machine learning applications for building structural design and performance assessment: State-of-the-art review. *Journal of Building Engineering*, *33*, 101816. https://doi.org/10.1016/j.jobe.2020.101816

Truong-Hong, L., & Laefer, D. F. (2019). Laser scanning for bridge inspection. In *Laser scanning* (pp. 189–214). CRC Press.

Tysiac, P., Miskiewicz, M., & Bruski, D. (2022). Bridge non-destructive measurements using a laser scanning during acceptance testing: Case study. *Materials*, *15*(23), 8533. https://doi.org/10.3390/ma15238533

Van Rossum, G., & Drake, F. L. (1995). *Python reference manual* (Vol. 111). Amsterdam: Centrum voor Wiskunde en Informatica.

Wang, C., Song, L. H., Yuan, Z., & Fan, J. S. (2023). State-of-the-art AI-based computational analysis in civil engineering. *Journal of Industrial Information Integration*, *33*, 100470. https://doi.org/10.1016/j.jii.2023.100470

Wang, Q., Sohn, H., & Cheng, J. C. (2016). Development of a mixed pixel filter for improved dimension estimation using AMCW laser scanner. *ISPRS Journal of Photogrammetry and Remote Sensing*, *119*, 246–258. https://doi.org/10.1016/j.isprsjprs.2016.06.004

Wang, Y., & Feng, H. Y. (2014). Modeling outlier formation in scanning reflective surfaces using a laser stripe scanner. *Measurement*, *57*, 108–121. https://doi.org/10.1016/j.measurement.2014.08.010

Wang, Y., Thrall, A. P., Baah, P., & Strain, R. (2022). Behavior of steel girder bridges damaged by vehicular collision. *Engineering Structures*, *255*, 113929. https://doi.org/10.1016/j.engstruct.2022.113929

Waskom, M. L. (2021). Seaborn: statistical data visualization. *Journal of Open Source Software*, *6*(60), 3021. https://doi.org/10.21105/joss.03021

Williams, C. K., & Rasmussen, C. E. (2006). *Gaussian processes for machine learning* (Vol. 2, No. 3, p. 4). Cambridge, MA: MIT press.

Xu, H., Wang, M., Liu, C., & Li, F. (2024). Vertical clearance assessment for highway bridges based on multisensor fusion simultaneous localization and mapping. *Journal of Bridge Engineering*, *29*(2), 04023120. https://doi.org/10.1061/JBENF2.BEENG-6331

Xu, L., Lu, X., Guan, H., & Zhang, Y. (2013). Finite-element and simplified models for collision simulation between overheight trucks and bridge superstructures. *Journal of Bridge Engineering*, *18*(11), 1140–1151. https://doi.org/10.1061/(ASCE)BE.1943-5592.0000472

Xu, Y., Tong, X., & Stilla, U. (2021). Voxel-based representation of 3D point clouds: Methods, applications, and its potential use in the construction industry. *Automation in Construction*, *126*, 103675. https://doi.org/10.1016/j.autcon.2021.103675

Zhao, Y., Wang, D., Zhu, Q., Fan, L., & Bao, Y. (2024). Algorithm-driven extraction of point cloud data representing bottom flanges of beams in a complex steel frame structure for deformation measurement. *Buildings*, *14*(9), 2847. https://doi.org/10.3390/buildings14092847

Zhou, L., Sun, G., Li, Y., Li, W., & Su, Z. (2022). Point cloud denoising review: from classical to deep learning-based approaches. *Graphical Models*, *121*, 101140. https://doi.org/10.1016/j.gmod.2022.101140

Zhou, Q. Y., Park, J., & Koltun, V. (2018). Open3D: A modern library for 3D data processing. *arXiv preprint arXiv:1801.09847*. https://doi.org/10.48550/arXiv.1801.09847

Zhou, Y., Zhu, J., Zhao, L., Hu, G., Xin, J., Zhang, H., & Yang, J. (2024). High-precision monitoring method for bridge deformation measurement and error analysis based on terrestrial laser scanning. *Remote Sensing*, *16*(13), 2263. https://doi.org/10.3390/rs16132263

Ziolkowski, P., Szulwic, J., & Miskiewicz, M. (2018). Deformation analysis of a composite bridge during proof loading using point cloud processing. *Sensors*, *18*(12), 4332. https://doi.org/10.3390/s18124332

APPENDIX A: ADDITIONAL PHOTOGRAPHS OF DAMAGED BRIDGES

This appendix includes additional photographs of the four bridges presented as example case studies for the point cloud processing procedure in Chapter 3. These photographs, which illustrate the nature of the damage for each case, provide additional context for the displacement measurement results.

BRIDGE SN 084-0014

Figure 61. Photo. Overall view of damage to IDOT Bridge SN 084-0014. Girder 18, the front fascia girder, was damaged in the strike (the impact occurred from left to right).

Source: Courtesy of IDOT

Figure 62. Photo. Close-up view of damage to the concrete deck above the impact point on the fascia girder of IDOT Bridge SN 084-0014 Girder 18.

Source: Courtesy of IDOT

Figure 63. Photo. Close-up view of the impact point on IDOT Bridge SN 084-0014 Girder 18. Small nicks and scratches are visible.

Source: Courtesy of IDOT

Figure 64. Photo. Bottom view of damage to IDOT Bridge SN 084-0014 Girder 18, looking toward the center pier. The girder is displaced toward the right.

Source: Courtesy of IDOT

BRIDGE SN 084-0077

Figure 65. Photo. Overall bottom view of damage to IDOT Bridge SN 084-0077; Girder 19 is the left fascia girder (the impact occurred from left to right).

Source: Courtesy of IDOT

Figure 66. Photo. Front view of damage to IDOT Bridge SN 084-0077 Girder 19.

Source: Courtesy of IDOT

Figure 67. Photo. Close-up view near the impact point on IDOT Bridge SN 084-0077 Girder 19. Small nicks and scratches are visible. (The stringline reference is pink.)

Source: Courtesy of IDOT

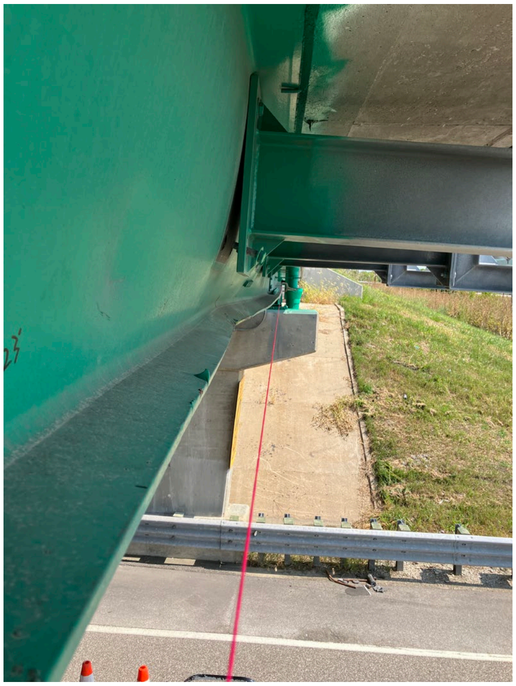

Figure 68. Photo. Longitudinal view of damage to IDOT Bridge SN 084-0077, looking away from the center pier. (The stringline reference is pink.)

Source: Courtesy of IDOT

BRIDGE SN 016-0918

Figure 69. Photo. Damage to IDOT Bridge SN 016-0918 Girder 1, looking toward the center of the span. Red marks drawn on the web indicate the longitudinal location of impact, while bolt holes and green paint indicate directional sign attachment points.

Source: Courtesy of IDOT

Figure 70. Photo. Back view of damage to IDOT Bridge SN 016-0918 Girder 1, looking toward the center of the span. Paint on the back of the girder is peeling.

Source: Courtesy of IDOT

BRIDGE SN 041-0067

Figure 71. Photo. Overall view of damage to IDOT Bridge SN 041-0067. Girder 6 is the first interior girder from front. (Several girders were damaged by the oversized load shown in Figure 1.)

Figure 72. Photo. Overall bottom view of damage to IDOT Bridge SN 041-0067. Girder 6 is the first interior girder from left and was damaged most severely.

Figure 73. Photo. Bottom view of damage to IDOT Bridge SN 041-0067 Girder 6, showing excessive displacement.

Source: Courtesy of IDOT